

SEISMIC BEHAVIOR AND DESIGN OF SEGMENTAL PRECAST POST-TENSIONED
CONCRETE PIERS

By

HAITHAM MOHAMED MAHMOUD MOUSAD DAWOOD

A thesis submitted in partial fulfillment of
the requirements for the degree of

MASTER OF SCIENCE IN CIVIL ENGINEERING

WASHINGTON STATE UNIVERSITY
Department of Civil Engineering

AUGUST 2010

To the Faculty of Washington State University:

The members of the Committee appointed to examine the dissertation/thesis of HAITHAM MOHAMED MAHMOUD MOUSAD DAWOOD find it satisfactory and recommend that it be accepted.

Mohamed A. ElGawady, Ph.D., Chair

William F. Cofer, Ph.D.

David I. McLean, Ph.D.

ACKNOWLEDGEMENT

I'm grateful to Dr. Mohamed ElGawady, my advisor and committee chair, for his guidance, patience and valuable suggestions throughout the entire research work. I would like to thank Dr. William Cofer and Dr. David McLean for their participation and assistance on my committee. I would like also to thank Dr. Joshua Hewes (NAU) for co-authoring the first two publications with me and Dr. ElGawady, also for his constructing comments on the first part of this study. I am also grateful to TransNOW for providing the research funding. I also acknowledge Dr. Mahmoud Imam (Taif U) for all his encouragement and support before and during pursuing my master's degree at WSU.

I dedicate this thesis to my mother (Gihan), my father (Mohamed) and my sweet sisters (Hend and Heba) for surrounding me with their love and kindness throughout my journey of success. I would like to express my deepest appreciation to my wife (Eman) for her love, patient and faithful encouragement and helping me for setting up a good study atmosphere in order to finish my degree. I would also like to thank all my friends and colleagues, Jamal Elmapruk (WSU), Ahmed Awed (U of Idaho), Ahmed El-Hadidy (U of Waterloo) and Waleed Adel (Mansoura U) for their encouragement and moral support during the course of this study.

I would like also to acknowledge the Earthquake Engineering Research Institute (EERI) for providing me with a grant to present this research in the EERI 2010 annual meeting in San Francisco, CA. Also, the civil and environmental engineering department for helping me to attend the meeting.

SEISMIC BEHAVIOR AND DESIGN OF SEGMENTAL PRECAST POST-TENSIONED CONCRETE PIERS

Abstract

By Haitham Mohamed M. Mousad Dawood, M.S.

Washington State University

August, 2010

Chair: Mohamed ElGawady

Segmental precast post tensioned (SPPT) bridge pier is an economical construction system, and a re-centering structural system. Understanding the seismic behavior of the SPPT system is an important step towards its application in high seismic zones.

First, the thesis presents a detailed three dimensional finite element model developed using the ABAQUS platform. A brief description and discussion of cyclic tests on eight large scale SPPT piers was also presented. The finite element model was validated against the experimental results and it showed good agreement. Sensitivity analyses using the finite element model showed that the model is sensitive to the softening behavior of the concrete material constitutive law.

Then, the FE model was used to discuss the design parameters that potentially affect the lateral seismic response of the SPPT bridge piers. Design parameters investigated include the initial post-tensioning stress as a percentage of the tendon yield stress, the applied axial stresses on concrete due to post-tensioning, pier aspect ratios, construction details, steel tube thicknesses, and internal mild steel rebar added as energy dissipaters.

After that, the FE model was validated against two experimental studies conducted at Washington State University. The SPPT piers were tested as single piers in the first study while two SPPT piers were connected from the top with a reinforced concrete beam to form a moment resistant bent in the second study. The FE model showed good agreement with the backbone behavior of the tested specimens. A parametric study was carried out to study the effect of piers dimensions, post-tensioning and external service loads on full scale FE models.

Finally, a large set of FE models of piers with different design parameters was used to develop a set of empirical equations. These equations were incorporated into a design procedure for the SPPT concrete piers.

TABLE OF CONTENTS

	Page
ACKNOWLEDGEMENTS.....	iii
ABSTRACT.....	iv
LIST OF TABLES.....	ix
LIST OF FIGURES.....	x
CHAPTER ONE.....	1
1. INTRODUCTION.....	1
1.1 Innovative Precast Post-tensioned Bridge Piers and Bents Developed at Washington State University.....	1
1.1.1 Structural Advantages.....	1
1.1.2 Construction advantages.....	3
1.1.3 Environmental Advantages.....	3
1.2 Research objectives.....	4
CHAPTER TWO.....	5
2. LITERATURE REVIEW.....	5
2.1 Seismic Behavior of Segmental Precast Post-tensioned Piers	5
2.1.1 Experimental Studies.....	7
2.1.1.1 Experimental Studies Done At WSU.....	7
2.1.2 Simple Models.....	9
2.1.3 Finite Element Models.....	10
2.1.4 Lumped-mass Models.....	11
2.1.5 Energy Dissipation Systems.....	12
2.2 Concrete Confinement	13
2.3 Conclusions.....	14
2.4 References.....	14
CHAPTER THREE.....	16
3. BEHAVIOR OF SEGMENTAL PRECAST POST-TENSIONED BRIDGE PIERS UNDER LATERAL LOADS: EXPERIMENTAL AND MODELING	16
3.1 Abstract.....	16
3.2 Keywords	16
3.3 Introduction.....	17
3.4 Finite Element Modeling of Self-Centering Piers.....	19
3.5 Experimental work.....	23
3.5.1 Test pier design details.....	23
3.5.2 Test setup, instrumentation, and loading protocol.....	26
3.5.3 Description of test results.....	27
3.6 Model Validation.....	31
3.7 Analyses results.....	33
3.8 Sensitivity Analyses.....	40
3.9 Findings and conclusions.....	43
3.10 Acknowledgements.....	44
3.11 References.....	44
CHAPTER FOUR.....	46

4. BEHAVIOR OF SEGMENTAL PRECAST POST-TENSIONED BRIDGE PIERS UNDER LATERAL LOADS: PARAMETRIC STUDY.....	46
4.1 Abstract.....	46
4.2 Keywords.....	47
4.3 Introduction.....	47
4.4 Results and Discussions.....	50
4.4.1 Effects of initial post-tensioning level in the tendon	50
4.4.2 Effects of initial stresses on the concrete	54
4.4.3 Effects of pier aspect ratio	57
4.4.4 Effects of construction details	60
4.4.5 Effects of confinement thickness	62
4.4.6 Effects of adding internal energy dissipaters.....	63
4.5 Findings and Conclusions.....	65
4.6 Acknowledgements.....	67
4.7 References.....	67
CHAPTER FIVE.....	68
5. FINITE ELEMENT MODEL CALIBRATION AGAINST SPPT SYSTEM DEVELOPED IN WASHINGTON STATE UNIVERSITY AND PARAMETRIC STUDY	68
5.1 Introduction.....	68
5.2 Piers Tested by Booker A. (2008)	68
5.3 Bents Tested by Shaalan (2009)	70
5.4 Finite Element Model Implementation.....	71
5.5 Results and Discussions.....	73
5.5.1 Piers.....	73
5.5.2 Bents.....	75
5.6 Parametric Study.....	76
5.6.1 Effects of applied post-tensioning force.....	76
5.6.2 Effects of load combination.....	77
5.6.3 Effects of pier aspect ratio	78
5.6.4 Effects of pier size.....	79
5.6.5 Effects of diameter size.....	80
5.6.6 Effects of confinement.....	81
5.7 Conclusions.....	83
5.8 References.....	84
CHAPTER SIX.....	86
6. PERFORMANCE-BASES SEISMIC DESIGN OF UNBONDED SEGMENTAL PRECAST POST-TENSIONED CONCRETE PIERS.....	86
6.1 Abstract.....	86
6.2 Keywords	87
6.3 Segmental Precast Post-tensioned (SPPT) Piers.....	87
6.4 Residual Drift Angles.....	87
6.5 Summary of the Finite Element Model.....	88
6.6 Study Description.....	90
6.7 Performance levels.....	92
6.7.1 Performance criteria for the serviceability level.....	93

6.7.2 Performance criteria for the collapse-prevention level.....	94
6.8 Equivalent viscous damping.....	94
6.9 Study Procedure.....	95
6.10 Collapse-prevention and Serviceability Performance levels.....	96
6.10.1 Effective stiffnesses (K_{CP-e} and K_{S-e})	96
6.10.2 Yield loads (F_{CP-y} and F_{S-y})	97
6.10.3 Displacements corresponding to yield loads (Δ_{CP-y} and Δ_{S-y}).....	99
6.10.4 Performance displacements (Δ_{CP-P} and Δ_{S-P}).....	99
6.10.5 Performance loads (F_{CP-P} and F_{S-P})	100
6.11 Error in predicting the bilinearized backbone curves	101
6.12 Increases in the post-tensioning force with increasing the applied lateral drift angle.....	103
6.13 Design Procedure	107
6.14 Findings and Conclusions.....	111
6.15 References.....	112
APPENDIX.....	116
A. APPENDIX A (MATERIALS TESTING).....	117
A.1 Concrete.....	117
A.2 Post-tensioning bars.....	119
A.3 Glass Fiber Reinforced Polymer (GFRP).....	121
A.4 Fiber Sheets Used To Retrofit JH12 & JH22 (CHAPTER 3).....	126
A.5 References.....	126

LIST OF TABLES

	Page
Table 2.1: Examples of bridges constructed using segmental piers.....	5
Table 3.1: The matrix of the experimental work.....	24
Table 3.2: Summary of steel coupons tension tests.....	25
Table 3.3: Concrete compressive strength for test units (f_c' , MPa).....	25
Table 3.4: Properties of the FRP.....	30
Table 4.1: Different values assigned for each parameter in the parametric study.....	50
Table 5.1: Description of the piers used in the laboratory testing.....	69
Table 5.2: Description of the bents used in the laboratory testing.....	70
Table 6.1: Different investigated parameters for the SPPT.....	91
Table 6.2: Material Properties of the GFRP tubes.....	91
Table 6.3: Mean, standard deviation an coefficient of variation of the error associated with using the empirical equations.....	103
Table A.1: Summary of compression test results.....	118
Table A.2: Summary of tension tests of GFRP specimens.....	122
Table A.3: Typical dry fiber propertied used in chapter (3).....	126

LIST OF FIGURES

	Page
Figure 1.1: Schematic drawing of the SPPT-CFFT System.....	3
Figure 2.1: Examples of segmental piers	6
Figure 2.2: Piers tested (From ElGawady et al. 2010).....	8
Figure 2.3: Tested frames (From ElGawady and Shaalan 2010).....	9
Figure 2.4: Backbone curve of the test specimens, (From ElGawady et al. 2009).....	10
Figure 3.1: A typical mesh and applied loads and displacements for the SPPT pier.....	20
Figure 3.2: Test setup for specimens.....	26
Figure 3.3: Experimental hysteretic response plots.....	28
Figure 3.4: Experimental hysteretic response plots.....	29
Figure 3.5: Stress strain curves for unconfined and confined concrete.....	31
Figure 3.6: Specimen JH12 (a) during testing, and (b) FE model results.....	34
Figure 3.7: A schematic of a rocking pier indicating stresses and strains at different heights of the pier.....	34
Figure 3.8: Specimen JH11 at failure.....	36
Figure 3.9: Experimental versus predicted backbone curves for slender virgin piers.....	37
Figure 3.10: Experimental versus predicted backbone curves for squat virgin piers.....	38
Figure 3.11: Errors in predicting the strengths.....	38
Figure 3.12: Error in post tensioning stress versus drift angle.....	40
Figure 3.13: Different softening behavior of concrete.....	41
Figure 3.14: The effects of concrete material softening behavior on the response of piers	42
Figure 3.15: Effects of coefficients of friction on the backbone curves of pier JH11	42
Figure 4.1: Detailed dimensions for piers.....	47
Figure 4.2: A typical mesh and applied loads and displacements for the SPPT pier	49
Figure 4.3: The effects of changing the initial post-tensioning stress in the tendons while keeping the same stress on concrete.....	51
Figure 4.4: Piers' drifts Vs. the stresses in the post-tensioning tendons normalized by its yield stress.....	52
Figure 4.5: The effects of changing the initial post-tensioning stress in the tendons for squat piers.....	52
Figure 4.6: Squat piers' drifts Vs. the stresses in the post-tensioning tendons normalized by its yield stress.....	53
Figure 4.7: The effects of increasing the axial stresses due to post-tensioning forces on concrete segments.....	55
Figure 4.8: The increase in the post-tensioning stresses vs. the standard piers lateral drifts	56
Figure 4.9: The effects of increasing the axial stresses on concrete segments for Pier B.	57
Figure 4.10: The increase in the post-tensioning stresses vs. piers type B lateral drifts.....	57

Figure 4.11:	Layout of the piers having different aspect ratios.....	58
Figure 4.12:	The effect of changing the piers' aspect ratio on the backbone curves.....	58
Figure 4.13:	The mechanism of deformation for slender and squat piers.....	59
Figure 4.14:	Configuration of each pier of CON series.....	60
Figure 4.15:	The effects of the different configurations on the backbone curves.....	61
Figure 4.16:	The effects on the backbone curves of the different confinement thicknesses.....	63
Figure 4.17:	The effects of the IED on the backbone curves.....	63
Figure 4.18:	High stress concentrations in the segments due to the insufficient development length of the IED bar.....	64
Figure 4.19:	The effects of different IED rebar diameters on normalized stresses on the rebar.....	65
Figure 5.1:	Schematic drawing showing the setup for the cyclic loading test for the piers.....	69
Figure 5.2:	Schematic drawing for the two piers used for the calibration of the FE model	69
Figure 5.3:	Schematic drawing showing the setup for the cyclic loading test for the bents.....	70
Figure 5.4:	Schematic drawing for the tested frames.....	71
Figure 5.5:	Typical mesh used for the FE model.....	72
Figure 5.6:	Stress strain curves for the concrete	73
Figure 5.7:	Experimental versus predicted backbone curves for the singly segmented pier.....	74
Figure 5.8:	Experimental versus predicted backbone curves for the multi segmented pier.....	74
Figure 5.9:	Experimental versus predicted backbone curves for the singly segmented bents.....	75
Figure 5.10:	Experimental versus predicted backbone curves for the multi segmented bents.....	76
Figure 5.11:	Effects of changing the applied post-tensioning forces on the backbone curves of piers having different aspect ratios.....	77
Figure 5.12:	Effects of different combinations of axial stresses for piers with different aspect ratios.....	78
Figure 5.13:	Effects of piers aspect ratios on the backbone curves.....	79
Figure 5.14:	Backbone curves for two piers having different aspect ratios	80
Figure 5.15:	Backbone curves for piers from the S series (dashed line) and L series (solid line) with different heights.....	81
Figure 5.16:	An approximate mechanism for rocking of two piers having the same height but with different cross sectional diameter.....	81
Figure 5.17:	Backbone curves for piers of the L series constructed using different FRP	82

	materials.....	
Figure 5.18:	Backbone curves for piers of the S series constructed using different FRP materials.....	82
Figure 5.19:	The stress-strain relationships for piers from the S and L series confined using different FRP materials.....	83
Figure 6.1:	FE model for a SPPT pier used in this study.....	89
Figure 6.2:	Deformed shape of the pier.....	90
Figure 6.3:	Compressive stress strain relationship obtained from Samaan et al. (1998) to model the GFRP confined concrete of the piers.....	92
Figure 6.4:	Backbone curve along with its bilinearized form (FEMA 356).....	96
Figure 6.5:	The yield load associated with each specific pier	98
Figure 6.6:	The performance load associated with each specific pier.....	101
Figure 6.7:	The lateral drift angle vs. the error in predicting the pier's strength.....	102
Figure 6.8:	The relationship between the lateral drift angle (%) vs. the stress in the post-tensioning tendon's normalized by its initial stress for piers.....	104
Figure 6.9:	Error in predicting the post-tensioning stress in the tendons Vs. lateral drift angle.....	106
Figure 6.10:	Flow chart diagram of the proposed design procedure for SPPT piers.....	108
Figure 6.11:	A diagram showing how to obtain the target periods of the pier from the uniform hazard displacement spectra of the Seattle, WA area.....	109
Figure A.1:	Test setup for computing concrete characteristic strength f'_c	117
Figure A.2:	Test setup for computing static modulus of elasticity of the concrete cylinders.....	118
Figure A.3:	Stress strain curves from the cylinders tests along with the equations of the trend lines.....	119
Figure A.4:	Copy of the report supplied by the DYWIYDAG company.....	120
Figure A.5:	Copy of the compression testing report of the FRP.....	123

CHAPTER ONE

INTRODUCTION

The use of precast segmental construction for concrete bridges in the United States has increased in recent years due to the demand for shortened construction periods, low environmental impacts and the desire for innovative designs that result in safe, economical and efficient structures. However, the behavior and performance of precast segmental bridges during earthquakes is of concern, and consequently their widespread use in moderate to high seismic regions such as the West Coast of the United States is limited.

1.1 Innovative Precast Post-tensioned Bridge Piers and Bents Developed at Washington State University

During the last few years, an innovative segmental precast post-tensioned bridge construction system was developed at Washington State University. The piers of the developed system consist of segmental concrete filled fiber reinforced polymer tubes (SPPT-CFFT), superimposed one on top of the other, and then connected structurally with vertical post-tensioned tendons passing through ducts located in the precast segments. The tendons are anchored in the foundation of the pier and in the bent cap at the pier top Fig. 1.1. Constructing bridge piers in this manner offers several structural, construction and environmental advantages over conventional R.C. designs.

1.1.1 Structural Advantages

A schematic deformed shape of the SPPT-CFFT segmental pier under transverse loading is shown in (Fig. 1.1). The post-tensioning load keeps the whole system as one unit. Under

lateral loads, the stresses under the precast segments start to be a combination of the normal force induced by prestressing and moment induced by the lateral load. Once the stresses reach a zero value at a point under a segment, any increase in the lateral load leads to an opening between that segment and the one beneath it. This opening continues to propagate with the load increase until it reaches the prestressing bars at the G.C. of the cross section. This is when the post-tensioning steel bar is stretched and the stress in the tendons increase. The fact that the opening between the components propagates means that the stiffness of the system decreases and as a result the energy absorbed from the seismic event decreases.

The tendon is unbonded over the height of the pier so incremental stresses and strains are not concentrated at the crack. This is the reason why unbonded tendons are chosen for this system, and if the initial prestress level is well chosen, the prestressing steel will not yield. This is essential for this system for several reasons. First, the ability to transfer shear forces across the segments interfaces by shear friction is dependent on the clamping force provided by the prestressing tendon. The pier stiffness depends on the prestressing force and hence is not reduced drastically if the prestress is maintained. Finally, the restoring force (self-centring ability) is provided to the pier if the prestress is maintained during and after the earthquake ensuring that the pier returns to the undeformed position.

SPPT-CFFT piers and bents have an encouraging behavior under seismic loads, as the residual pier drift will be negligible, and damage in the form of concrete spalling is minimal and limited to the region near the compression toe of the pier. Yielding of longitudinal bars, which is typical of R.C. piers, will not occur for the precast post-tensioned concrete filled fiber tubes (SPPT-CFFT). This means that a segmental precast concrete bridge pier will remain functional immediately after a moderate to strong seismic event and will require minimal repair. Due to

their exceptional seismic performance, this system would be particularly attractive in bridges considered as lifeline structures.

1.1.2 Construction Advantages

Construction schedules can be shortened significantly since bridge components can be rapidly produced at the precasting facility, where assembly lines and steam curing increase the efficiency of concrete construction. Additionally, the erection of a segmental bridge in the field can proceed rapidly, thus reducing the disruption to existing traffic infrastructure.

1.1.3 Environmental Advantages

Noise, leakage of wet concrete into waterways and fuel consumption due to congestion and rerouting of cars during construction are reduced when using this system. So it reduces sound, water and air pollution if compared to the conventional R.C. systems.

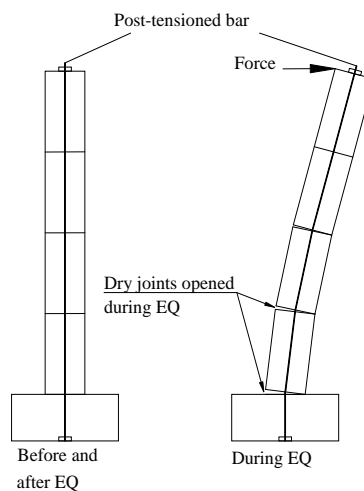


Figure 1.1 Schematic drawing of the SPPT-CFFT System

1.2 Research Objectives

This study started with the development of a FE model capable of capturing the behavior of the segmental precast post-tensioned (SPPT) pier system. The model was calibrated against three different experimental studies with different configurations of the SPPT system. The model was then used to conduct a parametric study to have a better understanding of the effect of different parameters and configurations on the seismic behavior of the SPPT piers. The data collected from a large number of analyzed piers was then used to develop a design procedure for the system using empirical equations.

CHAPTER TWO

LITERATURE REVIEW

2.1 Seismic Behavior of Segmental Precast Post-tensioned Piers

Segmental precast post-tensioned (SPPT) systems in low to medium seismic zones have proven to be an economical and advantageous construction system. Table 2.1 and Fig. 2.1 show examples of bridges constructed in this way. However, little is known about the seismic behavior of SPPT system. Recently, several research projects have investigated the seismic behavior of unbonded and bonded post-tensioned segmental piers.

Table 2.1 Examples of bridges constructed using segmental piers

Bridge	Location	Description
Louetta Road Overpass	Houston, Texas	precast post-tensioned piers
Sunshine Skyway Bridge	Florida	precast PT hollow elliptical pier segments
U.S. 183 Elevated	Austin, TX	Hollow Precast Piers
Varina-Enon Bridge	Virginia	Precast concrete elements for the piers
South Rangitikei Rail Bridge	New Zealand	Rocking bridge pier
Lions Gate Bridge (north approach)	Vancouver	Rocking bridge pier



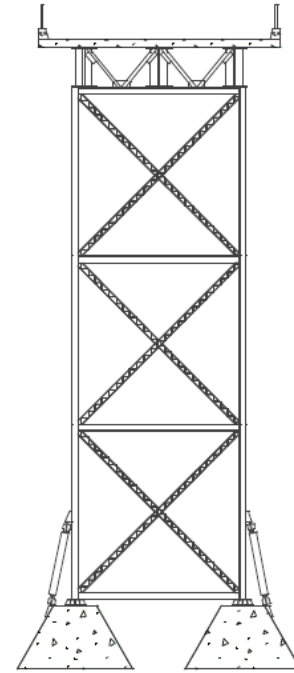
(a)



(b)



(c)



(d)

Figure 2.1 Examples of segmental piers

(a) Louetta Road Overpass,

(b) U.S. 183 Elevated piers during construction,

(c) South Rangitikei Rail Bridge, and

(d) Schematic diagram of the controlled rocking pier used in lions gate bridge

2.1.1 Experimental Studies

Hewes and Priestley (2002) conducted cyclic loading on four, 40% scaled, unbonded segmental post-tensioned piers with different aspect ratios. Each pier was tested twice under low and high initial post-tensioning stress. Two different thicknesses of steel confinement were used for the lower segments only, while the upper segments were reinforced concrete.

Chang et al. (2002) conducted a study on four large-scale hollow precast unbonded post-tensioned reinforced concrete segmented piers. Each specimen consisted of nine or ten 100 cm [39.4 in] tall, precast pier segments.

Chou and Chen (2006) tested two one-sixth scale (16.67%) precast unbonded post-tensioned concrete filled steel tube segmental piers through cyclic loading tests.

Marriott et al. (2009) tested three, one-third scale (33%) piers. Two were segmental piers while the third was of monolithic reinforced concrete (RC) construction as a control specimen.

The previously mentioned efforts highlighted the ability of the system to undergo large lateral displacements with no sudden strength reduction (failure). The reported residual displacements were much lower compared to monolithic RC systems. The low hysteretic energy dissipation capacity, due to the minimal concrete damage, was of concern.

2.1.1.1 Experimental Studies Done At WSU

ElGawady et al. (2010) and ElGawady and Shaalan (2010) studied the performance of segmental precast post-tensioned piers and bents (frames) under cyclic loads. The test matrices of the two studies consisted of four SPPT-CFFT, piers, and frames along with two cast-in-place RC specimens (Figs. 2.2 and 2.3) as control specimens. The segments consisted of plain concrete

cylinders confined by glass fiber reinforced polymer (GFRP) tubes. For each study, one single segment specimen and three multi-segmented specimens were tested (consisted of 4 segments for the piers study and 3 segments for the frames study stacked over each other). Steel angles were used as external fuses for one multi-segmented specimen in each study. Also, rubber pads were used as base isolators for one pier and one frame.



RC pier

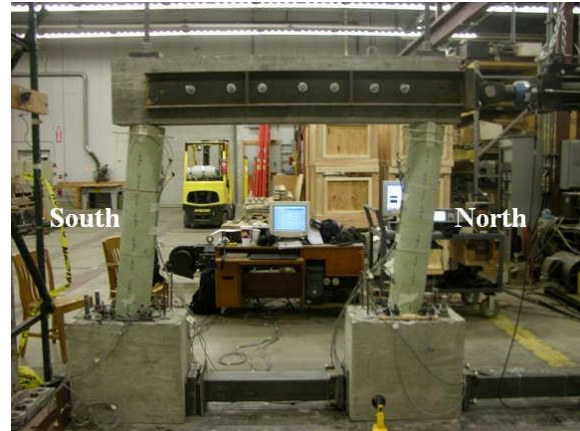


Multi-segmented

Figure 2.2 Piers tested (From ElGawady et al. 2010)



RC



Multi-segmented

Figure 2.3 Tested frames (From ElGawady and Shaalan 2010)

2.1.2 Simple Models

A simplified analytical three-stage model was developed by Hewes and Priestley (2002); their results showed that the model was able to predict the backbone curves of the tested piers quite well.

Ou et al. (2007) used the experimental data obtained by Chang et al. (2002) to develop a simplified analytical model for static pushover analysis as well, but also taking into consideration the presence of longitudinal mild steel reinforcement across the pier segment joints.

ElGawady et al. (2010) attempted to verify the simplified analytical model originally developed by Hewes and Priestley (2002) against their test results. The model overestimated the yield point of the system (Fig. 2.4). To capture the experimental backbone curve, the plastic hinge length definition was changed according to Hines et al. (2001). This proved that the model is not yet accurate enough to capture the behavior of different systems.

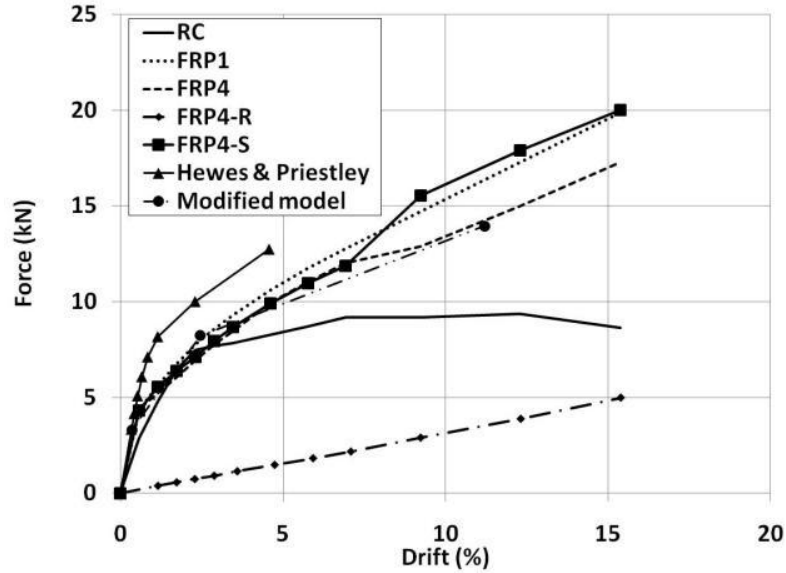


Figure 2.4: Backbone curve of the test specimens, (From ElGawady et al. 2010)

2.1.3 Finite Element Models

A wide range of numerical modeling techniques were used to model the response of segmental piers including 2-dimensional (2D-FEM), 3-dimensional, finite element (3D-FEM), and macro-models (multi-spring models). No 3D-FEM has been developed to model fiber and steel confined segments.

Kwan and Billington (2003 a,b) developed a 2D finite element model to simulate the behavior of partially post-tensioned reinforced concrete bridge piers. They developed models for single pier piers as well as two-pier bents and studied the behavior under monotonic, cyclic, and seismic loads. The material models were verified in the study. However, the overall response of the system was not calibrated.

Ou et al. (2007) also developed a 3D finite element model using the test results of Chang et al. (2002). A cyclic loading pattern was applied to the model to validate the simplified analytical model.

The 2D-FEM and 3D-FEM, at present, are only capable of capturing the general behavior of the segmental piers. Each of the FE models was calibrated against one set of data. Hence, the literature did not include a standard approach to develop a FE model capable of capturing the behavior of different systems layouts, particularly fiber and steel confined. This is the preliminary target of this study.

Marriott et al. (2009) developed and tested the efficiency of two macro-models (multi-spring model). ElGawady and Shaalan (2010) developed a pushover analysis of a segmental frame system using SAP2000. To be able to correctly implement this type of approach, a good physical understanding of the system and its behavior is required in order to implement the correct assumptions and parameters to the model and to be confident in the output.

2.1.4 Lumped-mass Models

In this approach, the piers are assumed to be a single degree of freedom system (SDOF) with a lumped mass at the top. The hysteretic diagrams developed by experimental tests and/or FE models are then modified to an idealized flag-shape hysteretic for the SDOF.

Ou et al. (2007) used the 3D FE analyses and the cyclic test data from Chang et. al (2002) to develop a flag-shaped (FS) model. By assuming that the piers are a lumped-mass SDOF, the response-history of the piers under 25 near-fault ground motions was easily computed in order to study the behavior of the system under seismic loading.

Chou and Hsu (2008) developed FS and stiffness-degrading flag-shaped (SDFS) models according to the hysteretic curves obtained from the cyclic loading of precast post-tensioned segmented piers. Both the FS and SDFS models considered hysteretic energy dissipation. However, only SDFS took the stiffness degradation into consideration. The discrepancy between the results of both assumptions showed the importance of considering stiffness degradation in predicting the dynamic response of the system.

The importance of this approach is that it makes possible a simplified dynamic analysis of the system under seismic excitations. Then it allows the development of the seismic analysis in a fast and economical way, compared with FE analysis.

2.1.5 Energy Dissipation Systems

To overcome the drawback of low hysteretic energy dissipation capacity, additional energy dissipaters were used to increase the hysteretic damping of the system. In most cases hysteretic damping comes from the yielding of the steel element. Energy dissipaters can be divided into two main categories, namely, internal and external (fuses) energy dissipation systems.

Chang et al. (2002) and Ou et al. (2007) used mild steel bars between pier segments as internal energy dissipaters. The bars proved their efficiency by significantly increasing the hysteretic energy dissipation. The major problem with this type of dissipater is that, after yielding, the bars are permanently deformed and the whole system suffers from residual displacement after loading.

External energy dissipaters (fuses) have been used by Chou and Chen (2006), Marriott et al. (2009), ElGawady et al. (2010) and ElGawady and Shaalan (2010).

Chou and Chen (2006) provided one of their piers with a dog bone shaped external energy dissipater. They reported that it increased the equivalent viscous damping of the system from 6.5% to 9%.

Marriott et al. (2009) used two different layouts of external energy dissipater systems for segmental piers. They used mild steel bars encased in steel confining tubes and injected with epoxy to have a fuse-like behavior and to be able to dissipate energy while subjected to tension and compression stresses.

ElGawady et al. (2010) and ElGawady and Shaalan (2010) used external steel angles and rubber pads respectively as external energy dissipaters and isolation dissipation devices. The idea of the steel angles is the same as with other metal dissipaters: energy is dissipated by the yielding of the steel. On the other hand, rubber dissipates energy in another way, as the soft rubber changed the energy dissipation function from a discrete function occurred at every impact between the rocking segments to a continuous function ElGawady et al. (2005 and 2006).

Both internal and external energy dissipaters increased the dissipation of hysteretic energy. The fuses had the advantage of being easily changed and, hence, not increasing the residual drift of the system. Use of the rubber isolation pads significantly decreased the initial stiffness.

2.2 Concrete Confinement

Mander et al. (1988) developed a theoretical model to predict the stress-strain behavior of concrete confined using steel stirrups and/or jackets.

In recent years, external confinement of concrete using FRP composites has emerged as a popular method of both pier retrofit and new construction, particularly for circular piers. Various

models for predicting stress-strain behavior have been developed (e.g., Samaan et al. (1998), Fam and Rizkalla (2001), Becque et al. (2003), Lam and Teng (2002 & 2003), Jiang and Teng (2007) and Teng et al. (2009)).

Confinement increases element ductility and the ultimate strength of the elements. If used in a tubular shape, confinement can be a permanent formwork which can save the time and money spent preparing temporary formworks.

2.3 Conclusions

- Experimental studies show that the permanent deformation of SPPT is minimal compared to that of RC piers.
- Experimental studies show the limited ability of the system to dissipate input seismic energy so additional energy dissipaters were used.
- Energy dissipaters are important for the SPPT system. External fuses don't increase the residual drift, but internal fuses do.
- The simple analytical models can not yet be generalized and need more research to be more accurate.
- 2D and 3D FE modeling is essential in understanding the behavior of the system under different loading patterns. A combination of FE modeling and FS/SDFS models can be an extremely powerful tool to compute the dynamic response of the system without running expensive experimental testing. However, first, a systematic way of preparing a FE model for the system must be developed.

2.4 References

- Booker, A. J. (2008). "Performance of continuous and segmented post-tensioned concrete filled fiber tubes." M.Sc. thesis, Washington State Univ., WA, USA

- Chang, K. C., Loh, C. H., Chiu, H. S., Hwang, J. S., Cheng, C. B., and Wang, J. C. (2002). "Seismic behavior of precast segmental bridge columns and design methodology for applications in Taiwan", Taiwan Area National Expressway Engineering Bureau, Taipei, Taiwan in Chinese.
- Chou, C.-C., and Chen, Y.-C., (2006). "Cyclic tests of post-tensioned precast CFT segmental bridge columns with unbonded strands" J. Earthquake Engng. Struct. Dyn., 35, 159-175.
- Chou, C.-C., and Hsu, C.-P.,(2008)."Hysteretic model development and seismic response of unbonded post-tensioned precast CFT segmental bridge columns." J. Earthquake Engng. Struct. Dyn., 37, 919-934.
- ElGawady, M., Booker, A.J., and Dawood, H., (2010). "Seismic behavior of post-tensioned concrete filled fiber tubes." J. Composites for Construction, ASCE, (to appear in October 2010 issue)
- ElGawady, M., and Shaalan, A., (2010- In review). "Seismic behavior of self-centering bridge bents", ASCE, Journal of Bridge Engineering.
- Hewes, J. T., and Priestley N. (2002). "Seismic design and performance of precast concrete segmental bridge columns." Report No. SSRP-2001/25, Univ. of California at San Diego.
- Kwan,W.-P., and Billington, S. L. (2003). "Unbonded posttensioned concrete bridge piers. I: Monotonic and cyclic analyses." J. Bridge Eng., 8(2), 92–101.
- Kwan,W.-P., and Billington, S. L. (2003). "Unbonded posttensioned concrete bridge piers. II: Seismic analyses." J. Bridge Eng., 8(2), 102–111.
- Marriott., D., Pampanin, S., and Palermo, A., (2009). "Quasi-static and pseudo-dynamic testing of unbonded post-tensioned rocking bridge piers with external replaceable dissipaters" J. Earthquake Engng. Struct. Dyn., 38, 331-345.
- Ou, Y.-C., Chiewanichakorn, M., Aref, A. J., and Lee, G. C. (2007). "Seismic performance of segmental precast unbonded posttensioned concrete bridge columns." J. Str. Eng., 133(11), 1636-1647.
- Shaalan, A. (2009). "Performance of re-centering moment resisting frames composed of continuous and segmented precast post-tensioned concrete columns confined by FRP tubes" M.Sc. thesis, Washington State Univ., WA, USA

CHAPTER THREE

BEHAVIOR OF SEGMENTAL PRECAST POST-TENSIONED BRIDGE PIERS UNDER LATERAL LOADS: EXPERIMENTAL AND MODELING

Haitham Dawood¹ Mohamed ElGawady^{2§} Joshua Hewes³

3.1 Abstract

Segmental precast post tensioned (SPPT) bridge pier is an economic construction system, and a re-centering structural system. Understanding the seismic behavior of a SPPT system is an important step towards its application in high seismic zones. This paper presents a detailed three dimensional finite element model developed using the ABAQUS platform. A brief description and discussion of cyclic tests on eight large scale SPPT piers was also presented. The test investigated the effects of the pier aspect ratio and the initial post-tensioning force on the seismic behavior and the reparability of the tested piers. The effects of confining the bottom segment using steel tubes were also investigated. The experimental work showed that the SPPT pier system is able to withstand large lateral drift angles with minimal damage. The finite element model was validated against the experimental results and it showed good agreement. Finally, sensitivity analyses using the finite element model showed that the model is sensitive to the softening behavior of the concrete material constitutive law.

3.2 Keywords

Finite element method, concrete, precast, post-tensioned, bridge construction, piers

¹ Graduate Research Assistant, Dept. of Civil and Environmental Engineering, Washington State University, Pullman, WA, hmousad@msn.com

² Assistant Professor, Dept. of Civil and Environmental Engineering, Washington State University, Pullman, WA, melgawady@wsu.edu;

[§]Corresponding author

³ Assistant Professor, Dept. of Civil and Environmental Engineering, Northern Arizona University, Joshua.Hewes@NAU.edu

3.3 Introduction

Correctly designed and detailed reinforced concrete structures, under the prevailing capacity design concepts, are anticipated to exhibit inelastic response leading to structural damage and permanent residual drift angles at the conclusion of severe ground motion excitations. This leads to long-term closure of highways while expensive retrofits, or even complete replacements, are carried out. Following the Kobe earthquake (Japan 1995), over 100 reinforced concrete bridge piers were demolished due to a residual drift angles in excess of 1.5% (Lee and Billington 2010).

Recent research on the seismic behavior of segmental precast post-tensioned (SPPT) bridge piers has shown that they display less residual displacement and damage when compared to conventional reinforced concrete (RC) bridge piers (e.g., Hewes 2002, Ou et al. 2007, Marriott et al. 2009, ElGawady et al. 2010 and ElGawady and Shaalan 2010). The potential benefits of using precast post-tensioned structural elements in high seismic zones were highlighted in the U.S. PRESSS research program where a self-centering system that was implemented with precast elements demonstrated superior seismic performance (Priestley et al. 1999).

A segmental precast pier consists of precast segments stacked on top of each other. The segments are connected by unbonded post-tensioning tendons passing through a duct cast in the segments during fabrication. The pier's segments will rock back and forth during ground motion excitation and re-center upon termination of the shaking as a result of the restoring force provided by the post-tensioning.

The effect of pier aspect ratio, applied initial post-tensioning force, applied external axial load, and solid or hollow core cross sections as well as confinement of the segments using steel

stirrups, steel tubes, and/or fiber reinforced polymer tubes on the seismic performance of SPPT piers has been investigated (e.g. Chang et al. 2002, Hewes 2002 and Ou et al. 2007, Marriott et al. 2009, ElGawady et al. 2010(a), ElGawady et al. 2010(b), and ElGawady and Shaalan 2010). These studies showed that SPPT piers were capable of withstanding large nonlinear displacements without experiencing significant or sudden loss of strength. The nonlinear behavior resulted not only from material nonlinearity, like in a conventional RC system, but also from geometric nonlinearity resulted from opening of the interface joints between segments as well as between the bottommost segment and the foundation. The significant contribution of the geometric nonlinearity to the nonlinear behavior of the SPPT piers resulted in smaller damage and residual displacement compared to their counterpart RC piers at a given lateral drift angle.

Currently, SPPT pier construction is an economical option to accelerate bridge construction in regions of low seismicity in the USA. Examples of bridges constructed with segmental piers include the Louetta Road Overpass (SH-249, Texas), Linn Cove Viaduct (Grandfather Mountain, North Carolina), Sunshine Skyway Bridge (I-275, Florida), Varina-Enon Bridge (I-295, Virginia), John T. Collinson Rail Bridge (Pensacola, Florida), Seven Mile Bridge (Tallahassee, Florida), and the Chesapeake and Delaware Canal Bridge (St. Georges, Delaware). However, the applications of this construction system in moderate to high seismic regions in the USA are limited due to concerns about its seismic response and low energy dissipation capabilities.

In an effort to increase the energy dissipation capacity of SPPT piers, researchers have investigated the influence of internal bonded mild steel bars at the interfaces between the segments as well as between the bottommost segment and foundation (Chang et al. 2002). However, the yielding of the mild steel bars increased residual displacements and damage

compared to piers without mild steel. External energy dissipaters “fuses” have also been investigated as a means of enhancing energy dissipation (Chou and Chen 2006, Marriott et al. 2009, Rouse 2009, ElGawady et al. 2010(a), ElGawady et al. 2010(b), and ElGawady and Shaalan 2010). These external simple yield-dissipaters significantly increased the energy dissipation with minor effects on the residual displacement of the system.

This paper presents a detailed three dimensional (3D) finite element (FE) model developed using ABAQUS/Standard version 6.8-2 to capture the backbone curves of SPPT piers. The paper starts with a detailed description of the FE model including the element types used, material constitutive models, loading patterns, boundary conditions, and contact interaction properties. Then, a discussion of an experimental study conducted on eight large scale SPPT piers subjected to static-cyclic loading is presented. The developed model was validated against the results of this experimental research. Finally, sensitivity analyses were carried out.

3.4 Finite Element Modeling of Self-Centering Piers

ABAQUS/Standard version 6.8-2, a general purpose finite element code, was selected as a basic platform for this study. For the simulation of the SPPT pier system a built-in first-order full integration 8-node linear brick element (C3D8) was used to represent the concrete and the confining material in the model (Fig. 3.1). A 2-node linear beam element in space (B31) was used to simulate the post-tensioning tendon. The mesh size was selected based on a sensitivity analysis such that the analyses converge to the same output while maintaining a reasonable computation effort.

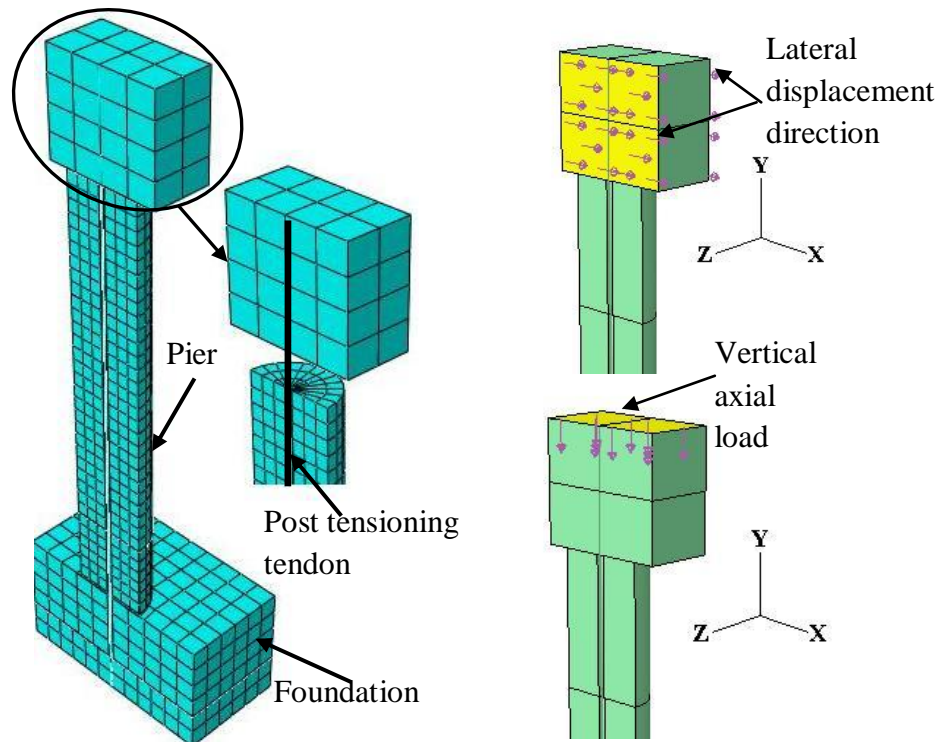


Figure 3.1: A typical mesh and applied loads and displacements for the SPPT pier.

Concrete damaged plasticity and concrete smeared cracking are the two models available in ABAQUS/Standard 6.8-2 to model concrete material behavior. The concrete damaged plasticity model (Lubliner et al. 1989 and Lee and Fenves 1998) assumes that the main two concrete failure mechanisms are the tensile cracking and compression crushing of the concrete material. Crack propagation is modeled by using continuum damage mechanics, i.e., stiffness degradation. The damaged plasticity model was selected to be used in this study since it has higher potential for convergence compared to concrete smeared cracking. Moreover, the concrete damaged plasticity model is designed for applications in which the material is subjected to monotonic, cyclic, and/or dynamic loading, which gives the model the potential to be applied under different loading types.

To fully define the concrete material it is required to define material density, Young's modulus, Poisson's ratio and the concrete damaged plasticity model parameters. The definition of the concrete damaged plasticity model requires the definition of the plasticity parameters, as well as compressive and tensile behavior. The five plasticity parameters are: the dilation angle in degrees, the flow potential eccentricity, the ratio of initial equibiaxial compressive yield stress to initial uniaxial compressive yield stress, the ratio of the second stress invariant on the tensile meridian to that on the compressive meridian, and the viscosity parameter that defines viscoplastic regularization. The aforementioned parameters were set to 1°, 0.1, 1.16, 0.66, and 0.0, respectively. The values of the last four parameters were recommended by the ABAQUS documentation for defining concrete material (ABAQUS version 6.8 documentation- SIMULIA 2008). The dilation angle was chosen to be unity to give stability to the material model while minimizing the confinement effect of the material as the confinement effects were taken independently into consideration while getting the stress strain curves of the confined concrete. For a given concrete characteristic compressive stress at 28 days (f'_c) and confinement characteristics (thickness, material's type, and properties) the concrete stress strain curve in compression can be developed using a suitable confined concrete model. (e.g., Mander et al. 1988, Samaan et al. 1998, Fam and Rizkalla 2001, Beque et al. 2003, and Teng et al. 2009).

The concrete Young's Modulus can be either measured according to ASTM (C469) or calculated using Eq. 3.1 (ACI318-2008).

$$E_c = 4733 \sqrt{f'_c} \text{ MPa} [57,000 \sqrt{f'_c} \text{ psi}] \quad (\text{Eq. 3.1})$$

The concrete behavior in tension was modeled using a linear elastic approach until cracking is initiated at f'_t where f'_t is defined using Eq. 3.2 (ACI318-2008), followed by a

horizontal plateau. This horizontal plateau was used to improve the numerical stability and convergence of the model (Wight 2006).

$$f_t = 0.62276 \sqrt{f'_c} \text{ Mpa} \quad [7.5 \sqrt{f'_c} \text{ psi}] \quad (\text{Eq. 3.2})$$

The concrete compressive and tensile behaviors were inputted to the program using a tabulated form of yield stress versus inelastic strain and yield stress versus cracking strain respectively (ABAQUS version 6.8 documentation- SIMULIA 2008).

The constitutive model used to simulate the steel tendons and steel jackets was the classical metal plasticity model. An idealized elasto-plastic stress strain curve for each material was developed and used as the input for the ABAQUS model. The input for the classic metal plasticity model includes density, Young's Modulus, Poisson's Ratio and the yield stress versus plastic strain submitted in a tabular form.

The three translational (Ux, Uy, Uz) degrees of freedom (DOF) were constrained for all the nodes at the bottom surface of the foundation (Fig. 3.1). Since the pier is symmetric with respect to an XY plane, a symmetry (ZSYMM) boundary condition was used along the plane of symmetry to reduce the analysis time.

The post-tensioning tendons in the model are embedded at the top into a loading stub representing the bridge superstructure and at the bottom into the foundation (Fig. 3.1). The normal contact behavior between the concrete surfaces and between the confining steel tube and the concrete segments was modeled using the default constraint enforcement method with a hard contact pressure-over closure having finite sliding with node to surface as the discretization method. The penalty method was chosen to formulate the tangential contact behavior between different surfaces of the model.

Three loading steps were used for the analysis of the models. During the first step, a post-tensioning force was applied using a stress-type initial condition to the tendons. During the second step, the gravity load was applied as a traction force applied to the top surface of the model in the negative y-direction (Fig. 3.1). The third loading step consisted of a monotonic push in the x-direction simulated by a linearly increasing lateral displacement until the failure of the model occurs and the analysis was not able to proceed any further.

3.5 Experimental Work

3.5.1 Test Pier Design Details

Four large-scale precast concrete segmented piers (Table 3.1) were constructed and tested at the Powell Structural Research Laboratories on the University of California at San Diego (UCSD) to investigate their strength – deformation characteristics and failure modes under simulated lateral seismic loading (Hewes 2002). The following primary features were investigated in the experimental program: (1) Pier aspect ratio, (2) Lateral confinement level at the maximum moment location, (3) Initial tendon stress, and (4) Damage reparability. The piers were circular in cross-section with diameter of 610 mm [24 in], and the main longitudinal reinforcement in each pier consisted of a single unbonded concentric tendon comprised of 27 – 12.7 mm [0.5 in] diameter ASTM A779 Grade 270 (1860 MPa [270 ksi]) low-relaxation steel prestressing strands with a total cross-sectional area of 2665 mm² [4.13 in²]. Two test piers had an aspect ratio (AR) of 6, and the other two piers had AR = 3, where aspect ratio is defined as the height between point of lateral loading and pier base divided by pier diameter.

Table 3.1: The matrix of the experimental work

Pier	Pier aspect ratio	No. of segments	Steel jacket thickness	Initial tendon's stress / ultimate tendon's tensile stress	Measured post-tensioning stress MPa [psi]
JH11 [*]	6	4	6.0 mm [0.24 in]	40%	1021 [148,090]
JH12 ^{**}				60%	1215 [176,238]
JH21 [*]	6	4	2.8 mm [0.11 in]	40%	801 [116,200]
JH22 ^{**}				60%	946 [137,210]
JH31 [*]	3	2	2.8 mm [0.11 in]	40%	773 [112,114]
JH32 ^{**}				60%	1020 [147,939]
JH41 [*]	3	2	6.0 mm [0.24 in]	40%	779 [112,984]
JH42 ^{**}				60%	1002 [145,328]

^{*} Virgin specimens

^{**} Retested specimens after retrofitting

The bottommost segment of each pier utilized an ASTM A569, A36 steel jacket to provide the relatively high level of lateral confinement which is required due to the high compression strains associated with a pier rocking about its base. For each aspect ratio, one pier used a jacket with a transverse volumetric reinforcing ratio of $\rho_v = 1.9\%$ and the other with $\rho_v = 3.9\%$. The steel jacket terminated approximately 25 mm [1.0 in] above the bottom of the segment to prevent the jacket from bearing on the footing during testing. The height of the steel jackets in all piers was selected such that spalling of cover concrete in the non-jacketed segments above it would be avoided. The jacketed segments did not contain any longitudinal reinforcement other than the prestressing tendon. Table 3.2 gives the jacket tensile properties and Table 3.3 gives the concrete compressive strength measured for each pier at the 28th day and the day of testing.

Table 3.2: Summary of steel coupons tension tests

Piers	Description	Size	Yield Strength (MPa)	Ultimate Strength (MPa)
JH1 and JH2	Thin coupons	2.9 mm thick	283 ± 7	390 ± 7
	Thick coupons	6.2 mm thick	303 ± 3	464 ± 3
JH3 and JH4	Thin coupons	2.8 mm thick	290	364
	Thick coupons	6.0 mm thick	317	463

Table 3.3 Concrete compressive strength for test units
(f_c' , MPa)

Pier	28-Day	Day of Test 1	Day of Test 2
JH1	44.0 ± 0.3	48.7 ± 0.6	57.0 ± 1
JH2		50.8 ± 1.1	55.5 ± 1
JH3	48.5 ± 1.1	57.3 ± 1.6	57.1 ± 0.8
JH4		58.1 ± 1.1	57.8 ± 1.7
Footing	49.5 ± 1	61.4 ± 1	--

All other pier segments above the base segment used traditional transverse spiral rebar for lateral confinement. The transverse spiral was Grade 60 #3 bar spaced at 75 mm [3.0 in] and 150 mm [5.9 in] for piers with $AR = 6$ and $AR = 3$, respectively. The upper non-jacketed segments also contained eight Grade 60 #4 longitudinal bars spaced evenly around the perimeter of the section with a cover of 25.4 mm [1.0 in]. Test piers JH1 and JH2 had a total of four precast piers segments while JH3 and JH4 had two precast segments each. The unbonded tendon length was $L_t = 4953$ mm [195 in] for JH1 and JH2, while that for JH3 and JH4 was $L_t = 3137$ mm [123.5 in].

In order to investigate the influence of initial tendon stress level on pier behavior, and to evaluate how well a pier could be repaired after a seismic event, each pier was tested twice. The first test on each pier was conducted at a given initial tendon stress, and then each pier was inspected, repaired, and post-tensioned to a higher initial tendon stress level for the second test. Table 3.1 provides a summary of pier test data including initial tendon stress level.

3.5.2 Test Setup, Instrumentation, and Loading Protocol

A schematic representation of the test setup is shown in Fig. 3.2. Pier footings were connected to the laboratory strong floor by six high strength post-tensioning bars, and a cyclic lateral point load was applied at the pier top by a servo-controlled hydraulic actuator reacting off the laboratory strong wall. Horizontal load levels in the actuator were monitored using a load cell, and the horizontal displacement at the actuator level was measured using a displacement transducer and reference pier. A constant axial compressive force of 890 kN [200 kips] was applied to the piers to simulate gravity service loads.

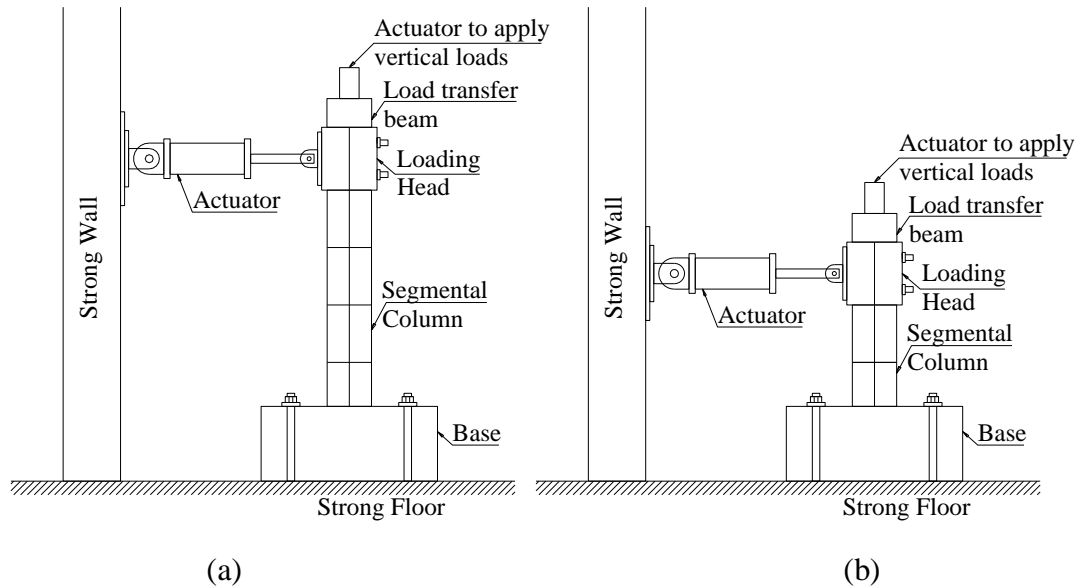


Figure 3.2: Test setup for specimens
(a) Specimens (JH11/JH12/JH21/JH22), and (b) Specimens (JH31/JH32/JH41/JH42).

The first few cycles of each test were conducted in the elastic range under force control, with one cycle each performed at one-half, one, and one and a half times the theoretical force to cause decompression of the extreme tension fiber at the pier base. Subsequent cycles during the test were conducted in displacement control, with three full displacement reversals conducted at increasing amplitudes. Since each pier was to be tested twice, it was desired to limit the damage

in the first test of each pier to an amount that could be repaired relatively easily. Thus the maximum drift imposed during the first test of each specimen was dictated by the observed damage at a particular drift.

3.5.3 Description of Test Results

All test piers exhibited ductile flexural response up to the maximum imposed drift of each test, as is visible in the hysteretic force – displacement response plots shown in Figs. 3.3 and 3.4. A prominent feature of piers with unbonded tendons is the recentering tendency, which also implies less hysteretic energy dissipation compared to a traditional reinforced concrete pier. Initial concrete crushing was observed at the region in the bottommost segment between the bottom of the steel jacket and top of footing at a drift angle of 1.2% for all piers during their first test. However, the extent of spalling was minor and the damage to this region was very limited during the first tests. After drift angle levels of about 0.5%, pier top displacement was observed to be primarily due to rotation of the pier about the compression toe. This was evidenced by a large flexural crack opening of the interface joint between the pier and its foundation with no significant flexural crack openings above the footing level.

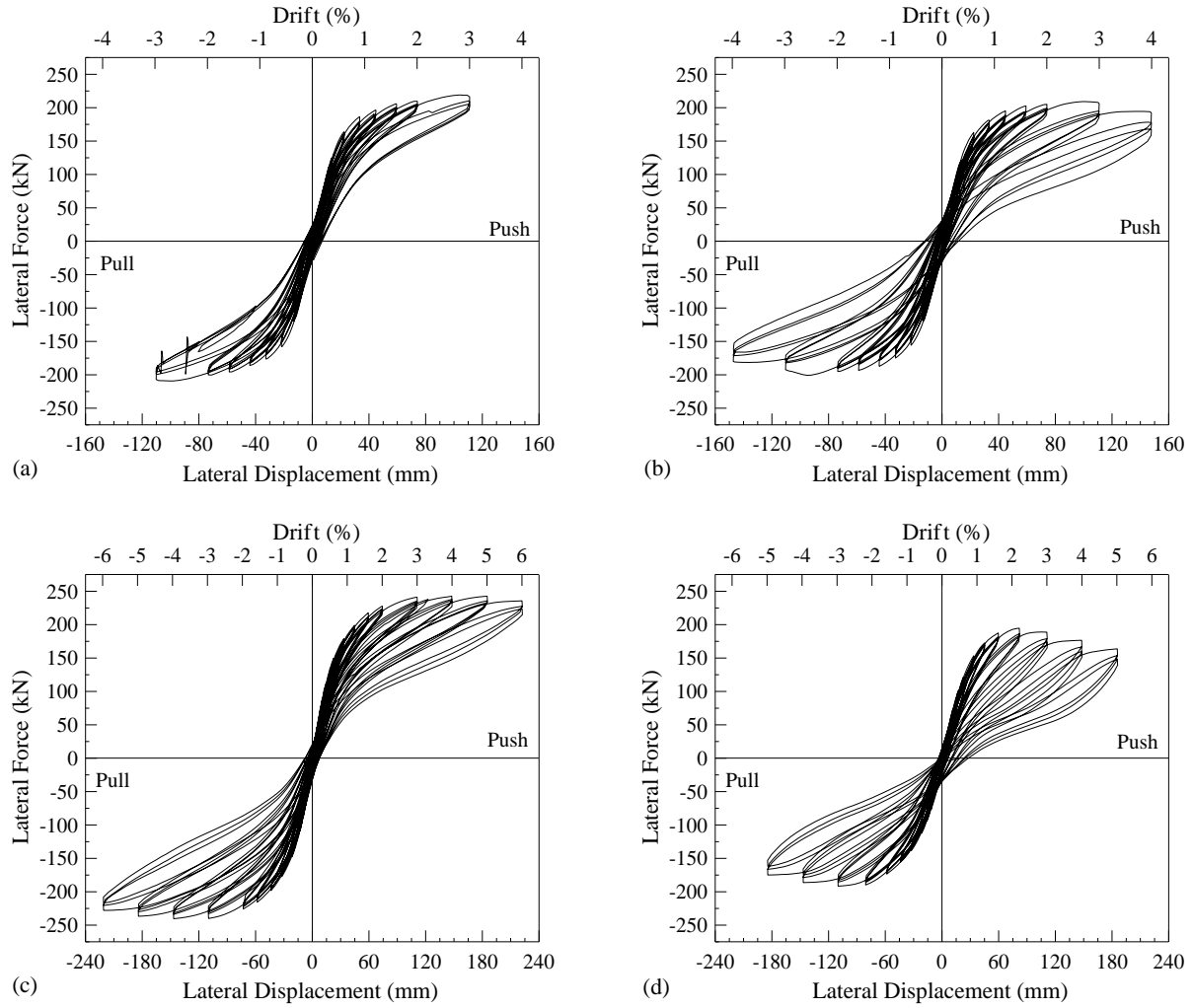


Figure 3.3: Experimental hysteretic response plots: (a) JH11; (b) JH21; (c) JH12; and (d) JH22

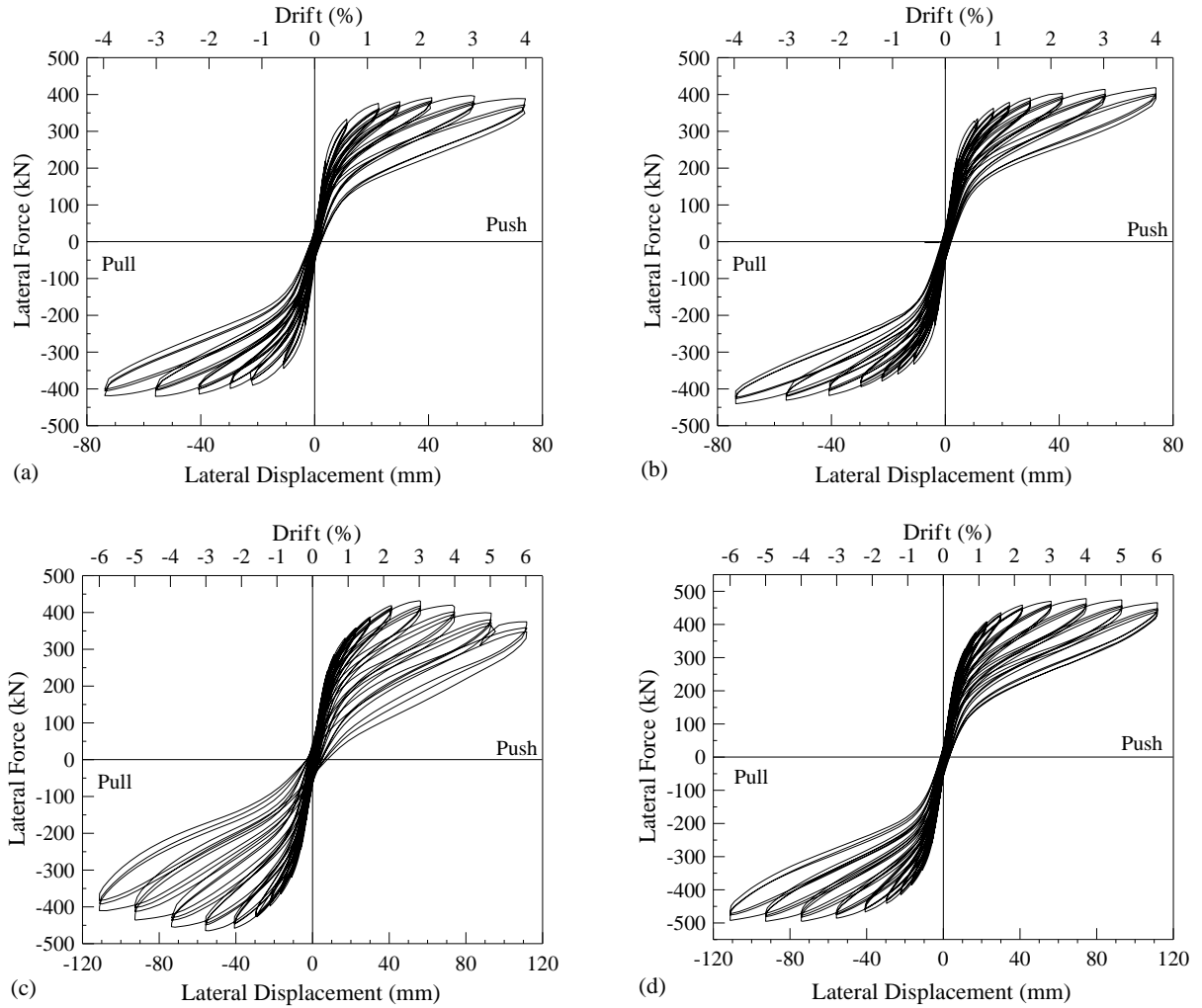


Figure 3.4: Experimental hysteretic response plots: (a) JH31; (b) JH41; (c) JH32; and (d) JH42

During the first tests on piers JH1 and JH2 ($AR = 6$), crushing of cover concrete in the segment directly above the jacketed segment was observed at lateral drift angles of 3.0%, and 4.0%, respectively. The first tests for these piers were stopped at these drift levels. Piers with $AR = 3$ were taken to a maximum lateral drift angle of 4.0% during the first tests. No spalling of cover concrete above the jacketed segment was observed for piers JH3 and JH4. Visible damage to JH3 and JH4 at the end of the first tests consisted of only minor crushing of concrete at the gap between steel jacket and top of footing. For all piers, a residual gap opening on each side of

the section at the pier base (i.e. the compression toe region) existed at the end of testing as a result of very high compression strains and concrete crushing. Residual pier drift angles at the end of testing were on the order of 0.1% for piers JH1, JH3, and JH4, while that for JH2 was 0.30%.

The damaged regions at the pier base and above the jacket (piers JH1 and JH2) were repaired after the first test. Loose concrete was removed, and the regions were scrubbed with a wire brush, rinsed with water to remove any remaining concrete particles, and then allowed to dry. The spalled cover concrete above the steel jacket was reinstated by patching the area with a non-sag polymer-modified, Portland cement mortar. The residual crack at the base of each pier was grouted using a high-modulus, low-viscosity, high-strength epoxy resin adhesive. After the spalled regions in piers JH1 and JH2 were repaired, the lower half of the second segment was wrapped with five layers of fiberglass in an effort to prevent spalling of cover concrete during the second test. Five layers of the Tyfo® Fibrwrap® SEH-51 fiber reinforced polymer (FRP) (Table 3.4) were applied. Each continuous band was installed with a 152 mm [6.0 in] minimum overlap back onto itself.

Table 3.4: Properties of the FRP

Tensile strength	3.24 GPa [470,000 psi]
Tensile modulus	72.4 GPa [10.5×10^6 psi]
Ultimate elongation	4.5%
Density	2.55 g/cm ³ [0.092 lb/in ³]
Thickness	0.36 mm [0.014 in]

The initial stiffness of the piers during their second test was much less than that predicted for an undamaged pier, indicating that the repair measures did not fully restore the piers to an undamaged state (see Figs. 3.3 and 3.4). However, the piers in general exhibited satisfactory

lateral strength –deformation behavior. Piers JH1, JH3 and JH4 achieved a maximum drift angle of 6% while testing of JH2 was terminated at 5% drift angle. The 6% maximum imposed drift during testing corresponded to the maximum displacement limit of the test setup. Comparing the second test hysteretic responses (Figs. 3.3 and 3.4 (c) and (d)), it is seen that piers with the higher jacket confinement level (JH1 and JH4) experienced less damage at their bases, achieved higher lateral strengths, and showed less stiffness and strength degradation at high drifts. Pier JH1 (AR=6) experienced a 6% decrease in lateral strength going from 5% drift to the maximum imposed drift, while JH4 (AR=3) did not show any reduction in strength up to the maximum imposed drift angle level. Specimen JH2 experienced a 20% decrease in strength at maximum drift angle while JH3 suffered a 13% drop in lateral capacity at 6% drift angle. Residual drift angles for JH1, JH3, and JH4 at the end of the second testing were about 0.2%, while that for JH2 was 0.7%. No spalling of cover concrete above the steel jackets was observed during the second tests on the piers.

3.6 Model Validation

The sizes of the elements chosen for the concrete segments, concrete base, and upper loading stub were 94, 127, and 130 mm [3.7, 5 and 9 inches], respectively. The slender pier's model includes 1720 continuum elements, 174 beam elements and a total of 3086 nodes, while the squat piers' model includes 1072 continuum elements, 102 beam elements and a total of 1974 nodes.

The passive confining stresses imposed by the steel stirrups, steel tube, and the FRP sheets on the concrete core during loading alter its stress strain behavior by increasing both its peak strength and ductility. Through this study, Mander et al.'s (1988) and Samaan et al.'s

(1998) models were used for developing the stress-strain behavior of concrete confined using steel and FRP wrapping, respectively.

The concrete compressive strengths in Table 3.3 were implemented in the model. Concrete was defined using a density of 2214 kg/m^3 [138 lb/ft^3] and a Poisson's ratio of 0.2. The stress strain curves in compression of the segments confined by thick steel tube, thin steel tube, steel stirrups and FRP is shown in Fig. 3.5. For more details about developing these curves and the ABAQUS input vectors refer to (Dawood 2010).

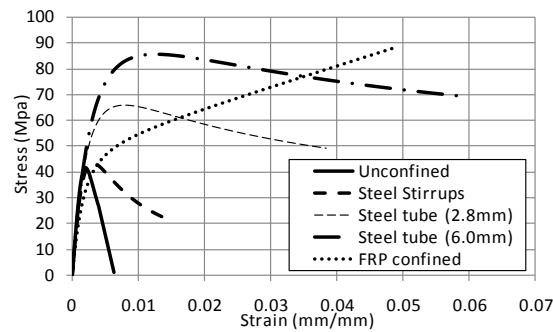


Figure 3.5: Stress strain curves for unconfined and confined concrete.

The steel tubes used to confine the lowermost segments in the specimens were defined using density of 7840 kg/m^3 [0.28 lb/in^3], Poisson's ratio of 0.3, modulus of elasticity of $200,000 \text{ MPa}$ [29000000 psi], while yield stress and ultimate stress were as shown in Table 3.2. The tendon material was modeled using a density of 7840 kg/m^3 [0.28 lb/in^3], Poisson's ratio of 0.3, and modulus of elasticity of $196,500 \text{ MPa}$ [$28,500 \text{ ksi}$], yield stress of 1690 MPa [$245,000 \text{ psi}$] and ultimate stress of $1,730 \text{ MPa}$ [$270,000 \text{ psi}$]. The characteristics used for the FRP used for the retrofitted piers JH12 and JH22 are listed in Table 3.4.

Coefficients of friction of 0, 0.5, and 0.5 were selected between the post-tensioning bar and the duct, steel tubes and segments' surfaces, and two concrete surfaces, respectively. An external axial vertical stress of 3.07 MPa [445 psi], corresponding to approximately 7.4% of f'_c ,

was applied to the top surface of the piers at the loading stub to represent the service load acting on the bridge's superstructure.

3.7 Analyses results

The FE models were able to capture the behavior of the eight specimens described previously (Fig. 3.6). While applying the lateral load, the lateral displacement of the pier increased approximately linearly while all the interface joints between the different segments remained intact. This linear behavior continued until the normal stress under the heel of the pier reached zero (neutral axis at the edge of the cross section). Beyond that, the first opening at the interface joint between the foundation and the bottommost segment was observed and softening in the stiffness was observed as well. While increasing the lateral load, the neutral axis continued to move through the pier's cross section towards its geometric centroid, and the opening of the interface joint between the bottommost segment and the foundation increased. Fig. 3.6(b) shows the discontinuity of the normal strains at the interface joints which was expected once the interface joints opened. Once the neutral axis reached the geometric centroid of the pier's cross section, more softening in the stiffness of the system occurred rapidly while the post-tensioning stresses increased rapidly. The same interface joint opening mechanism occurred at the second interface joint between the first and the second segments. However, the neutral axis did not reach the geometric centroid of the pier at this interface joint. Fig. 3.7 shows the different bending stresses and openings at the different interface joints. This behavior is similar to what was observed during the experimental tests.

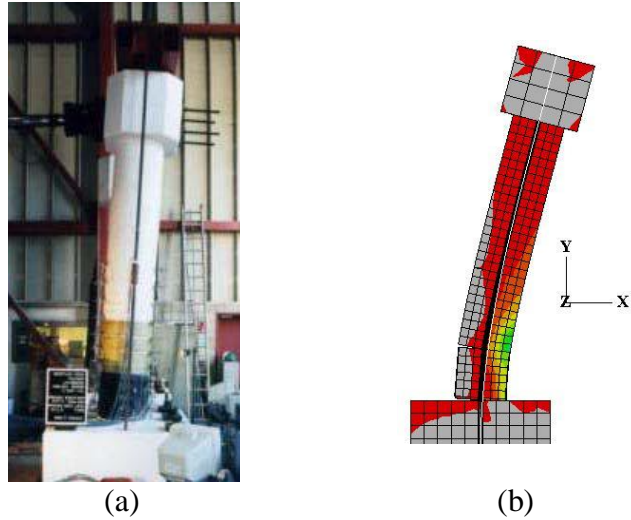


Figure 3.6: Specimen JH12 (a) during testing, and (b) FE model results.

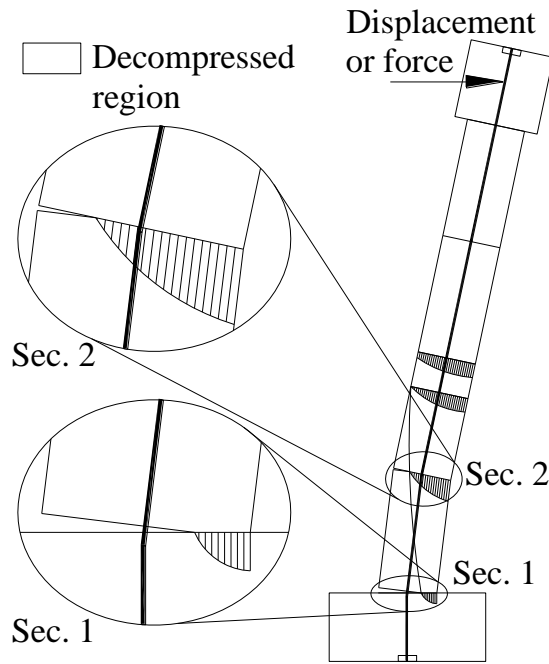
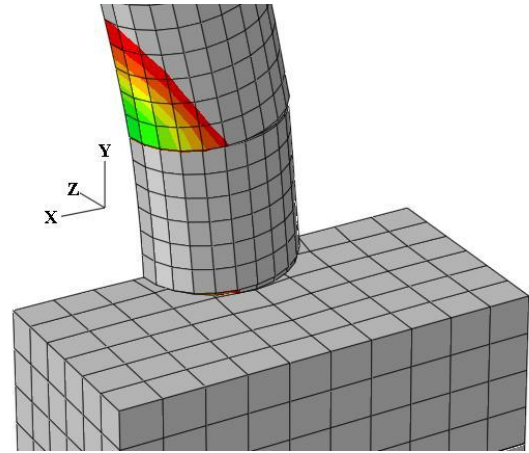
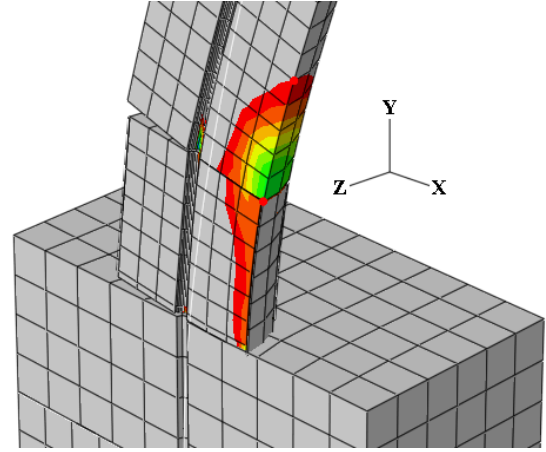
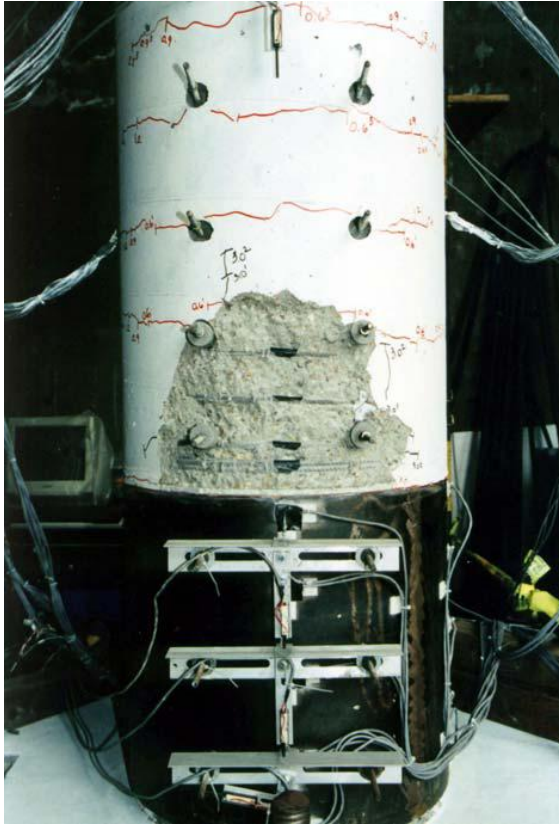


Figure 3.7: A schematic of a rocking pier indicating stresses and strains at different heights of the pier

The FE model was also capable of capturing the damage pattern of the system. For example, the experimental work showed spalling of the concrete cover of specimen JH11 along a height of approximately 406 mm [16 in] at a drift angle of 3%. During the FE analysis of JH11, stress concentrations occurred at the bottom of the second segment, as well as at the top and

bottom of the bottommost segment. At a lateral drift of 3%, since the bottommost segment was confined using the steel jacket, the segment was able to reach high strains without any potential concrete crushing. However, the second segment was a conventional RC segment and the strains in the concrete cover exceeded a potential spalling strain of 0.003 mm/mm along a height of approximately 533 mm [21 in] (Fig. 3.8(b)). Finally, it is worth noting that during the experimental work and at lateral drift of 3%, significant concrete crushing was reported. The analysis showed that the strength degradation of the pier started at a lateral drift of 2.5%.



(a)
Figure 3.8: Specimen JH11 at failure (a) experimental, and (b) analytical.

Figs. 3.9 and 3.10 show the predicted lateral forces versus drift angles and the experimental backbone curves of the slender and squat piers presented in the experimental section, respectively. As shown in the figures, the model was able to capture the general nonlinear behavior of all specimens. The model was able to capture the initial tangent stiffness of all piers. However, the stiffness degradation rate was underestimated for specimens JH12, JH22, JH32 and JH42. The aforementioned specimens were retests of specimens JH11, JH21, JH31 and JH41 after retrofitting and applying a higher post-tensioning stress. This shows that the behavior of the retrofitted piers was affected after the first testing due to micro cracks in the concrete and the retrofitting was not able to fully recover the concrete stiffness. The effect of these micro

cracks wasn't taken into consideration in the FE model. Pier JH11, unlike other piers, was tested up to a drift angle of only 3%, and consequently the extent of micro-cracking in this specimen was not as significant. Hence, out of all the retrofitted specimens, the predicted stiffness degradation for the retrofitted pier JH12 was much closer to the experimental study.

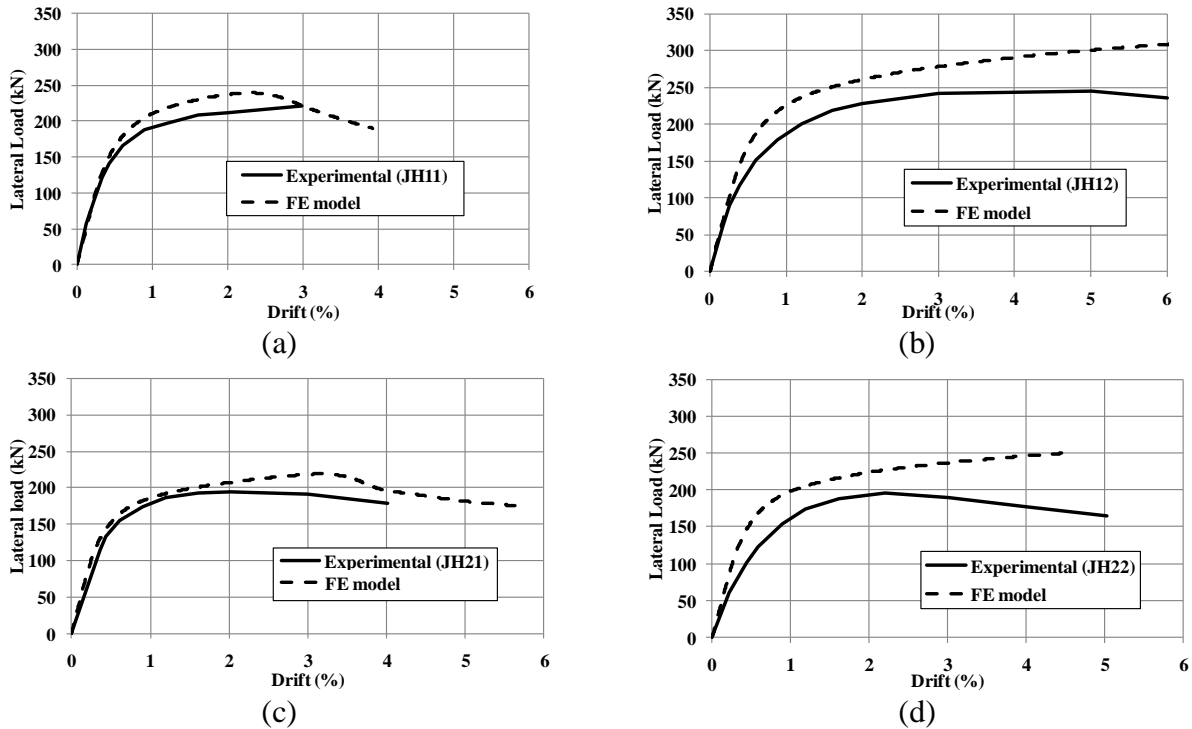


Figure 3.9: Experimental versus predicted backbone curves for slender virgin piers (left) and retested piers (right) (a) JH11, (b) JH12, (c) JH21, and (d) JH22.

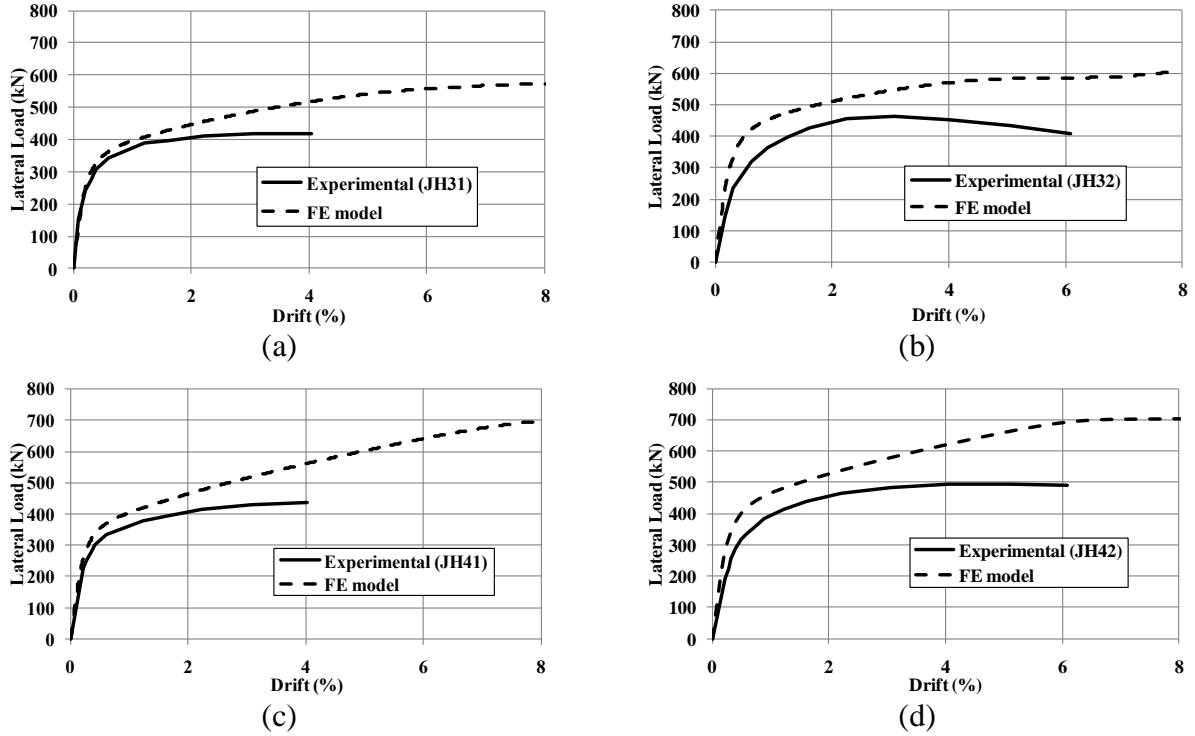


Figure 3.10: Experimental versus predicted backbone curves for squat virgin piers (left) and retested piers (right) (a) JH31, (b) JH32, (c) JH41, and (d) JH42.

Fig. 3.11 shows the error in predicting the lateral force for a given drift angle for each test specimen. The error is defined as follows:

Error in the lateral force (%) =

$$\frac{\text{Numerically determined lateral force} - \text{Experimentally measured lateral force}}{\text{Experimentally measured lateral force}} \% \quad (\text{Eq. 3.3})$$

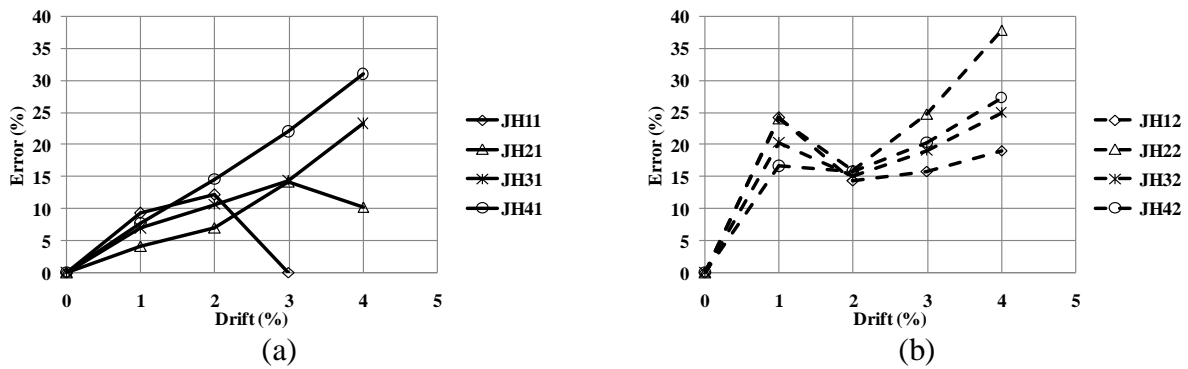


Figure 3.11: Errors in predicting the strengths of (a) virgin piers, and (b) retested piers

As the figure shows, the percentage of error increased with increasing the applied lateral drift angle. For slender specimens that were tested as virgin specimens (JH11 and JH21), the percentage of maximum error was approximately 14%. The error in predicting the strength of piers JH11 and JH21 started to decrease at drifts corresponding to the spalling of the upper segment's cover and it reached approximately 5% at the end of the tests. After retrofitting piers JH11 and JH21 and retesting as piers JH12 and JH22, the maximum percentage of error increased approximately to 17% and 37% for JH12 and JH22, respectively. As mentioned earlier, retrofitting was not able to fully recover the pier's mechanical properties as there were micro cracks that affected the performance of the piers, such micro cracks were not taken into consideration in the FE model. For virgin squat specimens i.e. piers JH31 and JH41, the percentage of error increased approximately linearly with the applied lateral drift angle. At a drift angle of 4% the percentage of error reached 23% and 31% for JH31 and JH41, respectively. For specimens JH32 and JH42, the percentage of error for both was approximately 25% at a drift angle of 4%.

One important parameter for the performance of the SPPT piers is the level of post-tensioning force at different drift angle levels. Fig. 3.12 shows the drift angle level versus the percentage of error, defined by Eq. 3.4, in post-tensioning force. As shown in the figure, the FE model over predicted the post-tensioning forces in most cases. The percentage of error increased with increasing the drifts. Except for specimens JH41 and JH42, the error in predicting the post-tensioning stresses ranged from -6% to +5% for virgin specimens and from -3% to +4% for retested specimens. The error in predicting the post-tensioning force reached approximately 12% for specimens JH41 and JH42. This errors maybe due to a small deviation in defining the

material characteristics and properties such as Young's modulus of the tendon and the concrete, and spalling of the concrete at the toe in the experimental tests.

$$\text{Error in post-tensioning (\%)} = \frac{\text{Numerically determined PT} - \text{Experimentally measured PT}}{\text{Experimentally measured PT}} \% \quad (\text{Eq. 3.4})$$

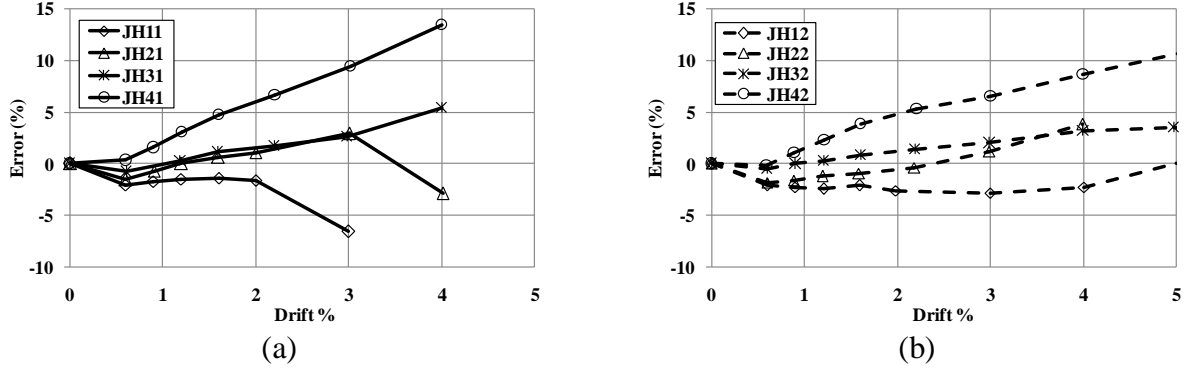


Figure 3.12: Error in post tensioning stress versus drift angle (a) virgin piers, and (b) retested piers

3.8 Sensitivity Analyses

As explained earlier, the mesh size was selected based on several analyses until the solution results converged at a given mesh size which was used in this study. In addition, the effects of confined concrete softening behavior, coefficient of friction between the concrete segments (μ_{c-c}) and coefficient of friction between the concrete and steel tubes (μ_{c-s}) on the predicted backbone curves were examined and presented in this section.

The softening behavior of concrete has an important role in the nonlinear response of RC structures. To investigate the effects of the softening behavior, three different slopes (Fig. 3.13) were implemented in the concrete behavior for the softening curve in the FE models of piers JH11 and JH21. The steepest softening curve is the one by Mander et al. (1988), while the other two softening behaviors were hypothetically assumed with milder stiffness degradations. The two hypothetical slopes were only used in this part of the research to explore the importance of the softening behavior of the concrete material on the ultimate strengths and displacements.

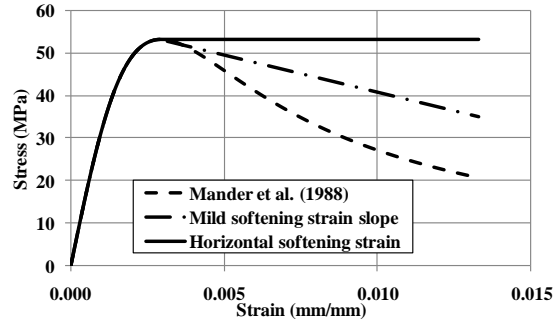


Figure 3.13: Different softening behavior of concrete

Fig. 3.14 shows the backbone curve for specimens JH11 and JH21 using the three different concrete material softening behaviors. As shown in Fig. 3.14, the softening behavior has a significant effect on the ultimate displacement of the investigated piers, as well as the slope of the descending branch of the piers after they reach their peak strengths. Decreasing the rate of the stiffness degradation, i.e. using milder slopes for the softening behavior of the confined concrete, increased the ultimate displacement and strength. Using horizontal softening behavior increased the ultimate displacement to be 175% and 183% of the ultimate displacement when using the steep softening behavior (Mander et al. 1988) for specimens JH11 and JH21, respectively, while in the case of mild softening behavior the ultimate displacement increased to approximately 150% of the ultimate displacement when using the steep softening behavior (Mander et al. 1988) for both specimens.

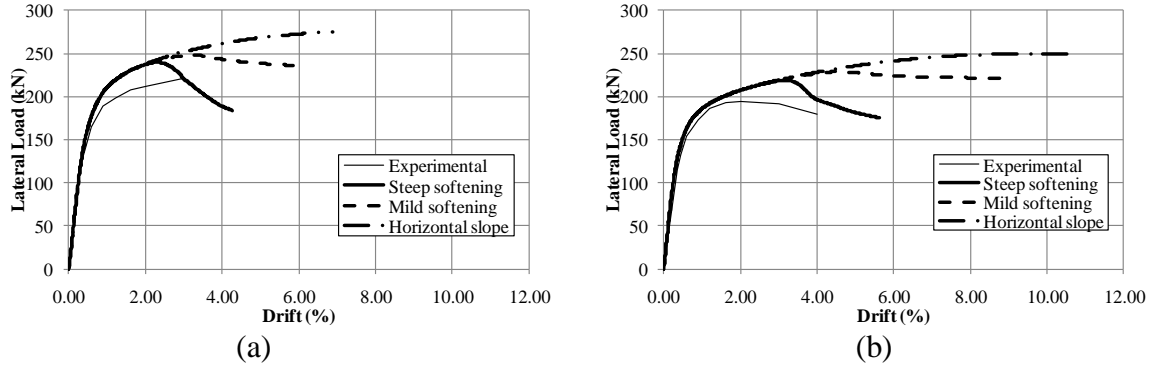


Figure 3.14: The effects of concrete material softening behavior on the response of piers (a) JH11, and (b) JH21

In this manuscript a value of 0.5 was used for μ_{c-c} (coefficient of friction between concrete surfaces) and μ_{c-s} (coefficient of friction between concrete and steel surfaces). In this section values of 0.30, 0.50, 0.75 and 1.00 were used for μ_{c-c} , and values of 0.10, 0.30 and 0.50 were used for μ_{c-s} . The effect of the variation of μ_{c-c} and μ_{c-s} on the backbone curves is presented in Figs. 3.15(a) and 3.15(b), respectively. As shown in the figures, there is no effect of μ_{c-c} and μ_{c-s} on either displacement nor the ultimate displacement of the piers. This matches the experimental observations where there was no sliding of the steel jacket or segments.

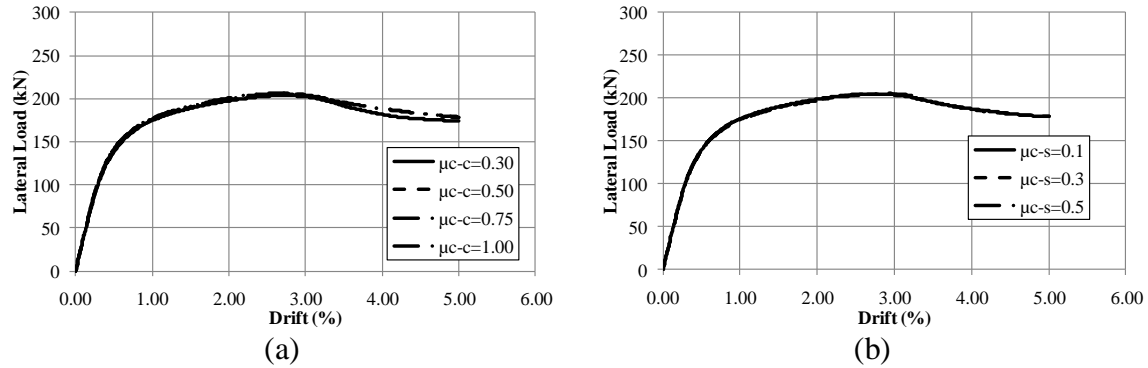


Figure 3.15: Effects of coefficients of friction on the backbone curves of pier JH11 (a) changing μ_{c-c} , and (b) changing μ_{c-s}

3.9 Findings and conclusions

This paper discusses the seismic behavior of the SPPT bridge piers. The piers consist of precast segments superimposed over each other and sandwiched between a reinforced concrete foundation and the bridge superstructure. The system is connected by unbonded post-tensioning tendons passing through ducts made in the segments during casting. The bottommost segments of the piers were encased in steel tubes to enhance its ductility. A FE model was developed, implemented and validated against experimental data. The analyses and experimental work presented in this study revealed that:

- The SPPT pier system is able to withstand large lateral drift angles with minimal damage and minimal residual displacements. The tested piers reached a lateral drift angle of approximately 4% with minimal damage in the form of spalling. After repairing this spalling and increasing the applied post-tensioning, the piers were able to reach a lateral drift greater than 5% before or at failure.
- Selection of the appropriate jacket height is a critical design parameter. For specimens JH1 and JH2, the height of jacket confinement was inadequate, leading to premature strength degradation of the test piers. A taller jacket would have postponed cover concrete spalling in the non-jacketed segments, thus reducing the amount of pier damage requiring repair.
- As expected, decreasing the piers' aspect ratios from 6 to 3 increased their initial stiffness and ultimate strength. In addition, increasing the applied post-tensioning force increased the ultimate strength of the test specimens.
- The FE model developed and presented in this paper was able to capture the backbone curves of the experimentally tested SPPT piers, and therefore could be used for

understanding the effects of the different parameters on the backbone curves of SPPT piers.

3.10 Acknowledgements

Funding for this research was provided by Transportation Northwest (TransNow) under Project No. 5200. Their assistance is greatly appreciated.

3.11 References

- ABAQUS Software and Documentation, Version 6.8-2. © Dassault Systèmes, SIMULIA, 2008.
- American Concrete Institute Committee 318, Building Code Requirements for Structural Concrete (ACI318-08) and Commentary (ACI318R-08). American Concrete Institute, Farmington Hills, MI.
- ASTM C469 (Standard test method for static modulus of elasticity and poisson's ratio of concrete in compression).
- Beque, J., Patnaik, A. K., and Rizkalla, S., (2003), "Analytical models for concrete confined with FRP tubes" J. Composites for Construction, ASCE, 7(1), 31-38.
- Chang, K. C., Loh, C. H., Chiu, H. S., Hwang, J. S., Cheng, C. B., and Wang, J. C. (2002). "Seismic behavior of precast segmental bridge columns and design methodology for applications in Taiwan", Taiwan Area National Expressway Engineering Bureau, Taipei, Taiwan in Chinese.
- Chou, C.-C., and Chen, Y.-C., (2006). "Cyclic tests of post-tensioned precast CFT segmental bridge columns with unbonded strands" J. Earthquake Engng. Struct. Dyn., 35, 159-175.
- Dawood, H. M., "Seismic Behavior of Segmental Precast Post-tensioned Concrete Piers", M.Sc. thesis, Washington State University, Washington, 2010
- ElGawady, M., Booker, A., Dawood, H. M. (2010). "Seismic behavior of post-tensioned concrete filled fiber tubes", ASCE, Journal of Composites for Construction, (to appear in October 2010 issue)
- ElGawady, M. A., Shaalan A., and Dawood, H. M. (2010). "Seismic behavior of precast post-tensioned segmented frames", 9th U.S. National and 10th Canadian Conference on Earthquake Engineering (July 25-29, 2010).

- ElGawady, M., and Shaalan, A., (2010- In review). “Seismic behavior of self-centering bridge bents”, ASCE, Journal of Bridge Engineering.
- Fam, A. Z., and Rizkalla, S. H., (2001), “Confinement model for axially loaded concrete confined by circular fiber-reinforced polymer tubes” ACI Str. J., 98 (4), 451-461.
- Hewes, J.T. “Seismic Design and Performance of Precast Concrete Segmental Bridge Columns.” Ph.D. Dissertation, University of California, San Diego, La Jolla, California. 2002.
- Lee, J., and G. L. Fenves, (1998) “Plastic-Damage Model for Cyclic Loading of Concrete Structures,” Journal of Engineering Mechanics, vol. 124, no.8, pp. 892–900.
- Lee, W. K., and Billington, S. L., (2009) “Modeling Residual Displacements of Concrete Bridge Columns under Earthquake Loads using Fiber Elements.”, ASCE J. Bridge Engineering, 15(3): 240-249.
- Lubliner, J., J. Oliver, S. Oller, and E. Oñate, (1989) “A Plastic-Damage Model for Concrete,” International Journal of Solids and Structures, vol. 25, pp. 299–329.
- Marriott., D., Pampanin, S., and Palermo, A., (2009). “Quasi-static and pseudo-dynamic testing of unbonded post-tensioned rocking bridge piers with external replaceable dissipaters” J. Earthquake Engng. Struct. Dyn., 38, 331-345.
- Ou, Y.-C., Chiewanichakorn, M., Aref, A. J., and Lee, G. C. (2007). “Seismic performance of segmental precast unbonded posttensioned concrete bridge columns.” J. Str. Eng., 133(11), 1636-1647.
- Mander, J. B., Priestley, M. J. N., and Park, R. (1988). “Theoretical stress-strain model for confined concrete.” J. Struct. Eng., 114(8), 1804–1826.
- Priestley N., Sritharan S., Conley J., and Pampanin S., (1999) “Preliminary results and conclusions from the PRESSS five-story precast concrete test building.” PCI Journal, 44 (6):p. 42-76.
- Samaan, M., Mirmiran, A., and Shahawy, M. (1998). “Model of concrete confined by fiber composite.” J. Struct. Eng., 124(9), 1025–1031.
- Teng, J. G., Jiang, T., Lam, L., and Luo, Y.Z., (2009), “Refinement of a design-oriented stress strain model for FRP-Confined concrete” J. Composites for Construction, ASCE, 13(4), 269-278.
- Wight, G. D. (2006) “Seismic Performance of a Post-tensioned Concrete Masonry Wall System.”, Ph.D. dissertation, University of Auckland, New Zealand.

CHAPTER FOUR

BEHAVIOR OF SEGMENTAL PRECAST POST-TENSIONED BRIDGE PIERS UNDER LATERAL LOAD: PARAMETRIC STUDY

Haitham Dawood⁴ Mohamed ElGawady^{5§} Joshua Hewes⁶

4.1 Abstract

This manuscript discusses the design parameters that potentially affect the lateral seismic response of segmental precast post-tensioned bridge piers. The piers consist of precast circular cross section segments stacked one on top of the other with concentric tendons passing through ducts made in the segments during casting. The bottommost segments of the piers were encased in steel tubes to enhance ductility and minimize damage. An FE model was used to investigate different design parameters and how they influence the lateral force – displacement response of the piers. Design parameters investigated include the initial post-tensioning stress as a percentage of the tendon yield stress, the applied axial stresses on concrete due to post-tensioning, pier aspect ratios, construction details, steel tube thicknesses, and internal mild steel rebar added as energy dissipaters. Based on the data presented, an initial tendon stress in the range of 40-60% of its yield stress and initial axial stress on concrete of approximately 20% of the concrete characteristic strength will be appropriate for most typical designs. These design values will prevent tendon yielding until lateral drift angle reaches approximately 4.5%. Changing the steel tube thickness, height, or a combination of both proved to be an effective parameter that may be used to reach a target performance level at a specific seismic zone.

⁴Graduate Research Assistant, Dept. of Civil and Environmental Engineering, Washington State University, Pullman, WA, hmousad@msn.com

⁵ Assistant Professor, Dept. of Civil and Environmental Engineering, Washington State University, Pullman, WA, melgawady@wsu.edu;

[§]Corresponding author

⁶ Assistant Professor, Dept. of Civil and Environmental Engineering, Northern Arizona University, Joshua.Hewes@NAU.edu

4.2 Keywords

ABAQUS, finite element model, post-tensioned, segmental pier, bridge

4.3 Introduction

This manuscript evaluates the effects of different design parameters on the backbone lateral force – displacement response of a segmental precast post-tensioned (SPPT) bridge pier. The standard pier investigated in this paper (see Fig. 4.1(a)) was similar in dimensions to pier JH11 tested by Hewes (2002) and described in detail by Dawood et al. (2010). The pier consisted of four concrete segments placed on top of each other and structurally connected using a concentric unbonded tendon comprised of 27 – 12.7 mm [0.5 in] diameter ASTM A779 Grade 270 (1860 MPa [270 ksi]) low-relaxation steel strands with a total cross-sectional area of 2665 mm²[4.13 in²]. The pier was circular in cross-section with diameter of 610mm [24 in]. The pier has an aspect ratio (AR) of 6, where aspect ratio is defined as the distance between point of application of lateral loading and pier base divided by pier diameter. The unbonded tendon length was $L_t = 4953$ mm [195 in]. The pier was investigated under an initial post tensioning stress corresponding to approximately 45% of the yield strength of the tendons.

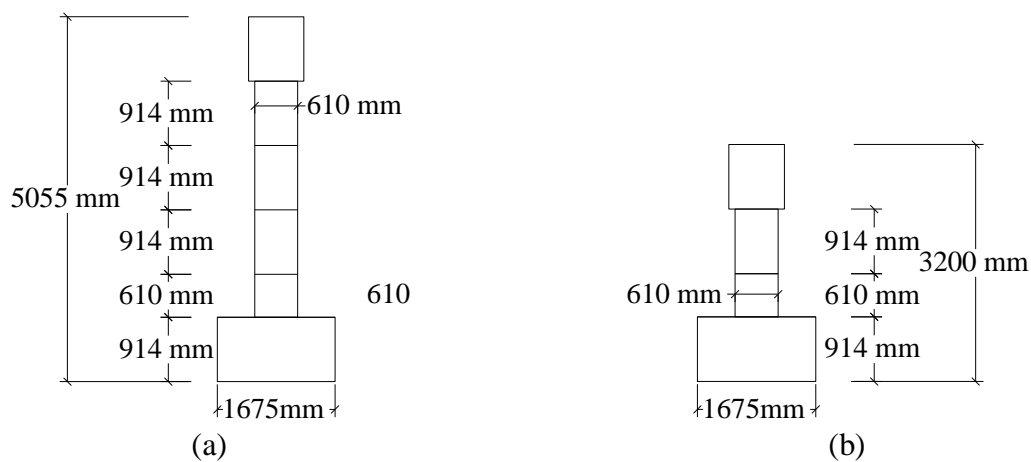


Figure 4.1: Detailed dimensions for (a) standard pier and (b) pier B

The bottommost segment of the pier utilized a 6.0 mm [0.24 in] thick, ASTM A569, A36 steel jacket to provide the relatively high level of lateral confinement which is required due to the high compressive strains associated with a pier rocking about its base. The steel jacket started from the top of the bottommost segment and terminated approximately 25.4 mm [1.0 in] above its bottom to prevent the jacket from bearing on the footing during testing. This resulted in a jacket height of approximately 585 mm [23 in]. The steel used in jacketing the segment had yield and ultimate strengths of 317 [46 ksi] and 460 Mpa [67 ksi], respectively. The jacketed segment did not contain any longitudinal reinforcement other than the post-tensioning tendons. The characteristic concrete compressive strength (f'_c) used was 41.4 MPa [6000 psi]. All other segments above the bottommost segment were modeled as conventional reinforced concrete segments having transverse spiral of #3 of Grade 60 spaced at 75 mm [3.0 in] for lateral confinement. The upper non-jacketed segments had a concrete cover of 25.4 mm [1.0 in].

Throughout this manuscript the standard pier was used for the analysis. However, to evaluate the effect of pier aspect ratio on pier response, a squat pier – namely “Pier B” – was also used in the investigation. The pier characteristics are identical to the standard pier in this manuscript but with an aspect ratio of 3. It consisted of only two segments resulting in a clear height of 1524 mm [60 in] instead of 3354 mm [132 in] for the standard pier.

A detailed finite element model for the pier was prepared, validated, and presented by Dawood et al. (2010). Fig. 4.2 shows a summary of the detailed finite element pier model. This model was used to study the effects of six parameters on the force-displacement response of SPPT piers. The effects of tendon initial post-tensioning stress level (PT), initial concrete compressive stress due to post-tensioning (IS), pier aspect ratio (AR), different construction details of the system (CON), confinement thickness at the pier’s base (CTh), and internal energy

dissipating bars (IED) on the overall behavior of the system were investigated. Table 4.1 summarizes the different values assigned for each parameter. The range of these parameters was selected to investigate a wide spectrum of values and does not necessarily reflect typical values to be used in practice.

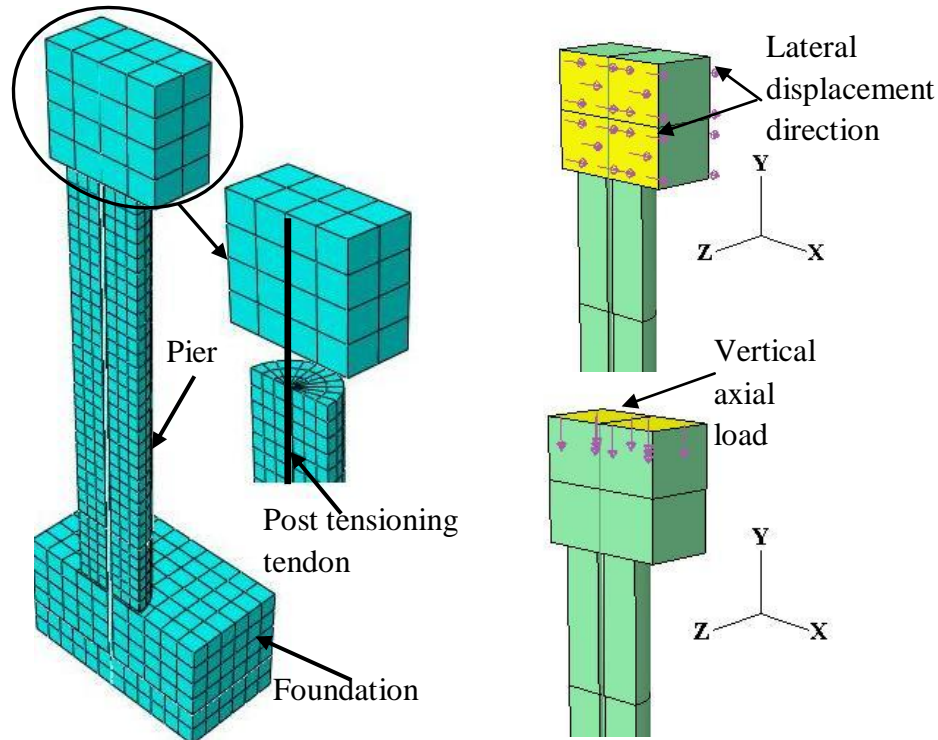


Figure 4.2: A typical mesh and applied loads and displacements for the SPPT pier.

Table 4.1: Different values assigned to each design parameter in the study

Series	Parameter	1	2	3	4	5	6	7	8
PT	Initial stress level as a percentage of tendon's yield stress (%).	30%	40%	45%	50%	60%	70%	80%	90%
IS	Stress on concrete induced by post-tensioning as a percentage of f'_c (%)	13%	16%	19%	22%	25%	28%	31%	-
AR	Aspect ratio of the piers.	3.0	4.5	6.0	7.5	9.0	-	-	-
CON	Different configurations of the system	See Fig. 4.14					-	-	-
CTh	Confinement thickness (mm)	6.0	4.5	3.0	1.5	-	-	-	-
IED	Reinforcement ratio of the mild steel used as internal energy dissipaters (%).	0.00	0.25	0.44	1.34	1.75	-	-	-

4.4 Results and Discussions

4.4.1 Effects of initial post-tensioning level in the tendon

The first parameter investigated in this study – the PT series – was the level of initial tendon stress. The initial post-tensioning stress ranged from 30% to 90% of the yield strength of the tendons while changing the cross sectional area from 4000 mm² [6.2 in²] to 1300 mm² [2.0 in²], respectively, to maintain the axial stresses on the concrete invariant at 7.17 MPa [1040 psi] which corresponds to 17% of f'_c . Fig. 4.3 shows the lateral drift at the loading point (middle of the loading stub) versus the measured the lateral resistance of the different piers. The lateral drift was defined as the ratio of the measured lateral displacement divided by the height of the loading point above the pier base. As shown in the figure, all the piers reached their ultimate strengths at a lateral drift angle of approximately 3%. Beyond that, a gradual degradation in the strength occurred and the analysis ended at a lateral drift angle of 5%. At this drift level, a reduction of approximately 14% occurred in the strengths of the piers. The analysis truncated due to spalling and compression failure at the bottom of the second segment.

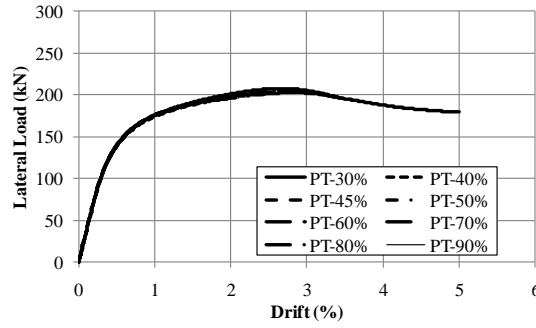


Figure 4.3: The effects of changing the initial post-tensioning stress in the tendons while keeping the same stress on concrete

Fig. 4.3 shows that changing the initial post tensioning stress in the tendon while maintaining constant initial axial stress on the concrete segments does not have a major effect on the backbone curve of the system. Surprisingly, in no case yielding of the tendon was observed. Since the post-tensioning tendon was placed in the geometric centroid of the pier, the increase in the tendon stress due to interface joints opening initiated after significant drift of the pier took place. Fig. 4.4 shows the lateral drift vs. the peak stress in the tendon for each pier. As shown in the figure, the increase in the tendon stress started at a lateral drift angle of approximately 1% and beyond that the increases in the post-tensioning stresses were quite small. The post-tensioning stresses reached their peak at a lateral drift of 3% when the piers reached their peak strength. Beyond that both the strengths of the piers and the stresses in the tendons started to decrease due to damage at the bottom of the second segments.

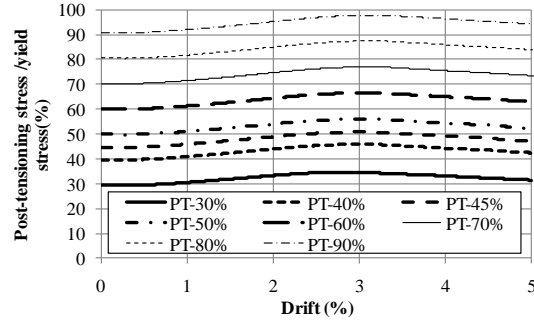


Figure 4.4: Drifts of different pier vs. the stresses in the post-tensioning tendons normalized by its yield stress

A second reason for the elastic response of the tendon was the relatively long unbonded length of the tendon. In the case of a squat pier, the unbonded tendon length will be relatively small and thus larger incremental tendon strains will occur with increasing the applied lateral displacement, resulting in potential yielding of the tendon if it was initially stressed to high initial stress levels. Fig. 4.5 shows the effects of the level of the initial post-tensioning stresses on the response of Pier B. Only three levels of initial post-tensioning stresses were investigated namely, 40%, 60%, and 80% of the yield stress of the tendon. Fig. 4.6 shows the peak stresses in the tendon versus the lateral drift angles of Pier B.

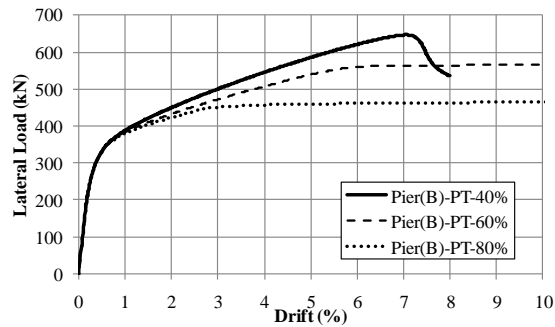


Figure 4.5: The effects of changing the initial post-tensioning stress in the tendons for squat piers

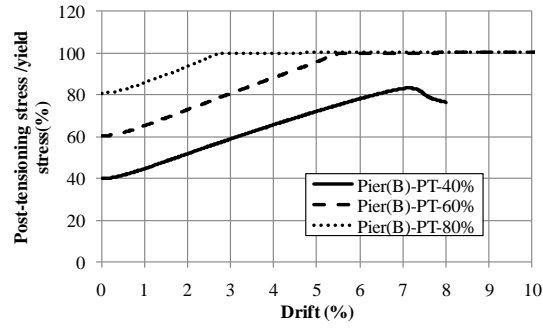


Figure 4.6: Drift of squat piers vs. the stresses in the post-tensioning tendons normalized by their yield stress

As shown in Figs. 4.5 and 4.6, increasing the initial post-tensioning stresses to 60% and 80% of the tendon yield stresses resulted in yielding of the tendon at lateral drift angles of 5.5%, and 2.5%, respectively. In addition, Fig. 4.6 shows that the increase in the tendon stresses started at small lateral drifts of approximately 0.2% which is significantly smaller than in the case of the more slender standard pier. Moreover, the rate of the strain increase in the post-tensioning is higher in the case of the squat piers compared to the slender piers. For small initial stresses of 40% of the yield stress, no yielding of the tendon was observed and the tendon reached a peak stress of approximately 82% of its yield stress followed by concrete crushing and the analysis stopped. Such crushing at high drift angle of 7% led to brittle failure as indicated in Fig. 4.5.

For initial tendon stresses of 40% of the yield stress (Fig. 4.5), the pier was able to develop a peak strength of 650 kN [146 kips] at a lateral drift angle of 7% where the concrete started to crush rupture and the analysis stopped at a lateral drift angle of 8%. For high initial stress in the tendons, the piers reached lateral strengths of 580 kN [130 kips] and 480 kN [108 kips] at lateral drift angles of 2.5% and 5.5% for initial post-tensioning stresses of 60 and 80% of the yield stress. Once the tendon yielded, the pier reached its peak strength and a substantial decrease in the tangent stiffness of the system occurred. Based on these analyses and within the

scope of this study it appears that an initial post-tensioning stress in the tendon that range from 40 to 60% of the tendon yield stress is suitable for design. A squat pier ($AR=3$) with an initial post-tensioning stress of 60% of the tendon yield stress would reach yielding of the tendon at a lateral drift of 5.5%; however, such drift angle is beyond the anticipated level of drift angle for a typical bridge. Priestley et al. (2007) recommended a drift angle of 4.5% for a bridge at the collapse prevention limit state.

4.4.2 Effects of initial stresses on the concrete

The second parameter investigated in this study – the IS series – was the level of the initial axial compressive stress imposed on the concrete due to post-tensioning forces. This was achieved by maintaining the tendon's post-tensioning stress constant at 45% of its yield stress while changing the tendon cross-sectional area from 1980 mm^2 to 4990 mm^2 [3.07 in^2 to 7.73 in^2]. This resulted in axial stresses in the concrete ranging from 5.38 MPa [780 psi] to 12.83 MPa [1860 psi] which corresponds to 13% to 31% of f'_c .

Fig. 4.7 shows the lateral drift angle versus the lateral resistance of the piers with different initial stresses on the concrete. Increasing the applied axial stresses on the piers increased the yield strengths, the ultimate strengths, and the post-elastic stiffness of the piers. However, the increase in the applied initial post-tensioning stress on the concrete resulted in a reduction in the ultimate drift angles and the drift angle at the maximum lateral load. For small axial stresses on the concrete segments, the geometric nonlinearity, i.e. the rocking mechanism was predominant, while for the case of high axial stresses the material nonlinearity was dominant leading to concrete crushing at smaller drift angles. This resulted in two features in the backbone curves (Fig. 4.7): 1) the transition between the initial and post-elastic stiffness is abrupt for small axial stresses compared to high initial stresses; and 2) the slope of the lateral resistance –drift

curves beyond the peak strength is relatively sharper for higher concrete initial axial stress resulting in small ultimate drift angles. This is attributed to the high stresses accumulated by the rigid body rocking that result in more brittle failure.

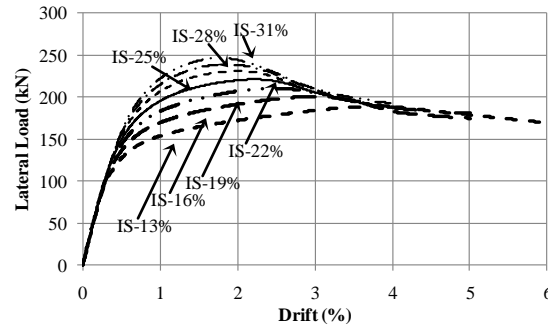


Figure 4.7: The effects of increasing the axial stresses due to post-tensioning forces on concrete segments

Fig. 4.8 shows the peak stress in the post-tensioning tendon normalized by its yield stress vs. the lateral drift of the standard piers. As shown in the figure, in no case did tendon yielding occur. In addition, the rate of increase in the post-tensioning stress was slightly higher for piers having smaller axial stress on the concrete since piers that were subjected to small axial stress due to post-tensioning were able to reach deformation higher than other piers subjected to higher post-tensioning forces (Fig. 4.7). Decreasing the applied axial stress due to post-tensioning made the rocking response and geometric nonlinearity more dominant compared to the deformation in the case of high applied axial stress due to post-tensioning.

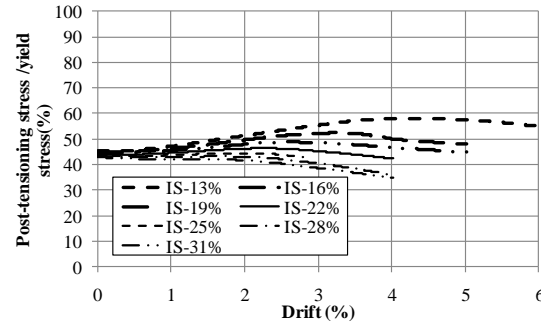


Figure 4.8: The increase in the post-tensioning stresses vs. the standard piers lateral drifts

Based on these analyses, it seems an initial concrete axial stress of approximately $20\%f_c$ is reasonable for design of piers similar to those examined in this manuscript. The slender piers that were subjected to axial concrete stresses of approximately 20% of f_c or less were able to reach an ultimate drift angle of 4.5% or larger.

To investigate this recommendation for a squat pier, Pier B was analyzed under different axial concrete stresses ranging from 19 to $31\% f_c$. Fig. 4.9 shows the effects of the applied axial stresses on the concrete on the backbone curves of Piers B. As shown in the figure and similar to the case of the standard pier, increasing the applied axial stress due to post-tensioning slightly increased the strength of the piers; however, it significantly increased the post-elastic stiffness and decreased the ultimate drift angle. Piers that were subjected to an axial stress of approximately 22% of f_c or less were able to reach an ultimate drift angle of 5% or greater.

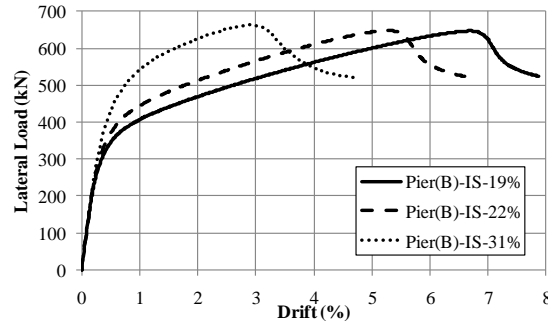


Figure 4.9: The effects of increasing the axial stresses on concrete segments for Pier B

Fig. 4.10 shows the variation of peak stresses in the tendons versus the lateral drift for Pier B for the different applied axial stresses on the concrete segments. As shown in the figure, in no case did yielding of the tendon occur.

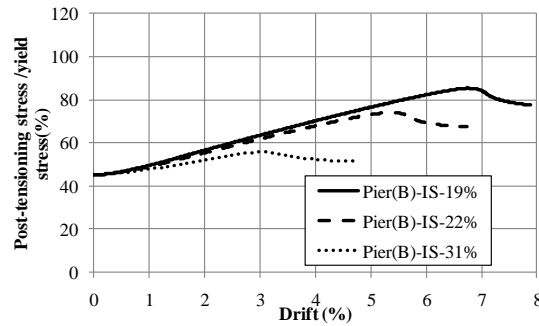


Figure 4.10: The increase in the post-tensioning stresses vs. piers type B lateral drifts

4.4.3 Effects of pier aspect ratio

The third parameter investigated in this manuscript was the effects of increasing the aspect ratio – AR series – of the piers from 3 to 9 by adding one more segment from one pier to the other as shown in Fig. 4.11.

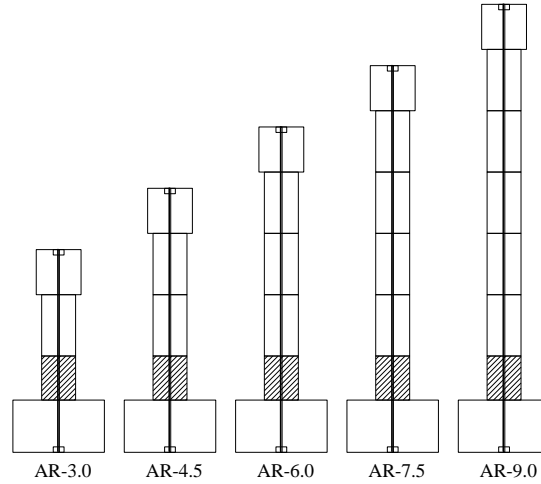


Figure 4.11: Layout of the piers having different aspect ratios

Fig. 4.12 shows the lateral resistance of the different piers versus the lateral drift angle measured at the loading point. Increasing the aspect ratio of the piers from 3 to 9 decreased the initial stiffness as well as the ultimate drift angle (Fig. 4.12(a)) and increased to lesser extent the ultimate displacement (Fig. 4.12(b)). Failure of squat piers was more abrupt compared to slender piers since in the squat piers more stress concentration and damage occurred at the bottom of the second segment compared to slender piers. The slope of the post-elastic stiffness increased with decreasing the pier aspect ratio.

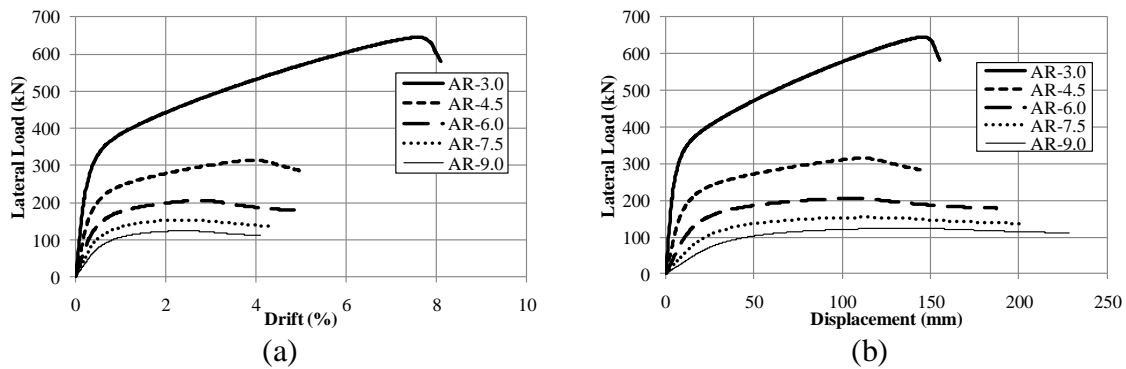


Figure 4.12: The effect of changing the piers' aspect ratio on the backbone curves

Fig. 4.13 shows an approximate mechanism for the rotation of two piers having two different aspect ratios, assuming rigid rotations of the segments over each other and also assuming that only the interface joint between the bottommost segment and foundation will open. For both piers to reach the same displacement, the ratio of the rotation of the squat piers (θ_{squat}) to the rotation of the slender piers (θ_{slender}) i.e. ($\theta_{\text{squat}} / \theta_{\text{slender}}$) should be approximately equal to H/h where h , H , θ_{squat} and θ_{slender} are shown on Fig. 4.13. Because the rotation in the squat pier is higher, the elongation of the tendon in the squat pier is higher. Additionally, for the squat pier the unbonded tendon length is shorter than in the case of the slender pier, resulting in higher incremental strains and higher incremental post-tensioning stresses. Such increases led to an increase in the slope of the post-elastic stiffness. It is worth noting that in no case did the tendon reach its yield strain and in all cases the analysis stopped due to concrete crushing at the bottom of the second segment.

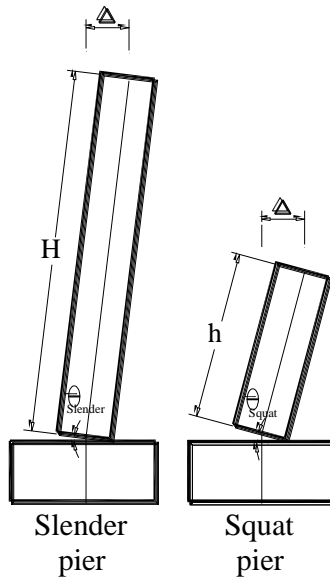


Figure 4.13: The mechanism of deformation for slender and squat piers

4.4.4 Effects of construction details

The fourth parameter investigated –CON series –was the effect of different construction details on the behavior of the pier system. As shown in Fig. 4.14, case CON-1 was a pier constructed similar to the standard pier. Pier CON-2 represents a different construction scenario where the bottommost two segments in the pier CON-1 were replaced by a single segment cast monolithically while maintaining the steel confinement height and thickness unchanged from those used for pier CON-1. In the case of pier CON-3, the three lowest segments were cast monolithically while maintaining the same steel confinement configuration. Pier CON-4 had construction details similar to pier CON-1 except that the two lower segments of pier CON-4 were both confined by steel tubes having a thickness of 6 mm [0.24 in]. In Fig. 4.14, the hatched areas represent segments confined by external steel tubes.

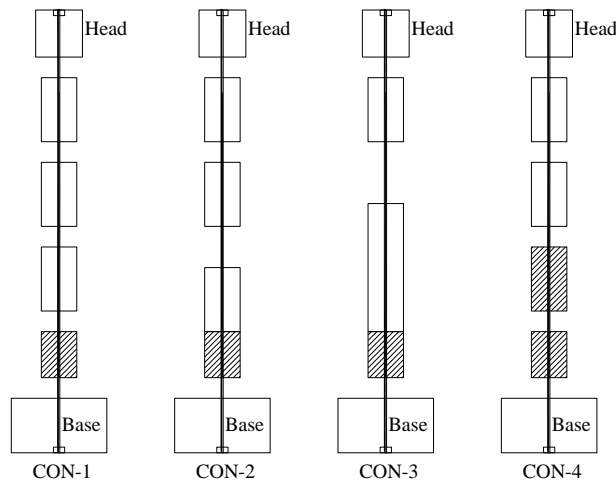


Figure 4.14: Configuration of each pier of CON series

Fig. 4.15 represents the backbone curves for the different piers of series CON. As shown in the figure, the ultimate displacement of the pier CON-2 is approximately 140% of that of the pier CON-1. In the case of pier CON-1, the pier failed due to stress concentration at the interface between the lowest two segments resulting in spalling and crushing of the concrete at the second

segment. The concrete of the second segment was less ductile than that of the bottommost segment due to the confining steel tube. Pier CON-2 has the advantage of the continuation of stresses between the first two segments (no interface joint opening), and consequently concentrated the stresses at the interface joint between the foundation and the bottommost segment. The high confinement of the lower segment prevented the premature failure of the pier due to high stress concentrations that happened in the case of pier CON-1.

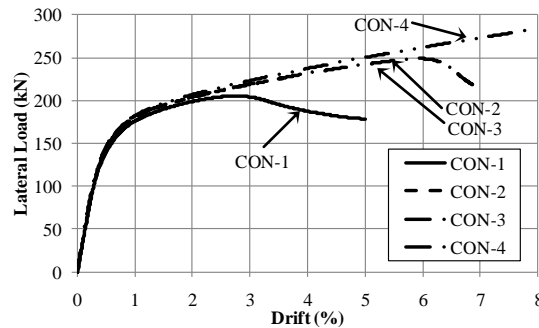


Figure 4.15: The effects of the different configurations on the backbone curves

Removing the interface joint between the second and the third segments in the case of pier CON-3 had minor effects on the ultimate drift angle. Since the joint opening at this interface in pier CON-2 was minimal, removal of the joint for CON-3 had little influence on response.

Another option to prevent premature failure due to stress concentration at the interface joint between the first and second segment was to encase the second segment in a steel tube as shown for pier CON-4 in Fig. 4.14. As expected, in the case of pier CON-4, the ultimate drift angle increased to approximately 160% and 115% of the ultimate drift angles of the piers CON-1 and CON-2, respectively. This indicated the importance of designing the confinement of each segment to obtain the optimum performance of the pier from structural and economical point of views. This analysis showed an important conclusion that a design engineer can achieve a target

displacement performance point using either an appropriate segment height, appropriate confinement configuration, or a combination of the two.

4.4.5 Effects of confinement thickness

The fifth parameter investigated in this study – series CTh – was the effect of changing the confinement ratio of the bottommost segment on the backbone behavior of the system. The volumetric reinforcement ratios chosen ranged from 3.9% to 1% which corresponds to a steel tube thickness of 6.0 mm [0.24 in] to 1.5mm [0.06 in]. These thicknesses were used for confinement in two different scenarios: the first scenario (Fig. 4.16(a)) where only the bottommost segment was confined; the second scenario where the two bottommost segments (Fig. 4.16(b)) were confined. As shown in the figure, the confinement volumetric reinforcement ratio had minimal effect in the case of confining only the lower segment since failure occurred mainly at the second segment due to concrete cover spalling. On the other hand, increasing the confinement thickness of the two bottommost segments enhanced the ductility and increased the ultimate displacement by approximately 100% when the confinement thickness increased from 1.5mm [0.06 in] to 6.0mm [0.24 in]. Increasing the confinement thickness had no effect on the yield lateral strength but increased the post yield stiffness. This shows that the confinement volumetric reinforcement ratio and height are very important parameters to fulfill the required performance level in a given seismic zone.

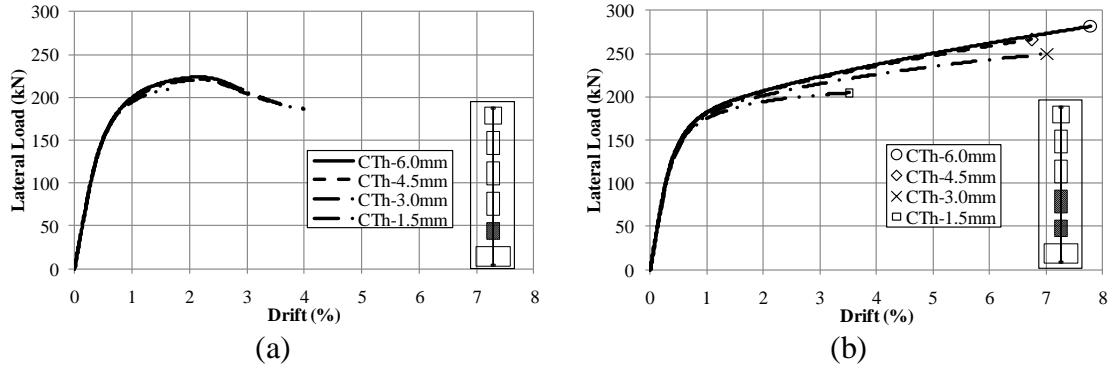


Figure 4.16: The effects on the backbone curves of the different confinement thicknesses for; a) the lower segment only, and b) the lower two segments

4.4.6 Effects of adding internal energy dissipaters

The last parameter investigated in this study was the effect of adding ten mild steel rebar as internal energy dissipaters (IED) to the interface joint between the base and the bottommost segment as well as at the interface between the bottommost segment and the second segment. During earthquake ground motion such mild steel bars would yield increasing the energy dissipation of the system. The rebar had nominal diameter ranging from 0 (i.e. no IED) to 25 mm [#8] with all the rebar extended 305mm [12 in] on each side of the interface joints. The rebar length was selected to represent one-half the height of the bottommost segment. Fig. 4.17 shows the backbone curves for the different piers having the internal rebar.

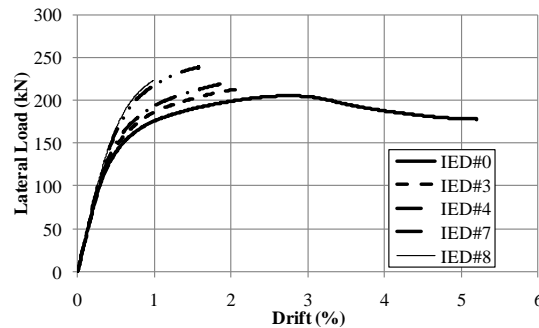


Figure 4.17: The effects of the IED on the backbone curves

As shown in the figure, adding internal mild steel rebar, as energy dissipaters, increased the ultimate strength. However, failure of the piers having such rebar was quite brittle with limited drift angle capacity. Adding the rebar changed the mode of failure from compression controlled, for pier IED#0- without internal rebar, to anchorage failure in the rebar due to the limited development length (Fig. 4.18).

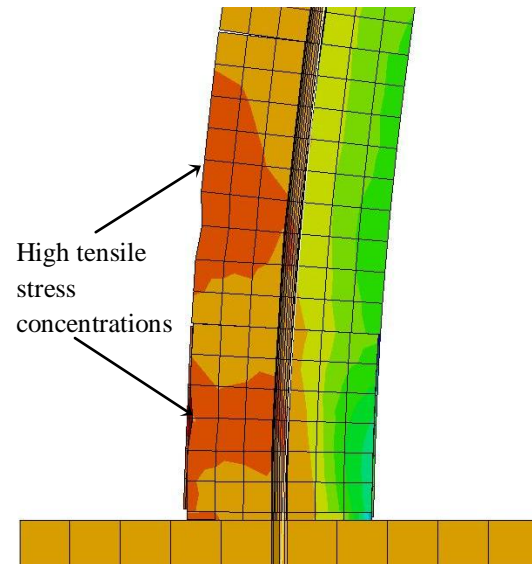


Figure 4.18: High stress concentrations in the segments due to the insufficient development length of the IED bar

In general, increasing the rebar size decreased the ultimate drift angle but increased the ultimate strength of the piers. Fig. 4.19 shows the relationship between pier lateral drift angle versus the normalized tensile stress in the rebar located at the extreme tension side of the pier. The normalized tensile stress is defined as the stress in the rebar normalized by its yield stress. The figure shows that in the case of small rebar diameters, i.e. #3 and #4, the mild bars reached their yield strength before the failure of the pier occurs. However, the rebar were not able to develop their over-strength stresses. For large rebar diameters i.e. #7 and #8 the mild rebar didn't reach their yield stress. However, there was softening in the behavior of the rebar. This softening

is attributed to anchorage failure of the rebar. Yielding of the rebar potentially will lead to higher energy dissipation, high residual displacement, and more concrete damage. However, the rebar should be well designed to avoid brittle anchorage failure.

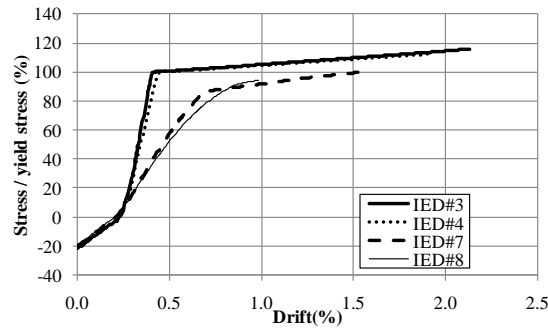


Figure 4.19: The effects of different IED rebar diameters on normalized stresses on the rebar

4.5 Findings and Conclusions

This paper discusses the seismic behavior of the SPPT bridge pier system. The piers consist of precast segments stacked on each other and sandwiched between a reinforced concrete foundation and the bridge superstructure. The system is connected by unbonded post-tensioning tendons passing through ducts made in the segments during casting. The bottommost segments of the piers were encased in steel tubes to enhance its ductility. A FE model was used to investigate different design parameters and how they affect the backbone curves of a given pier. Different parameters including: initial post-tensioning stresses as a percentage of the tendon yield stress, the applied axial stresses on concrete due to post-tensioning, the piers aspect ratios, construction details, confinement thicknesses, and adding internal mild steel rebar as energy dissipaters are discussed in this manuscript. The analyses revealed that:

- Increasing the post-tensioning stresses in the tendon by decreasing its cross sectional area while keeping the same axial stress on the concrete will not have significant effects on relatively slender piers. In this case tendons will not likely yield. On the other hand,

increasing the initial post-tensioning stresses in the tendons of squat piers will potentially lead to yielding of the tendon during a major earthquake excitation which will decrease both the pier's tangent stiffness and the ultimate strength. Based on the data analyzed in this manuscript, it seems that an initial tendon stress of 45% of its yield stress will be appropriate for design purposes. Using this initial post-tensioning stress will not lead to yielding of the tendon until a lateral drift angle of approximately 4.5%.

- Increasing the initial axial stresses on concrete segments by increasing the post-tensioning forces significantly increased the yield and ultimate strengths, but reduced the ultimate drift angles. Based on the data analyzed in this manuscript, an initial axial stress on the concrete of approximately 20% of f'_c seems appropriate for design purposes.
- Increasing the aspect ratio of the piers led to a decrease of the initial stiffness and post-elastic stiffness as well as the yield lateral load. On the other hand, increasing the aspect ratio led to a less brittle descending branch of the backbone curves.
- Encasing the concrete segments in steel tubes significantly increased the ductility of the SPPT piers. However, the confinement volumetric ratio and height are critical parameters that can be tailored to fit different seismic demands.
- Adding internal energy dissipaters to the piers led to an increase in the ultimate strength and post elastic stiffness. Using small reinforcement ratios resulted in yielding of the rebar potentially leading to high energy dissipation and residual displacement. On the other hand, using high reinforcement ratios resulted in elastic response of the rebar potentially leading to small energy dissipation and residual displacements. However, adequate development length should be provided to avoid concrete brittle failure.

4.6 Acknowledgements

Funding for this research was provided by Transportation Northwest (TransNow) under Project No. 5200. Their assistance is greatly appreciated.

4.7 References

- ABAQUS Software and Documentation, Version 6.8-2. © Dassault Systèmes, SIMULIA, 2008.
- ASTM A569/A569M-98, (Standard Specification for Steel, Carbon (0.15 Maximum, Percent), Hot-Rolled Sheet and Strip Commercial)
- ASTM A779 / A779M – 05, (Standard Specification for Steel Strand, Seven-Wire, Uncoated, Compacted, Stress-Relieved for Prestressed Concrete)
- Chou, C.-C., and Chen, Y.-C., (2006). “Cyclic tests of post-tensioned precast CFT segmental bridge columns with unbonded strands” J. Earthquake Engng. Struct. Dyn., 35, 159-175.
- Dawood, H. M., “Seismic Behavior and Design of Segmental Precast Post-tensioned Concrete Piers”, M.Sc. thesis, Washington State University, Washington, 2010
- Dawood, H., ElGawady, M., and Hewes, J., “Behavior of Segmental Precast Post-Tensioned Bridge Piers Under Lateral Loads: Experimental and Modeling”, Journal of Bridge Engineering, 2010 (in review).
- ElGawady, M., Booker, A., Dawood, H. M. (2010- In press). “Seismic behavior of post-tensioned concrete filled fiber tubes”, ASCE, Journal of Composites for Construction.
- Hewes, J.T. “Seismic Design and Performance of Precast Concrete Segmental Bridge Columns.” Ph.D. Dissertation, University of California, San Diego, La Jolla, California. 2002.
- Priestley, M.J.N., Calvi, G. M., and Kowalsky, M. J., “Displacement Based Seismic Design of Structures,” IUSS Press, Pavia, Italy, 2007, 720pp.

CHAPTER FIVE

FINITE ELEMENT MODEL CALIBRATION AGAINST SPPT SYSTEM DEVELOPED IN WASHINGTON STATE UNIVERSITY AND PARAMETRIC STUDY

5.1 Introduction

The aim of this chapter is to calibrate the finite element model described in chapter (3) against the experimental study conducted on a segmental precast post-tensioned (SPPT) pier system developed at WSU. The chapter contains a brief description of the experimental studies conducted by Booker (2008) and ShaAlan (2009) at WSU. The implementation of the FE model to fit the different parameters used in these studies is described and followed by a comparison between the output of the FE model and the two experimental studies. Finally, a parametric study is presented.

5.2 Piers Tested by Booker (2008)

Two SPPT concrete piers tested by Booker (2008) were used in the FE model's calibration. These piers were tested under cyclic loading induced by an actuator attached to a steel loading frame (Fig. 5.1). The two piers have the characteristics presented in Table 5.1 and shown in Fig. 5.2.

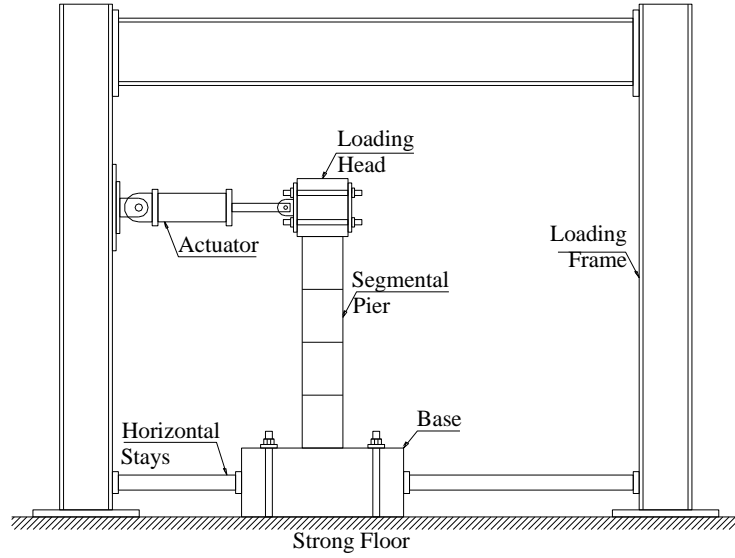


Figure 5.1 Schematic drawing showing the setup for the cyclic loading test for the piers

Table 5.1 Description of the piers used in the laboratory testing

Name	Height to Load	Horizontal Reinforcement	No. of segments	Segment Height
FRP1	1651 mm [65 in]	FRP Tube	1	1524 mm [60 in]
FRP4	1651 mm [65 in]	FRP Tube	4	381 mm [15 in]

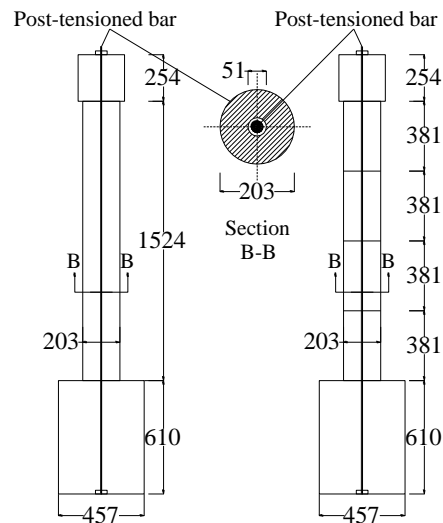


Figure 5.2 Schematic drawing for the two piers used for the calibration of the FE model (Dimensions in mm)

5.3 Bents Tested by Shaalan (2009)

Two SPPT concrete bents tested by Shaalan (2009) were used in the FE model's calibration. The schematic drawings showing the setup for the cyclic loading test and the bents configuration are shown in Figs. 5.3 and 5.4, respectively. Table 5.3 shows the description of the tested frames.

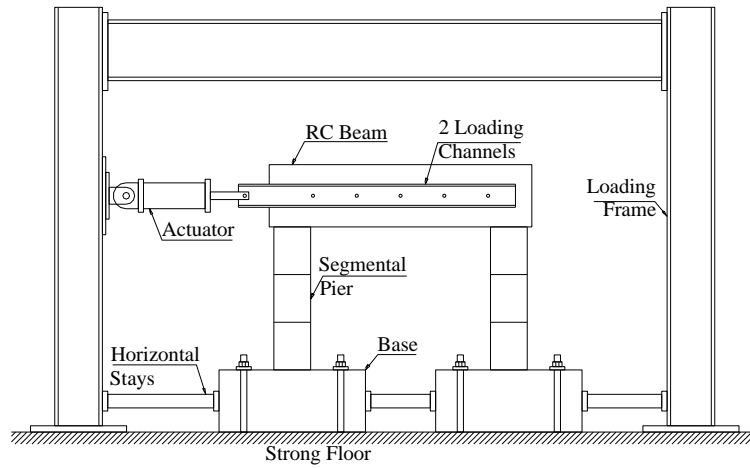


Figure 5.3 Schematic drawing showing the setup for the cyclic loading test for the bents

Table 5.2 Description of the bents used in the laboratory testing

Name	Height to Load	Horizontal Reinforcement	No. of segments	Segment Height
F-FRP1	1334 mm [52.5 in]	FRP Tube	1	1143 mm [45 in]
F-FRP3	1334 mm [52.5 in]	FRP Tube	3	381 mm [15 in]

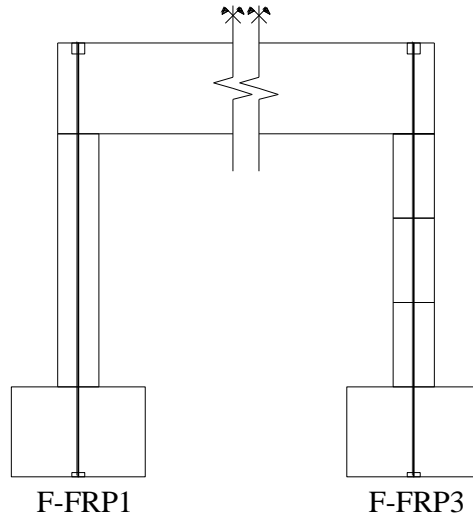


Figure 5.4 Schematic drawing for the tested frames

5.4 Finite Element Model Implementation

The specimens studied by Booker (2008) and Shaalan (2009) were constructed by sandwiching segments between the foundation and superstructure of the pier (represented by a loading stub for the piers and by a reinforced concrete beam for the bents) by an unbonded post-tensioned bar. The segments were plain concrete directly poured in glass fiber reinforced polymer (GFRP) tubes to confine the concrete's core and work as permanent formwork for the segments. In the case of the bents, a reinforced concrete beam was post-tensioned to the top of both piers to make the two piers behave as one bent (Fig. 5.5).

The passive confining stresses imposed by the GFRP tubes on the concrete core during loading alter its stress-strain behavior by increasing both its peak strength and ductility. Through this study, Samaan et al.'s (1998) model was used for developing the stress-strain behavior of the pier's core. On the other hand, the model developed by Mander et al. (1988) was used to develop the stress strain curve of the reinforced concrete beam.

The characteristic compressive strengths (f'_c) of the concrete used for casting the segments and the reinforced concrete beam were 13.8 MPa [2000 psi] and 22.08 MPa [3200 psi], respectively. Concrete was defined using a density of 2214 kg/m³ [138 lb/ft³] and a Poisson's ratio of 0.2. The stress strain curves in compression for the concrete segments and the reinforced concrete beam is shown in Fig. 5.6.

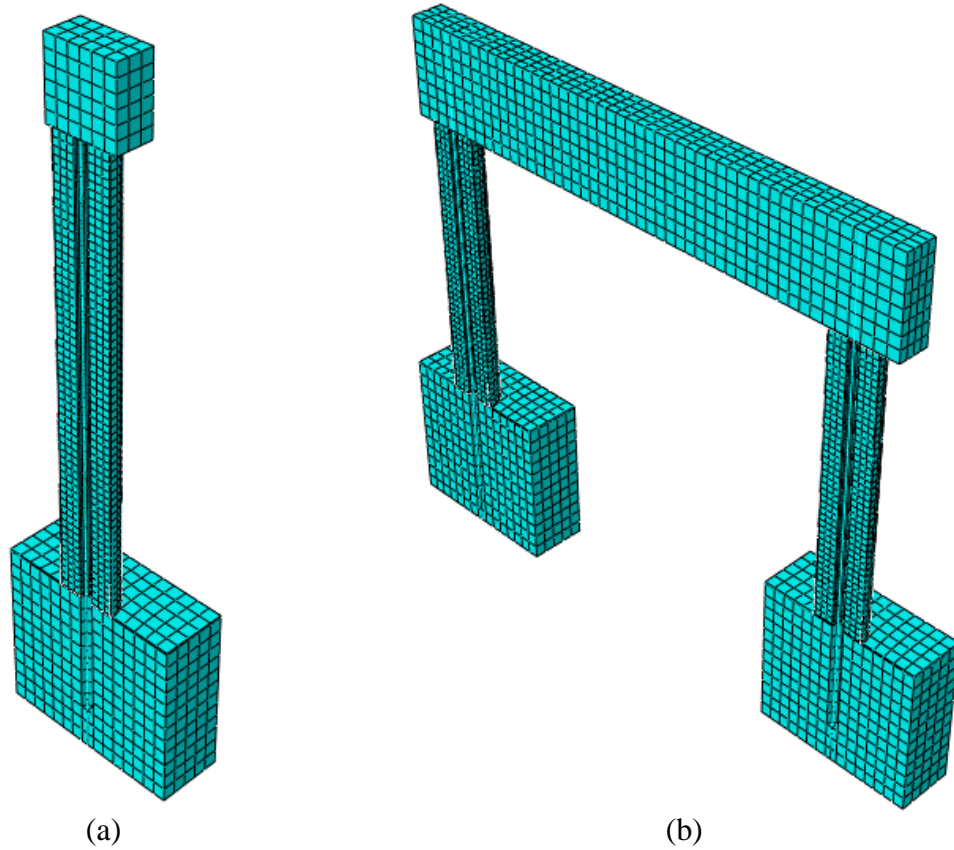


Figure 5.5: Typical mesh used for the FE model of: a) piers, and b) bents.

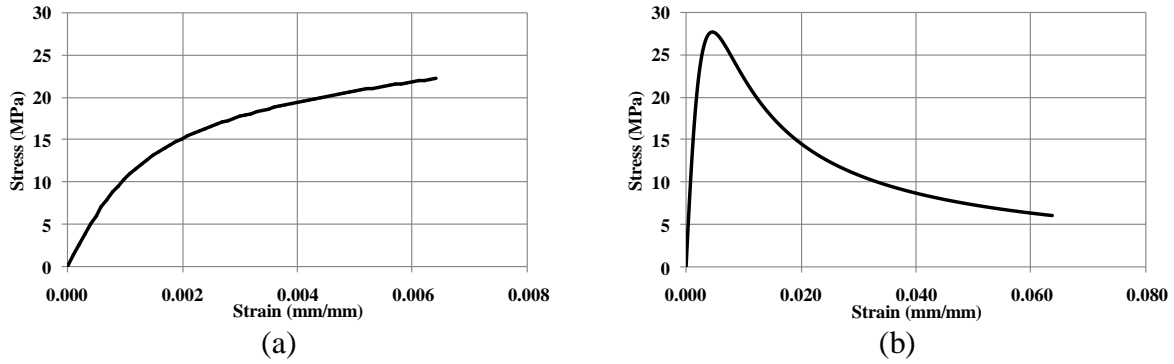


Figure 5.6: Stress strain curves for the concrete of: a) segments of the piers and bents, and b) beam of the bent

The tendons used in these two studies were DYWIDAG hot-rolled post-tensioning bars 31.75 mm [1.25 in] in diameter. The tendon's material was modeled using a density of 7840 kg/m³ [0.28 lb/in³], Poisson's ratio of 0.3, modulus of elasticity of 204,774 MPa [29,700 ksi], yield stress of 874 MPa [126,800 psi] and ultimate stress of 1,110 MPa [160,900 psi].

Amalga Composites clear fiberglass tubing was selected with a diameter of 203 mm [8 in] and wall thickness of 3.18 mm [0.125 in] as a confining material. The tubes were delivered in ten foot lengths which were cut to size. The GFRP material was used with an elastic modulus of 13,848 MPa [2,000 ksi] and a Poisson's ratio of 0.35 (Appendix A).

5.5 Results and Discussions

5.5.1 Piers

The FE model was able to capture the overall behavior of the piers. Figs. 5.7 and 5.8 show the backbone curves from the experimental work superimposed with the model's output. It is worth mentioning that the abrupt reduction in the tangent stiffness of the system was measured in the FE model when the neutral axis at the lowermost section of the pier reaches the tendon's level, this behavior was also reported by Hewes and Priestley (2002).

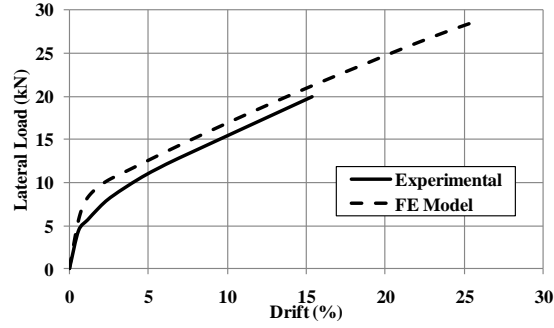


Figure 5.7: Experimental versus predicted backbone curves for the singly segmented pier

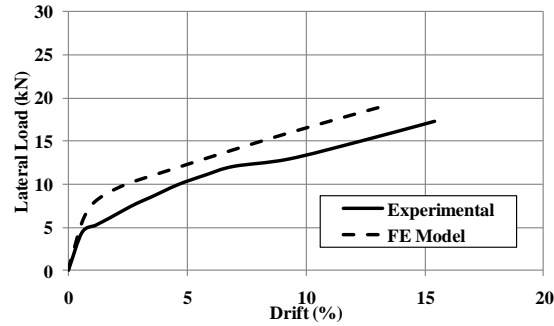


Figure 5.8: Experimental versus predicted backbone curves for the multi segmented pier

Figs. 5.7 and 5.8 show that the FE model was able to capture the initial stiffness of the piers. On the other hand, the FE model over estimated the lateral load at which the stiffness is reduced. An indepth study was performed to understand which factors affects this load, the major factor was found to be the post-tensioning load. The foundation surface was not well leveled during the casting, to overcome this problem a grout layer was used to assure a well leveled surface. This grout layer showed severe damage while testing the piers in the lab. The grout behavior can be explained as follows. At the beginning of the lateral loading, the grout behaved without suffering any damage so it did not affect the system's behavior. At high lateral drift angles the damage propagated, resulting in a softer behavior. The softened grout layer affected

the behavior by reducing the post-tensioning stress in the tendon and by behaving as a soft pillow under the pier. This behavior is proposed as an explanation for the deviation between the FE model and the experimental results.

5.5.2 Bents

In the case of the bents, a cement paste layer approximately 6mm [0.25 in] thick was used to level the foundation surface. This layer was simulated in the model by an elastic material that has an elastic modulus of 4.83 Mpa [700 psi] (Darwish and Al-Samhan).

Figs. 5.9 and 5.10 show the backbone curves from the experimental work conducted on the SPPT concrete bents superimposed with the model's output. The curves shows that the FE model was able to capture quite well the backbone behavior of the system.

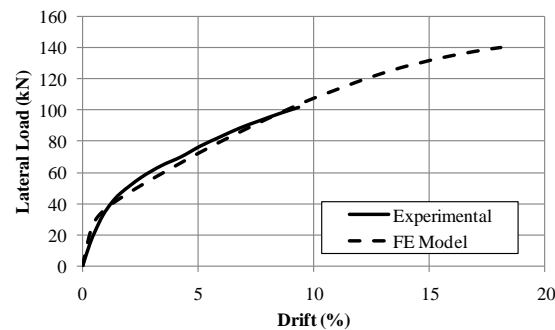


Figure 5.9: Experimental versus predicted backbone curves for the singly segmented bents

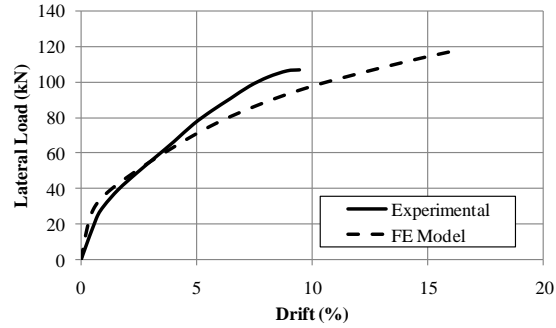


Figure 5.10: Experimental versus predicted backbone curves for the multi segmented bents

5.6 Parametric Study

The model described above was used to study the effects of different design parameters on the backbone curves of the previously described SPPT piers. The piers in this parametric study have $f'_c = 41.4$ MPa [6000 psi] and a FRP confining tube thickness = 19 mm [0.75 in]. The FRP characteristics were similar to those used in FRP1 and FRP4. Two series of piers were investigated in this parametric study: series “L” are piers having large diameter of 1220 mm [48 in] while series “S” are piers having a diameter of 610 mm [24 in]. The post-tensioning tendons had yield diameters of 176 mm [6.92 in] and 93 mm [3.68 in] for “S” and “L” series, respectively. The piers had heights ranging from 1830 mm [72 in] to 9145 mm [360 in]. All the piers were subjected to external gravity load corresponding to an axial stresses normalized by f'_c (DL) of 7%, unless otherwise mentioned. The piers were subjected to variable post-tensioning forces corresponding to axial stresses, normalized by f'_c , (PT) ranging from 10% to 30%. The increases in the applied post-tensioning forces were achieved by increasing the stresses in the tendons from 20% to 60% of the yield stresses of the tendons, respectively.

5.6.1 Effects of applied post-tensioning force

Fig. 5.11 shows the effects of changing the applied post-tensioning force on the backbone curves of three different piers of the S-series. The piers have three different aspect ratios (AR) of

3, 6, and 9. As shown in the figure, increasing PT from 10% to 30% increased the piers yield strengths. For a given aspect ratio, increasing the post-tensioning stresses in the tendon led to early yielding of the tendon. Yielding of the tendon is characterized by softening in the backbone curve due to degradation in the lateral strength and stiffness. Under earthquake excitation, yielding of the tendon leads to losses in the post-tensioning forces. However, for all cases presented in the figure, the earliest yielding in a tendon occurred at a drift angle of approximately 7% for pier having an AR = 3 and PT = 30%. A typical bridge pier would reach a drift angle of approximately 6% under the maximum credible earthquake.

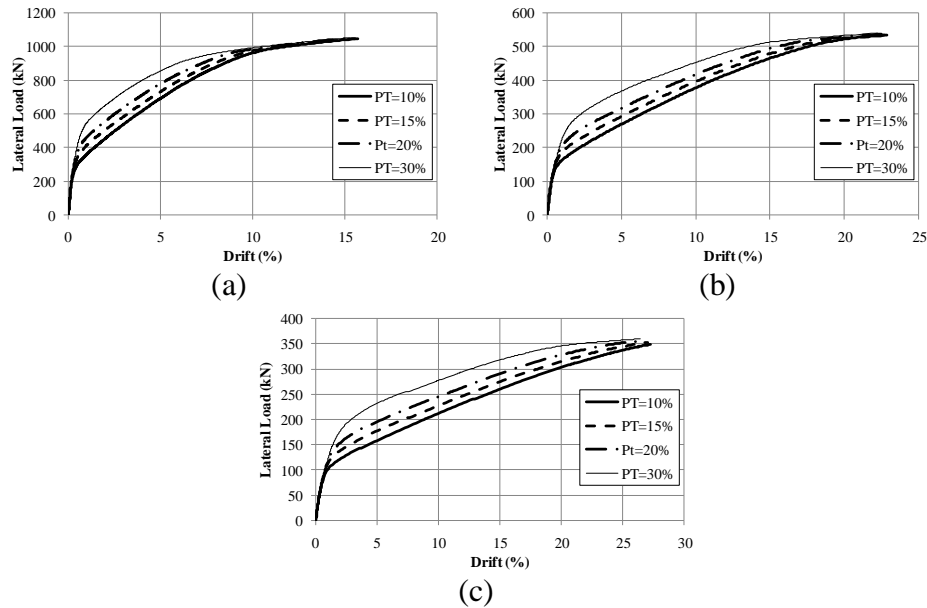


Figure 5.11: Effects of changing the applied post-tensioning forces on the backbone curves of piers having aspect ratios of (a) 3, (b) 6, and (c) 9
(Note the different scales in the graphs)

5.6.2 Effects of load combination

Fig. 5.12 shows the backbone curves for three piers of S series having AR of 3, 6, and 9. The three piers have axial stresses due to the applied gravity load and post-tensioning force, normalized by f'_c , of 25%. However, two different load combinations were investigated. Case I

has $PT = 15\%$ and $DL=10\%$ while case II has $PT=20\%$ and $DL=5\%$. As shown in the figure, for drift angles smaller than approximately one-half the ultimate drift angle of each pier, the backbone curves are sensitive to the total axial stresses. However, beyond such drift angle, piers having higher PT yielded at smaller drift angles compared to those having smaller PT . Relatively early yielding of the tendon in the case of piers having higher PT led to smaller ultimate resistance. Hence, for practical application and within drift angles of 6% or smaller, it seems appropriate for a design model to consider the effect of the total axial stresses.

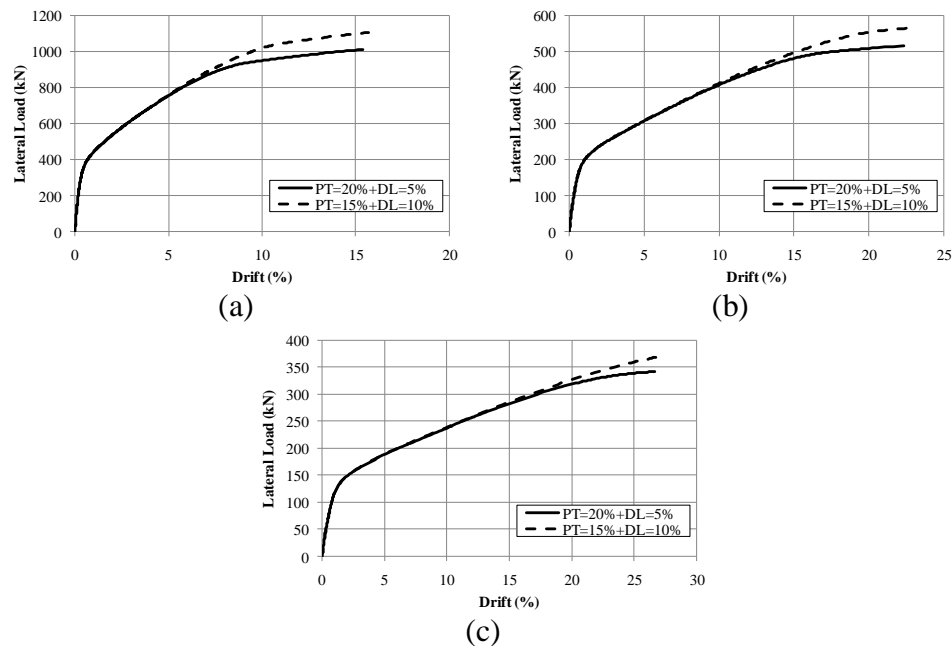


Figure 5.12: Effects of different combinations of axial stresses for piers having $AR =$ (a) 3, (b) 6, and (c) 9 (Note the different scales in the graphs).

5.6.3 Effects of pier aspect ratio

Fig. 5.13 shows the backbone curves for four different piers of the S series having $AR =$ 3, 6, 9, and 15. All the piers had $PT = 20\%$ and $DL = 7\%$. As shown in the figure, decreasing the aspect ratio of a pier increased the pier initial stiffness, yield strength, and ultimate strength. However, such increase in the ultimate strength was accompanied by a significant decrease in the

pier deformation capacity. In addition, yielding of the tendons occurred at small drift angles for squat piers. Yielding of the tendon occurred at drift angles ranged from 10% for $AR = 3$ to 30% for $AR = 15$.

5.6.4 Effects of Pier size

Fig. 5.14 shows the backbone curves for two piers: one pier from the S series and the other one from the L series. Both piers have the same aspect ratio of 3. The piers were investigated under $PT = 10\%$ and 30% . The applied lateral load of the piers was normalized by the cross sectional area of the pier. As shown in the figure, for the same axial stress both piers have the same shear stresses for a given drift angle until opening of the interface joints at the bases of the piers. However, once the interface joints opened, the shear stresses for the smaller pier are higher than those of the larger pier at a given drift angle. Finally, the smaller pier reached yielding of the tendon at smaller drift compared to the larger pier. The tendon yielded at drift angles that ranged from approximately 7% for $PT = 30\%$ to 10% at $PT = 10\%$. The corresponding values for large piers are 10% and 15%, respectively.

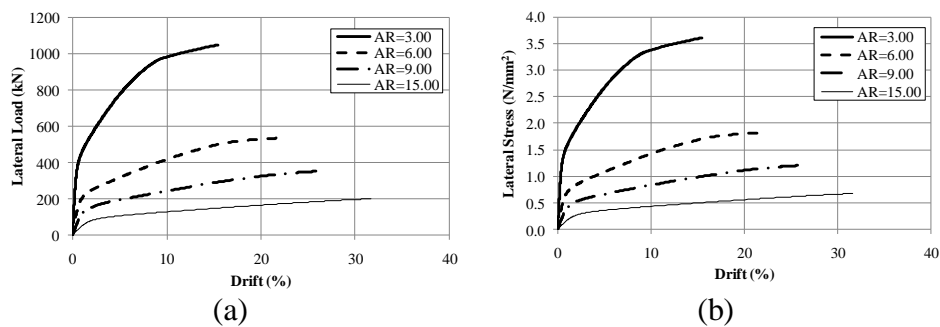


Figure 5.13: Effects of piers aspect ratios on the backbone curves of lateral drift angle vs. a) lateral load; and b) lateral load normalized by the cross sectional area

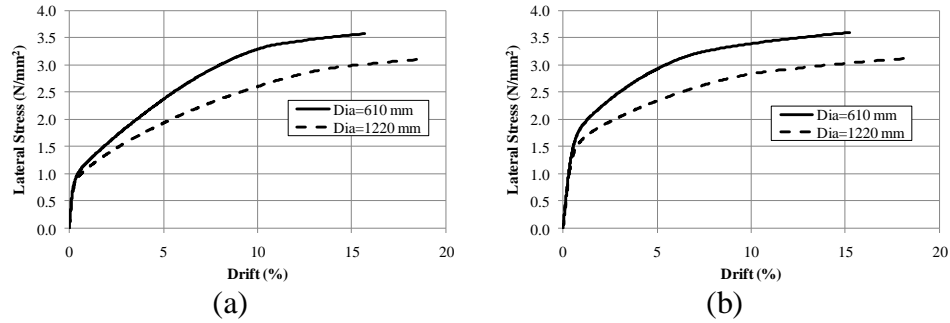


Figure 5.14: Backbone curves for two piers having $AR = 3$ and different sizes for (a) $PT = 10\%$, and (b) $PT = 30\%$

5.6.5 Effects of diameter size

Fig. 5.15 shows the backbone curves for six different piers representing three different groups. Each group includes one pier of the S series and one from the L series having the same height of 3660 mm [144 in], 5490 mm [216 in], or 9150 mm [360 in]. The lateral forces were normalized by the piers cross sectional areas and presented as shear stresses. As shown in the figure, the pier diameter size has a significant effect on the shear stresses and limited effects on the lateral drift angle capacity. Piers of the L series consistently were able to resist higher stresses compared to those of the S series at the same drift angle. For the same pier height, increasing the piers diameter by 100% increased the lateral shear stresses by approximately 100%. Fig. 5.16 shows an approximate mechanism for rocking of two piers having the same height but with different cross sectional diameter. As shown in the figure, for the same drift angle, increasing the pier cross sectional diameter increases the lever arm between the compression forces in the concrete stress block and the tension forces in the tendon. In addition, moving the tendon far from the rocking pivot increases the stretch in the tendon leading to higher post-tensioning stresses and higher lateral resistance. Finally, increasing the diameter size reduced the displacement capacity of the piers. However, all the piers reached a lateral drift angles significantly higher than 6%.

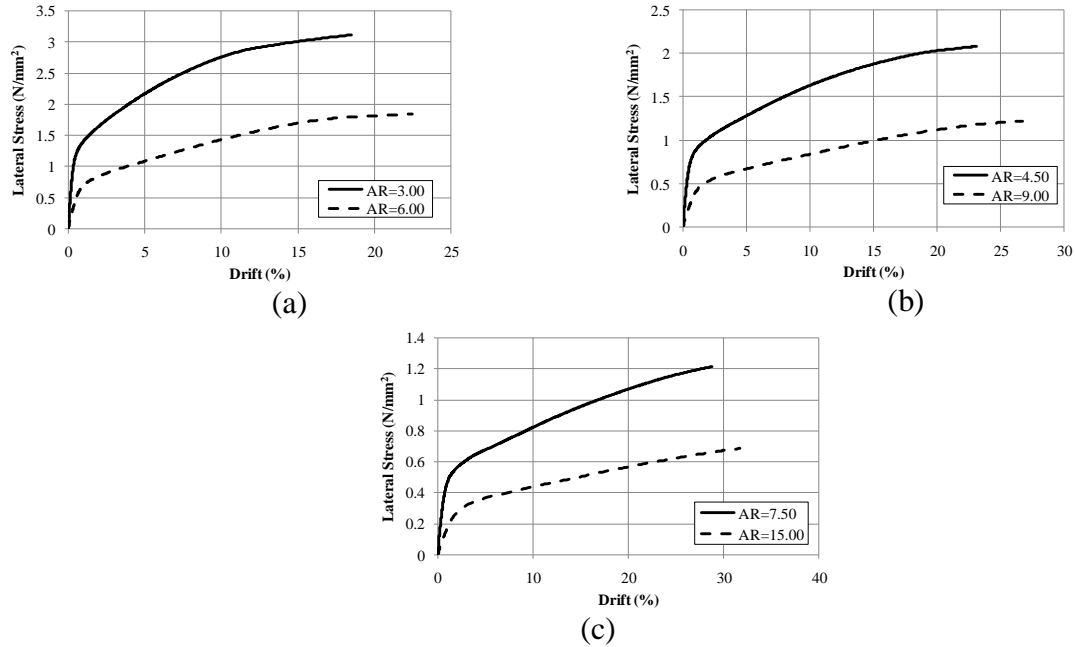


Figure 5.15: Backbone curves for piers from the S series (dashed line) and L series (solid line) having heights of (a) 3660, (b) 5490, and (c) 9150 mm

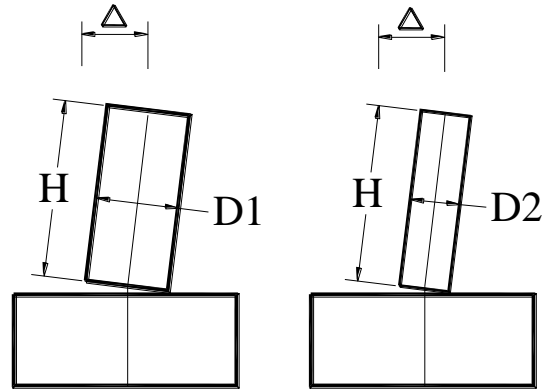


Figure 5.16: An approximate mechanism for rocking of two piers having the same height but with different cross sectional diameter

5.6.6 Effects of confinement

Figs. 5.17 and 5.18 show the backbone curves for four piers: two from the S series and two from the L series. All piers have a height of 5487 mm [216 in]. The piers were subjected to

PT ranged from 10% to 30%. The piers were constructed with two different FRP tubes. Both tubes have the same thickness of FRP but the second tube having a tensile stress of 275.79 MPa [40 ksi] and E modulus of 24,821 MPa [3600 ksi] representing a stronger and stiffer FRP tubes available in the market. Fig. 5.19 shows the stress-strain behavior for the S series and L series confined using the different FRP materials. As shown in Figs. 5.17 and 5.18, increasing the modulus of elasticity and tensile strength of the tubes significantly increased the strengths and the post-elastic stiffness of the piers. The increase in the strength and post-elastic stiffness is more significant in the case of the piers from the S series.

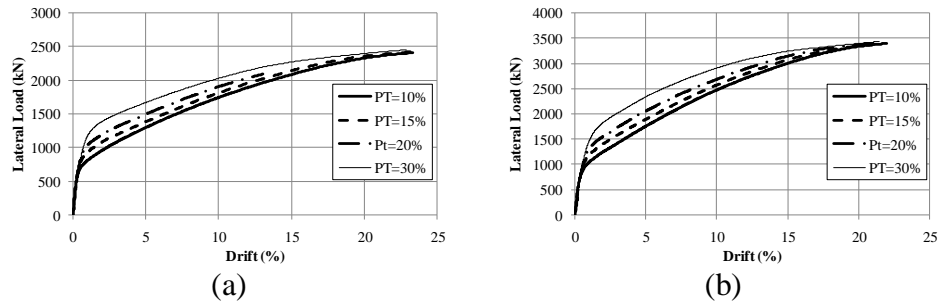


Figure 5.17: Backbone curves for piers of the L series constructed using (a) weak FRP and (b) strong FRP (Note the vertical axis different limits)

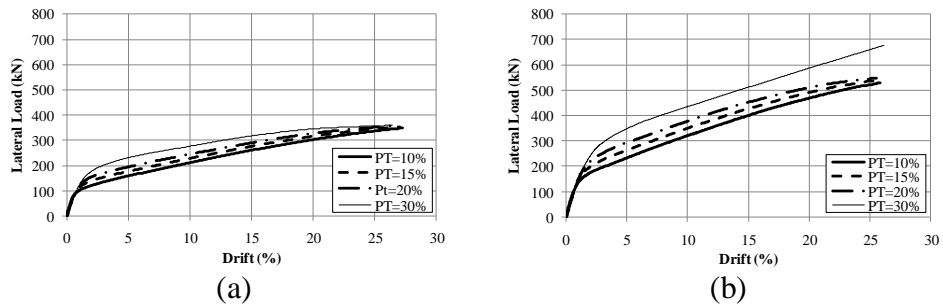


Figure 5.18: Backbone curves for piers of the S series constructed using (a) weak FRP and (b) strong FRP

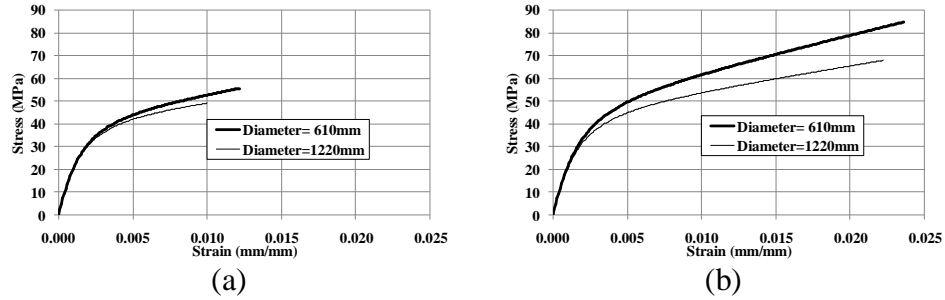


Figure 5.19: The stress-strain relationships for piers from the S and L series confined using (a) weak FRP and (b) strong FRP tubes

5.7 Conclusions

This chapter introduces the implementation of different material behaviors in the previously developed FE model to be able to capture the backbone behavior of SPPT concrete piers and bents tested in Washington State University. This investigation revealed that:

- The FE model was able to capture the backbone behavior of both SPPT concrete piers and bents quite well.
- The grout layer behaved quite well at the beginning of testing, but after that the damage induced by high stress concentrations on it made it softer. This led to reduction in the post-tensioning stresses in the tendon.
- The grout layer used to level the foundation surface, in the case of piers, affected the lateral load at which the tangent stiffness of the system reduces.
- The cement paste as well affected the initial and post-elastic tangent stiffnesses of the SPPT concrete bents.
- Including the cement paste layer in the FE model proved its efficacy as the FE model was then able to capture the bent's behavior very well.

Based on the results of the presented parametric study:

- The level of the applied post-tensioning forces has a significant effect on the backbone of SPPT-CFFT piers. Increasing the applied post-tensioning increased the yield strength of the piers. However, increasing the post-tensioning stresses in the tendons combined with decreasing the pier's height led to yielding of the tendon at relatively small drifts.
- For the parameters chosen for this study and within the feasible drift angle for a pier, the analysis was more sensitive to the total applied axial loads than to the ratio of the applied post-tensioning to gravity loads.
- Increasing the piers' aspect ratios decreased the initial stiffness, ultimate strength, and yield strength but increased the deformation capacity. In addition, tendons in squat piers tend to yield at small drift angles compared to relatively slender piers.
- The analysis showed that the pier size played an important role in the behavior of the piers once the interface joint opened. However, before the interface joint opening, the performance of the piers depended on the piers' aspect ratios.
- For the same pier height, increasing the pier diameter size significantly increased the pier shear stress capacity but had minimal effect on the pier deformation capacity.
- Increasing the tensile strength and E-modulus of the confining tube significantly improved the strength and post-elastic stiffness of the piers. However, it did not have significant effect on the deformation capacity of the piers.

5.8 References

- Booker, A. J. (2008). "Performance of continuous and segmented post-tensioned concrete filled fiber tubes." M.Sc. thesis, Washington State Univ., WA, USA

- Darwish, S.M., and Al-Samhan, A., (2008). "The effect of cement stiffness and tibia tray material on the stresses developed in artificial knee." *Journal of Adhesion*, 28, 120-125.
- Hewes, J. T., and Priestley N. (2002). "Seismic design and performance of precast concrete segmental bridge columns." Report No. SSRP-2001/25, Univ. of California at San Diego.
- Mander, J. B., Priestley, M. J. N., and Park, R. (1988). "Theoretical stress-strain model for confined concrete." *J. Struct. Eng.*, 114(8), 1804–1826.
- Samaan, M., Mirmiran, A., and Shahawy, M. (1998). "Model of concrete confined by fiber composite." *J. Struct. Eng.*, 124(9), 1025–1031.
- Shaalan, A. (2009). "Performance of re-centering moment resisting frames composed of continuous and segmented precast post-tensioned concrete columns confined by FRP tubes" M.Sc. thesis, Washington State Univ., WA, USA

CHAPTER SIX

PERFORMANCE-BASED SEISMIC DESIGN OF UNBONDED SEGMENTAL PRECAST POST-TENSIONED CONCRETE PIERS

Haitham Dawood⁷ Mohamed ElGawady^{8§}

6.1 Abstract

Segmental precast post-tensioned (SPPT) pier system has a self-centering behavior that makes it an attractive system to be used in high seismic zones. The piers investigated in this manuscript are singly segmented. The segment consisted of concrete filled fiber reinforced polymer tubes.

A large set of 84 piers with different design parameters were analyzed using finite element models. The backbone curve of each pier was developed and bilinearized using a standard procedure. The idealized backbone curves were used to develop a set of empirical equations that were able to reproduce the bilinearized backbone curve of a given pier. Different performance criteria have been proposed for the system according to the intensity and the frequency of occurrence of a seismic event. The developed empirical equations were arranged in a design procedure to achieve a given performance level at a specific seismic zone. Finally, the design methodology was verified by comparing the performance output of the empirical procedure against the output of the finite element model.

⁷ Graduate Research Assistant, Dept. of Civil and Environmental Engineering, Washington State University, Pullman, WA, hmousad@msn.com

⁸ Assistant Professor, Dept. of Civil and Environmental Engineering, Washington State University, Pullman, WA, melgawady@wsu.edu;

[§]Corresponding author

6.2 Keywords

Seismic design, post-tensioned, segmental pier, accelerated bridge construction, Performance-based design

6.3 Segmental Precast Post-tensioned (SPPT) Piers

The Kobe earthquake (Japan 1995) resulted in demolishing over 100 reinforced concrete bridge piers that reached residual drift angles in excess of 1.5% (Lee and Billington 2010). This showed the need for a bridge pier's system that not only can withstand high seismic events without collapse, but also that is resilient. Segmental precast-post-tensioned (SPPT) piers show high self-centering capabilities compared to conventional reinforced concrete (RC) piers (Chang et al. 2002, Hewes and Priestley 2002, Chou and Chen 2006, Marriott et al. 2009, ElGawady et al. 2010 (a,b), and ElGawady and Shaalan 2010). SPPT system consists of precast segments stacked over each other and connected by an unbonded post-tensioning tendon. Segments used in those research were hollow or solid sections, reinforced with longitudinal bars and horizontal stirrups or confined with fiber reinforced polymers or confined by steel tubes.

While several experimental work showed the advantage of the SPPT system, this manuscript presents a design procedure for SPPT piers using empirical equations. To accomplish this target, a set of 84 piers having different design parameters were analyzed using a 3D FE model. A nonlinear regression analyses were carried out on the results of this set of piers. The regression analysis resulted in a set of empirical design equations.

6.4 Residual Drift Angles

The study conducted by ElGawady and Shaalan (2010) revealed that the residual displacements for a SPPT bent is approximately equivalent to 10% of the imposed lateral

displacement on that bent. The residual drift angles of the SPPT piers studied by Hewes and Priestley (2002) were on the order of 0.10%, except for one specimen which reached 0.3%. Investigation of the work done by Hewes and Priestley (2002) showed that the residual displacements represent approximately 4% to 5% of the maximum imposed lateral displacement. To be conservative, in this study a residual displacement of 10% of the imposed lateral displacement was adopted. This assumption maybe revised in the future when more experimental data become available.

6.5 Summary of the Finite Element Model

ABAQUS/Standard version 6.8-2, a general purpose finite element code, was selected as a basic platform for developing a 3D finite element (FE) model for this study. The model was presented in detail by Dawood et al. (2010(a)) and verified against three different experimental studies (Dawood et al. (2010(a)), ElGawady and Dawood (2010) and Dawood 2010).

In this manuscript, the SPPT system consisted of one precast segment sandwiched between foundation and superstructure. All piers in this study consisted of concrete filled glass fiber reinforced polymer (GFRP) tubes without any rebars. The system is connected by unbonded post-tensioning tendons passing through ducts made in the segments during casting. The model was built up using 3D continuum elements for concrete and fiber components and 3D beam elements for the post-tensioning tendons (Fig. 6.1).

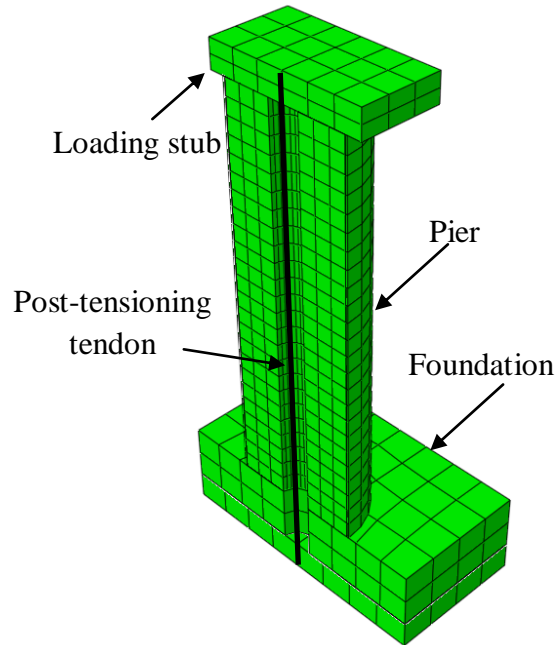


Figure 6.1: FE model for a SPPT pier used in this study

The concrete damaged plasticity model (Lubliner et al. 1989 and Lee and Fenves 1998) was used to model the concrete material behavior while the classic metal plasticity model was used for the tendon's material. The fiber tube was modeled as an elastic orthotropic material. The ends of the tendon were embedded in the loading stub (that represents the superstructure) and the foundation to simulate the tendon's anchorage. The tendon was subjected to a stress type initial condition to simulate its post-tensioning. By neglecting the sliding of the foundation and by assuming a rigid soil underneath the foundation, the bottom surface of the foundation was constrained in the three motional directions. A typical pier loading stages were: a) tendon's post-tensioning; b) application of a vertical external gravity load; and c) application of a monolithically increasing lateral load.

Fig. 6.2 shows the deformed shape of a pier due to the application of the lateral loads. As shown in the figure, the pier attained its lateral deformation through opening of the interface joint

at the base. The FE model successfully captured the overall behavior of the system (i.e., the backbone behavior, stress concentrations at the pier's toe and failure modes). More details about the model description, its implementation and validation procedures along with an in-depth parametric studies are presented by Dawood et al. (2010 a, b).

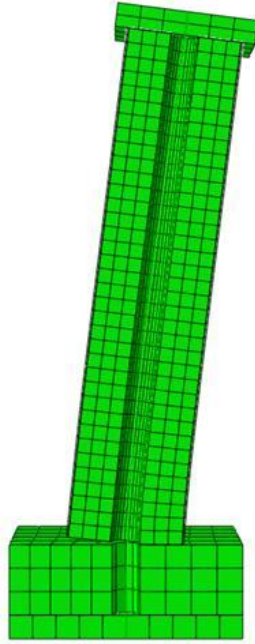


Figure 6.2: Deformed shape of the pier

6.6 Study Description

The previously described FE model was used to investigate the behavior of a large matrix of 84 piers having different design parameters, namely, height, diameter, effective post-tensioning load, and external gravity load. The values studied for each parameter are listed in table 6.1. The piers were built up using plain concrete with a characteristic compressive strength (f'_c) of 41.4 MPa [6000 psi] cast directly in glass fiber reinforced polymer (GFRP) confining tubes 19 mm [0.75in] thick (Table 6.2). The investigated piers have heights ranging from 1830mm [72 in] to 9144mm [360 in] and cross sectional diameter of either 1220 mm [48 in] or

610 mm [24 in]. This resulted in piers having aspect ratios of 3 to 15. The stress on the concrete induced by the gravity load normalized by its f'_c (DL) ranged from 5% to 10%. While, the stress on the concrete induced by the post-tensioning force normalized by its f'_c (PT) ranged from 10% to 30%.

Table 6.1: Different investigated parameters for the SPPT piers

Height	Diameter	PT	DL
1830 mm [72 in]	1220 mm [48 in]	10%	5%
3660 mm [144 in]	610 mm [24 in]	15%	7%
5490 mm [216 in]	-	20%	10%
9144 mm [360 in]	-	30%	-

Table 6.2: Material Properties of the GFRP tubes

Flexural Modulus Longitudinal	13790 MPa [2,000 ksi]
Tensile Strength Longitudinal	634 MPa [9.2 ksi]
Poisson's Ratio	0.35

Throughout this study, Samaan et al.'s (1998) model was used for developing the stress-strain behavior of concrete confined by GFRP. Fig. 6.3 shows the developed stress strain curves for the concrete of piers with different diameters. As shown in the figure, although the GFRP and concrete were identical in both cases, the confining effect increased as the diameter of the cross section decreased. The concrete was defined using a density of 2214 kg/m³ [0.08 lb/in³], Young's modulus of 25,414MPa [3686 ksi] and a Poisson's ratio of 0.2.

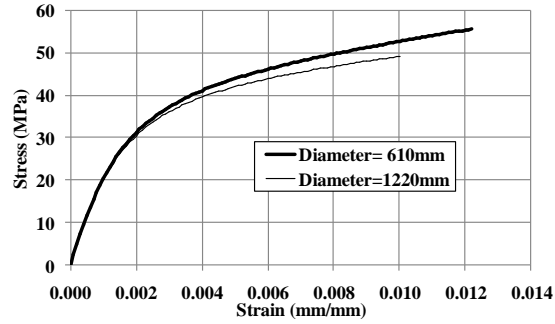


Figure 6.3: Compressive stress strain relationship obtained from Samaan et al. (1998) to model the GFRP confined concrete of the piers

The post-tensioning tendon used in the investigation had an equivalent nominal diameter of either 176 mm [6.92 in] or 93 mm [3.68 in] which resulted in a reinforcement ratio of 2.00% and 2.35% for piers having cross sectional diameters of 1220 mm [48 in] and 610 mm [24 in], respectively. These diameters were selected such that the post-tensioning stress in the tendons were 20% (25%), 30% (38%), 40% (51%) and 60% (76%) of their ultimate (yield) strength. The axial stresses in the piers cross sections due to these applied post-tensioning forces (PT) were 10%, 15%, 20% and 30% of f'_c , respectively. The post-tensioning tendon was defined with a Young's modulus of 204,774 MPa [29,700ksi], Poisson's ratio of 0.3, yield stress of 874 MPa [126.8 ksi] and ultimate stress of 1110 MPa [160.9 ksi].

6.7 Performance levels

The performance-based seismic design of a structure necessitates specifying performance criteria for each seismic hazard level. Two performance levels were proposed by Kwan and Billington (2003), namely functional and survival, and Wight et al. (2007), namely serviceability and ultimate, for the design of unbonded post-tensioned piers and masonry walls, respectively. However, there is no consensus on the different performance levels and its criteria for

unbounded post-tensioned structural elements. For the SPPT system investigated in this study, the following performance levels were adopted.

6.7.1 Performance criteria for the serviceability level

The serviceability performance point is associated with the smallest among: a) drift angle when the concrete reaches its theoretical ultimate confined strain (ϵ_n); b) drift angle at which the stress in the tendon reaches 90% of its yield stress; c) drift angle corresponding to 70% of the pier's ultimate drift angle; and d) drift angle of 2%. The drift angle is defined as the ratio between the measured lateral displacement at the point of load application and the height of this point of load application above the pier's foundation.

Criterion 'a' was chosen to insure that no toe crushing will occur, similar criterion was adopted by Wight et al. (2007) for rocking masonry walls. Currently, the available models for predicting the stress-strain behavior of confined concrete are quite conservative in predicting the ultimate strain (e.g., Mander et al. 1988, Samaan et al. 1998, Fam and Rizkalla 2001, Beque et al. 2003, and Teng et al. 2009). Hence, a rocking pier should be able to resist lateral loads well beyond those causing the confined concrete to reach its theoretical ultimate strains. In addition, experimental work showed that rocking piers suffered minimal, easy repairable, damage with minimal residual crack widths when they were subjected to lateral loads causing the confined concrete, at their toes, to reach its theoretical ultimate strain.

Criterion 'b' was chosen as a fraction of the yielding stress of the tendon to give a margin of safety against yielding. Wight et al. (2007) adopted similar criterion for rocking masonry walls. Kurama (1997) and Kwan and Billington (2003) used 100% of F_y as a criterion for the serviceability performance level. However, yielding of tendons lead to loss in the applied post-tensioning forces, stiffness degradation, and reduction in the self-centering capability of the

SPPT system. Hence, the authors of this manuscript believe in having a margin of safety against yielding of the post-tensioning tendons.

Criterion 'c' was adopted by Kwan and Billington (2003) to provide the piers with a sufficient margin of safety against brittle failure. Criterion 'd' was proposed also to ensure a sufficient margin of safety against brittle failure and to ensure minimal residual drift angle.

For rocking structures, criteria 'a' and 'b' may occur just before or after the collapse-prevention performance level. This indicated the importance of criteria 'c' and 'd'.

6.7.2 Performance criteria for the collapse-prevention level

The collapse-prevention performance point is associated with the smallest drift angle among: a) drift angle at which the post-tensioning tendons yield; b) drift angle level of 4.5%; and c) drift angle that cause a residual drift angle of 1.0%.

Criterion 'a' was chosen to avoid tendons yielding as discussed before (Kurama 1997 and Kwan and Billington 2003). Criterion 'b' was adopted from Priestley et al. (2007) for bridges. Criterion 'c' was adopted from Kwan and Billington (2003).

6.8 Equivalent viscous damping

Equivalent viscous damping is an essential parameter that affects the behavior of a structural system under seismic excitations. Hewes and Priestley (2002) reported an average equivalent viscous damping of approximately 5% up to a drift angle of 3% with higher values associated with low confinement due to the damage increase; then, it increased due to spalling of concrete cover of the reinforced concrete segments. Chou and Chen (2006) reported that the equivalent viscous damping was 6.5% on average for SPPT piers with a minimum value that was

approximately 6%. ElGawady et al. (2010) reported an average equivalent viscous damping of 5% for single segmented pier similar to those investigated in this study. For this study, a constant 5% equivalent viscous damping was assumed for all drift levels as the concrete core was externally confined with the GFRP so no concrete cover spalling would occur before the rupture of the GFRP and collapse of the system.

6.9 Study Procedure

This study provides a simplified design procedure for SPPT piers, consisting of CFFT segments, using simplified empirical equations. The use of empirical equations will help a design engineer to avoid going through the cumbersome FE analysis.

To accomplish this target, the following steps were carried out: a) the serviceability and collapse-prevention performance levels were determined using the criteria discussed before; b) the backbone curves obtained from the results of the FE models of the 84 piers were bilinearized following FEMA 356, in this case the performance displacement for serviceability and collapse-prevention were used as Δ_u in the FEMA procedure (Fig. 6.4) (i.e., for each pier two bilinearized backbone curves were prepared); c) each parameter in the bilinear backbone curve (i.e. K_e , Δ_y , F_y , Δ_u , F_u and α (Fig. 6.4)) was studied separately and a nonlinear regression analyses were carried out to develop an empirical equation for the prediction of each parameter; d) an empirical equation for predicting the post-tensioning stresses in the tendon, at different drift levels, was derived;

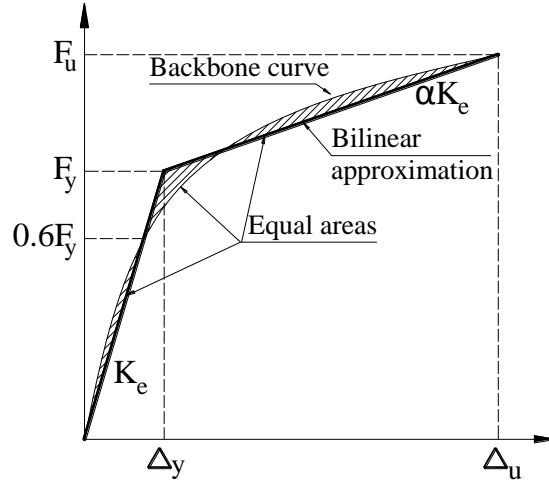


Figure 6.4: Backbone curve along with its bilinearized form (FEMA 356)

e) a simplified systematic procedure was derived for the design of SPPT pier system using the developed empirical equations. Once the empirical equations were developed, the errors in predicting the parameters corresponding to the bilinear system were calculated using Eq. 6.1.

Error in calculating parameter A (%) =

$$\frac{A_{\text{from the empirical equation}} - A_{\text{from the bilinear approximation}}}{A_{\text{from the bilinear approximation}}} \% \quad (\text{Equation 6.1})$$

6.10 Collapse-prevention and Serviceability Performance levels

6.10.1 Effective stiffnesses (K_{CP-e} and K_{S-e})

The nonlinear regression analyses of the data of the 84 piers showed that the effective stiffness is a function in (EI/H) ; where, E: is the modulus of elasticity of the pier's concrete (kN/mm^2); I: is the moment of inertia of the pier's cross section (mm^4); and H is the height of the pier (mm). The effective stiffness was found to be inversely proportional to PT. Eq. 6.2 was

found to best predict the effective stiffness for both, the collapse prevention (K_{CP-e}) and serviceability (K_{S-e}) performance levels.

$$K_{CP-e} \text{ (kN/mm)} = K_{S-e} \text{ (kN/mm)} = \frac{1.82}{PT^{0.3}} \frac{3EI}{H^3} \quad (\text{Equation 6.2})$$

The mean (μ), standard deviation (σ), and coefficient of variation (C_v) of the errors in computing the effective stiffness of the system for the 84 piers using Eq. 6.1 is shown in Table 6.3. As shown in the table, Eq. 6.2 predicts quite well K_{CP-e} and K_{S-e} . The μ of the error in predicting K_{CP-e} was +1.0% and +3.2% with σ of 10.5% and 9.6% when using all piers and 72 piers, respectively. On the other hand, the μ of the error in predicting K_{S-e} was -2.3% and -0.1% with σ of 10.2% and 9.1% when using all piers and 72 piers, respectively

6.10.2 Yield loads (F_{CP-y} and F_{S-y})

For a rocking structure, the apparent yielding of the structure is different from yielding of the unbounded tendon and occurs well before the tendons' yield (Kwan and Billington 2003). In this manuscript, the yield load (F_{CP-y}) will be used to refer to the apparent yielding of the structure and was defined as the lateral load at which the stiffness of the pier reduces abruptly by a factor α (Fig. 6.4). Fig. 6.5 shows the relationship between the design parameters of the piers vs. the yield loads of the piers (kN). The load combination is represented by the horizontal axis and is defined as two percentages separated by a dash; the first (left, PT) is the stress on the concrete induced by the post-tensioning; and the second (right, DL) is the stress on the concrete induced by the gravity load. Both were normalized by the concrete's f'_c . In the figure, piers with the same dimensions are assigned a specific marker type and a code for each dimension is shown under the figure (e.g., H5490-D0610 is a pier with a height of 5490 mm and a diameter of 610 mm).

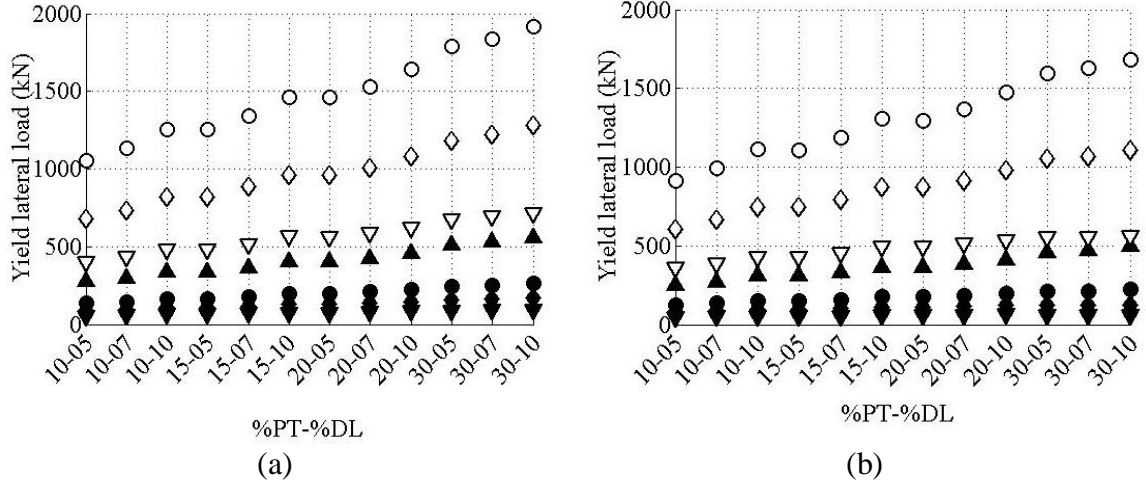


Figure 6.5: The yield load associated with each specific pier for a) collapse-prevention performance level; and b) serviceability performance level

▲ H1830-D0610 ◇ H5490-D1220 ▽ H9144-D1220
 ○ H3660-D1220 ◆ H5490-D0610 ▼ H9144-D0610
 ● H3660-D0610

Fig. 6.5 shows that F_{CP-y} and F_{S-y} are directly proportional to the value of the combination of loads acting on the pier. For piers with the same diameter, increasing the height decreases F_{CP-y} and F_{S-y} . On the other hand, for piers with the same height, increasing the diameter increases F_{CP-y} and F_{S-y} . Based on the previously mentioned observations, Eqs. 3 and 4 were developed through a nonlinear regression analysis.

$$F_{CP-y} \text{ (kN)} = \frac{D^{2.8} PT^{0.4} DL^{0.2}}{400 H} \quad (\text{Equation 6.3})$$

$$F_{S-y} \text{ (kN)} = \frac{D^{2.8} PT^{0.4} DL^{0.2}}{480 H} \quad (\text{Equation 6.4})$$

Where D is the diameter of the pier (mm).

The error associated with using Eqs. 3 and 4 to get F_{CP-y} and F_{S-y} for each pier is computed using Eq. 6.1 and is presented in Table 6.3. The μ of the error in predicting F_{CP-y} was -7.5% and -6.4% with σ of 4.9% and 3.8% when using all piers and 72 piers, respectively. On the

other hand, the μ of the error in predicting F_{S-y} was +3.0% and +1.7% with σ of 6.4% and 5.6% when using all piers and 72 piers, respectively

6.10.3 Displacements corresponding to yield loads (Δ_{CP-y} and Δ_{S-y})

The yield displacements for collapse-prevention (Δ_{CP-y}) and serviceability (Δ_{S-y}) performance levels were calculated using Eqs. 5 and 6, respectively.

$$\Delta_{CP-y} \text{ (mm)} = \frac{F_{CP-y}}{K_{CP-e}} \quad \text{(Equation 6.5)}$$

$$\Delta_{S-y} \text{ (mm)} = \frac{F_{S-y}}{K_{S-e}} \quad \text{(Equation 6.6)}$$

The μ , σ , and C_v of the errors in computing the yield displacements of the system using Eqs. 5 and 6 for the 84 and 72 piers are presented in Table 6.3. As shown in the table, the μ of the error in predicting Δ_{CP-y} was +2.1% and -2.3% with σ of 15.5% and 11.8% when using all piers and 72 piers, respectively. On the other hand, the μ of the error in predicting Δ_{S-y} was +3.5% and -4.1% with σ of 24.0% and 13.6% when using all piers and 72 piers, respectively

6.10.4 Performance displacements (Δ_{CP-P} and Δ_{S-P})

The collapse-prevention performance displacement (Δ_{CP-P}) is the lateral displacement that fulfills all the collapse-prevention performance criteria discussed earlier in this manuscript. The prevailing performance objective in all the 84 piers analyzed in this manuscript was the 4.5% of lateral drift angle (criterion b). As a result, the collapse-prevention performance point can be calculated using Eq. 6.7.

$$\Delta_{CP-P} \text{ (mm)} = 4.5\% H \quad \text{(Equation 6.7)}$$

The serviceability performance displacement (Δ_{S-P}) is the lateral displacement that fulfills all the serviceability performance criteria discussed earlier in this manuscript. Criteria “d” dominated the performance of all the 84 piers; hence, Eq. 6.8 can be used to calculate the performance displacement at the serviceability performance level.

$$\Delta_{S-P} \text{ (mm)} = 2.0\% H \quad (\text{Equation 6.8})$$

6.10.5 Performance loads (F_{CP-P} and F_{S-P})

The performance loads are the lateral loads corresponding to Δ_{CP-P} and Δ_{S-P} for the collapse-prevention (F_{CP-P}) and serviceability (F_{S-P}) performance levels, respectively. Fig. 6.6 shows that the performance loads (F_{cp-p} & F_{s-p}) for each pier analyzed in this manuscript. The figure shows that the performance loads like the yield loads, are directly proportional to the load combination imposed on the pier as well as the pier’s diameter. Also, it is inversely proportional to the pier’s height. From the nonlinear regression analysis, Eqs. 9 and 10 were derived for predicting the collapse-prevention and the serviceability performance loads, respectively.

$$F_{cp-p} \text{ (kN)} = \frac{D^{3.0} PT^{0.2} DL^{0.1}}{40 H^{1.3}} \quad (\text{Equation 6.9})$$

$$F_{s-p} \text{ (kN)} = \frac{3 D^{3.0} PT^{0.3} DL^{0.1}}{1000 H^{1.1}} \quad (\text{Equation 6.10})$$

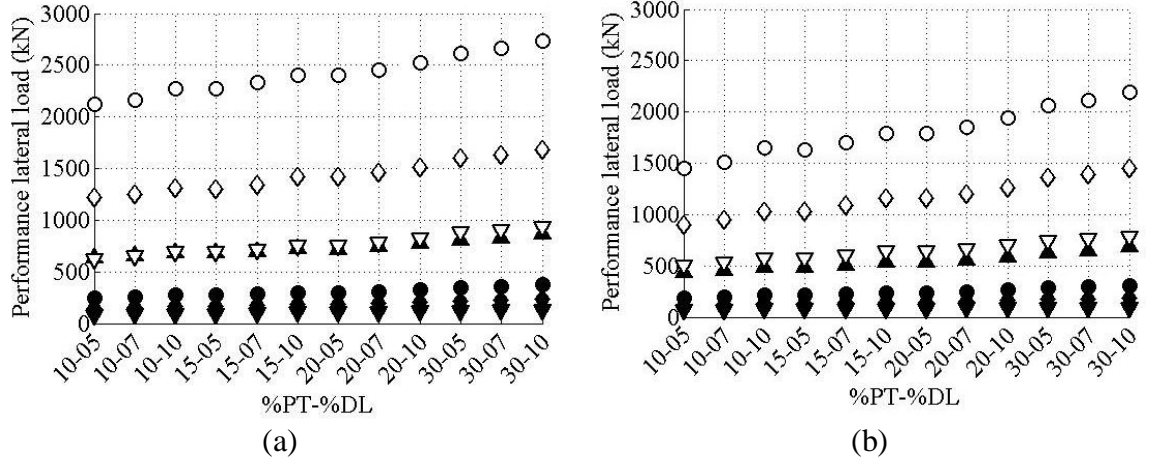


Figure 6.6: The performance load associated with each specific pier: a) collapse-prevention, and b) serviceability performance levels

▲ H1830-D0610 ◇ H5490-D1220 ▽ H9144-D1220
○ H3660-D1220 ◆ H5490-D0610 ▼ H9144-D0610
● H3660-D0610

The errors in predicting F_{CP-P} and F_{S-P} for all specimens using Eqs. 9 and 10 are shown in Table 6.3. As shown in the table, the μ of the error in predicting F_{CP-P} was +1.6% and -0.1% with σ of 6.1% and 4.5% when using all piers and 72 piers, respectively. On the other hand, the μ of the error in predicting F_{S-P} was -0.9% and -5.3% with σ of 13.5% and 6.1% when using all piers and 72 piers, respectively

6.11 Error in predicting the bilinearized backbone curves

Eqs. 1, 3, 5, 7, and 9 as well as Eqs. 1, 4, 5, 8, and 10 were used to develop empirical bilinearized backbone curves for the considered 84 piers at collapse-prevention and serviceability performance levels. To assess the overall accuracy of this empirical approach, the error in predicting the bilinearized lateral resistance of each pier at each lateral drift angle was calculated using Eq. 6.1 and plotted in Fig. 6.7. The figures show the error calculated for the 84 piers (thin gray lines) superimposed with the line representing the mean error (continuous black line) and the lines representing the mean error plus or minus the standard deviation ($\mu \pm \sigma$) (dotted black lines).

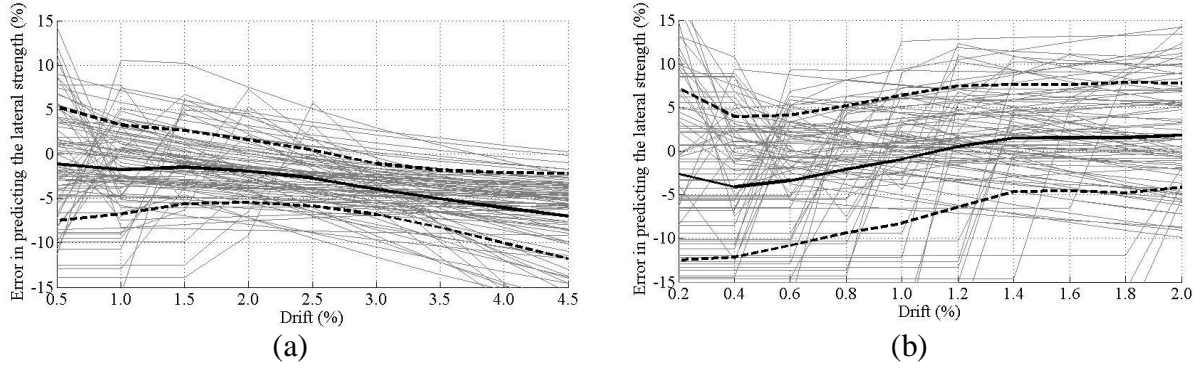


Figure 6.7: The lateral drift angle vs. the error in predicting the pier's strength: a) collapse-prevention performance level, and b) serviceability performance level.

In the case of collapse-prevention performance level, the error in predicting the lateral strength of the piers using the set of empirical equations ranged from -20% to +15%. The figure shows that, the mean (μ) error in predicting the lateral strength for all the studied piers ranged from -1.1% to -7.0% for all drift angles. The standard deviation (σ) ranged from 2.8% to 6.4%. This resulted in a ($\mu \pm \sigma$) that ranges from -11.8% to +5.3% and a ($\mu \pm 2\sigma$) that ranges from -16.6% to +11.7%. Assuming that the piers represents a normally distributed community, then 68% of the piers have an error in predicting its strength ranging from -11.8% to +5.3% , and 95% of the piers have an error ranging from -16.6% to +11.7%.

In the case of serviceability performance level, the error in predicting the lateral strength for all piers at all drifts ranged from -23% to +19% with μ ranging from -4.1% to 1.8% and σ ranging from 6.0% to 9.9%. This resulted in 68% of the piers have an error range ($\mu \pm \sigma$) from -12.5% to 7.8% and 95% of the piers have an error range ($\mu \pm 2\sigma$) from -22.3% to 17.1% when using the empirical procedure to calculate its lateral strength.

A general observation was that, the piers with an aspect ratio of 15 had a quite larger error margins if compared against the other aspect ratios (from 3 to 9). Hence, caution should be used when using the proposed empirical equation for piers having high aspect ratio.

Table 6.3: Mean, standard deviation and coefficient of variation of the error associated with using the empirical equations

	Collapse-prevention performance level				Serviceability performance level			
	84 piers		72 piers		84 piers		72 piers	
	μ (%)	σ (%)	μ (%)	σ (%)	μ (%)	σ (%)	μ (%)	σ (%)
K_e	+1.0	10.5	+3.2	9.6	-2.3	10.2	-0.1	9.1
Δ_y	+2.1	15.5	-2.3	11.8	+3.5	24.0	-4.1	13.6
F_y	+1.6	6.1	-0.1	4.5	-0.9	13.5	-5.3	6.1
F_p	-7.5	4.9	-6.4	3.8	+3.0	6.4	+1.7	5.6

6.12 Increases in the post-tensioning force with increasing the applied lateral drift angle

Finding an empirical correlation between the lateral displacement and the increase in post-tensioning stress in the tendons for the SPPT piers is essential for designing the tendon's cross sectional area for each pier during the design procedure. Fig. 6.8 shows the increase in the post-tensioning stress normalized by its initial value Vs. the lateral drift angle. The topmost curve represents a loading combination of 10% from PT and 5% from DL and the curves below it represent (10%PT-7%DL, 10%PT-10%DL, 15%PT-5%DL, 15%PT-7%DL, ...etc).

For high vertical load combinations, at small lateral displacements, there were losses in the post-tensioning stresses. Beyond such displacements, the post-tensioning stresses started to increase. Once the neutral axis of the bottommost surface of the pier reached the tendon's location, the tendon started to stretch and the post-tensioning stresses increased approximately linearly versus increasing the applied lateral drift angle.

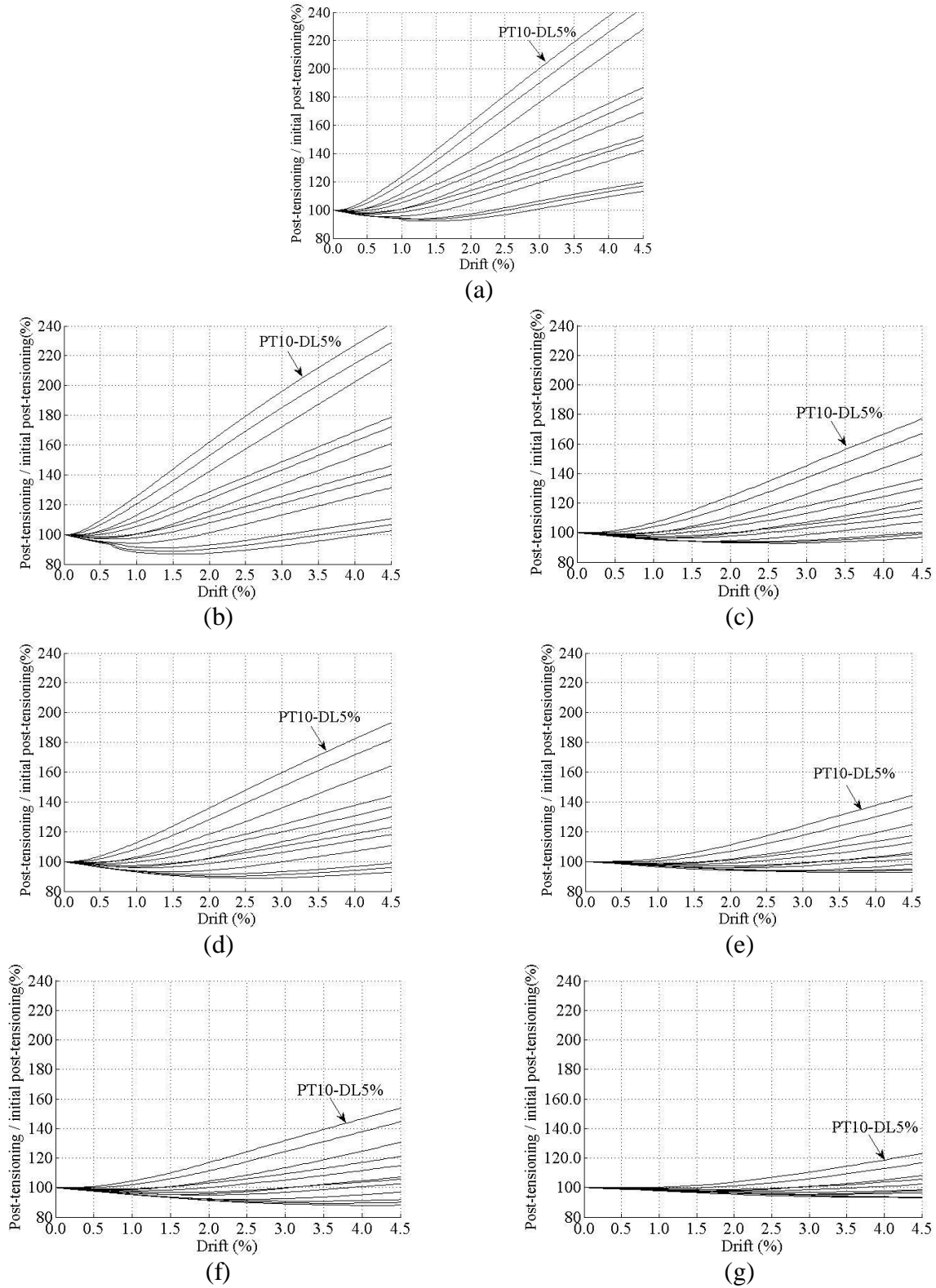


Figure 6.8: The relationship between the lateral drift angle (%) vs. the stress in the post-tensioning tendon's normalized by its initial stress for piers; a) H1830-D0610; b) H3660-D1220; c) H3660-D0610; d) H5490-D1220; e) H5490-D0610; f) H9144-D1220; and g) H9144-D0610

For piers subjected to relatively small vertical load combinations. The piers behaved more as a rigid block. For small lateral displacements, the post-tensioning force was approximately constant. Once the opening at the interface joint between the pier and the foundation reached the location of the tendon the post-tensioning force increased approximately linear with increasing the lateral displacement. It is worth noting that the same behavior was observed by Yamashita and Sanders (2009) for segmental post-tensioned hollow core piers.

The different graphs presented in Fig. 6.8, shows that the rate of stress increase is directly proportional to the stress induced by the post-tensioning stress on the concrete. On the other hand, the stress induced on the concrete by the applied gravity load does not seem to significantly affect that slope. For piers with the same height, those with smaller diameters have much milder rate of increase of the post-tensioning stress. For piers with the same diameter, increasing the height decreases the post-tensioning stress rate of increase. Upon these observations, a nonlinear regression analysis was carried out and resulted in Eq. 6.11 that represents the stress in the post-tensioning tendons as a function of lateral drift angles.

$$\sigma_{PT} = \begin{cases} \sigma_i & : \Delta \leq \Delta_0 \\ \sigma_i \left[1 + \frac{10^4 D^{0.78}}{P_T^{1.4} H^2} (\Delta - \Delta_0) \right] & : \Delta > \Delta_0 \end{cases} \quad (\text{Equation 6.11})$$

Where, Δ is the lateral displacement of the pier (mm); σ_{PT} is the final stress in the post-tensioning tendon at a lateral displacement Δ ; σ_i is the effective post-tensioning stress in the tendon before subjecting the pier to lateral loading; Δ_0 is the lateral displacement (mm) at which the post-tensioning stress in the tendon starts to increase (Eq. 6.12).

$$\Delta_0(\text{mm}) = \frac{H^{1.9} P_T^{1.7} D L^{0.6}}{10^5 D^{0.9}} \quad (\text{Equation 6.12})$$

The accuracy of the previously introduced empirical equations was assessed using Eq. 6.1 and the errors were plotted vs. the lateral drift angle for the 84 piers (Fig. 6.9). In Fig. 6.9, the error of all piers is represented by the gray lines while the mean error is represented by the black continuous line, and the dotted black lines represent the $\mu \pm \sigma$.

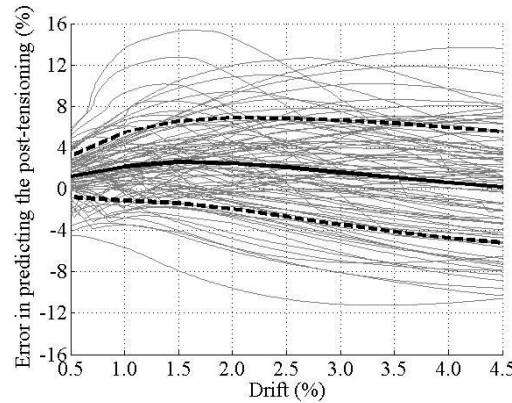


Figure 6.9: Error in predicting the post-tensioning stress in the tendons Vs. lateral drift angle

The error in predicting the post-tensioning value ranged from -12% to +16%. The figure shows that the μ of the error in predicting the post-tensioning stress in the tendons for all the studied piers ranged from +0.18% to +2.59% for all drift angles up to 4.5%. The standard deviation (σ) ranged from 2.00% to 5.37%. This resulted in a $(\mu \pm \sigma)$ that ranges from -5.19% to +6.89% and a $(\mu \pm 2\sigma)$ that ranges from -10.55% to 11.64%. Assuming that the piers represent a normally distributed community, then 68% of the piers will have an error range in predicting their strength of -5.19% to +6.89%, and 95% of the piers will have an error range of -10.55% to 11.64%.

6.13 Design Procedure

Fig. 6.10 shows a flow chart diagram of the proposed design procedure for the SPPT piers. The procedure can be summarized in the following steps:

1) Two uniform hazard acceleration spectra (period vs. spectral acceleration) are obtained according to the location of the bridge.

2) The two uniform hazard spectra (5% damping) are then converted into uniform hazard displacement spectra (period vs. spectral displacement) using Eq. 6.13 (e.g. Priestley et al. 2007),

$$S_d(T) = \frac{T^2}{4\pi^2} S_a(T) \quad (\text{Equation 6.13})$$

Where T is the period of the structure in seconds; $S_d(T)$ is the spectral displacement at a period of T seconds; and $S_a(T)$ is the spectral acceleration at a period T .

3) Given the height of the pier, the performance lateral displacements for the two performance levels (Δ_{CP-P}) and (Δ_{S-P}) can be calculated using Eqs. 5 and 6, respectively;

4) The uniform hazard displacement spectra (step 2), along with Δ_{CP-P} and Δ_{S-P} , are used to obtain the target periods of the pier at the collapse-prevention (T_{CP-P}) and serviceability (T_{S-P}) performance levels (Fig. 6.11).

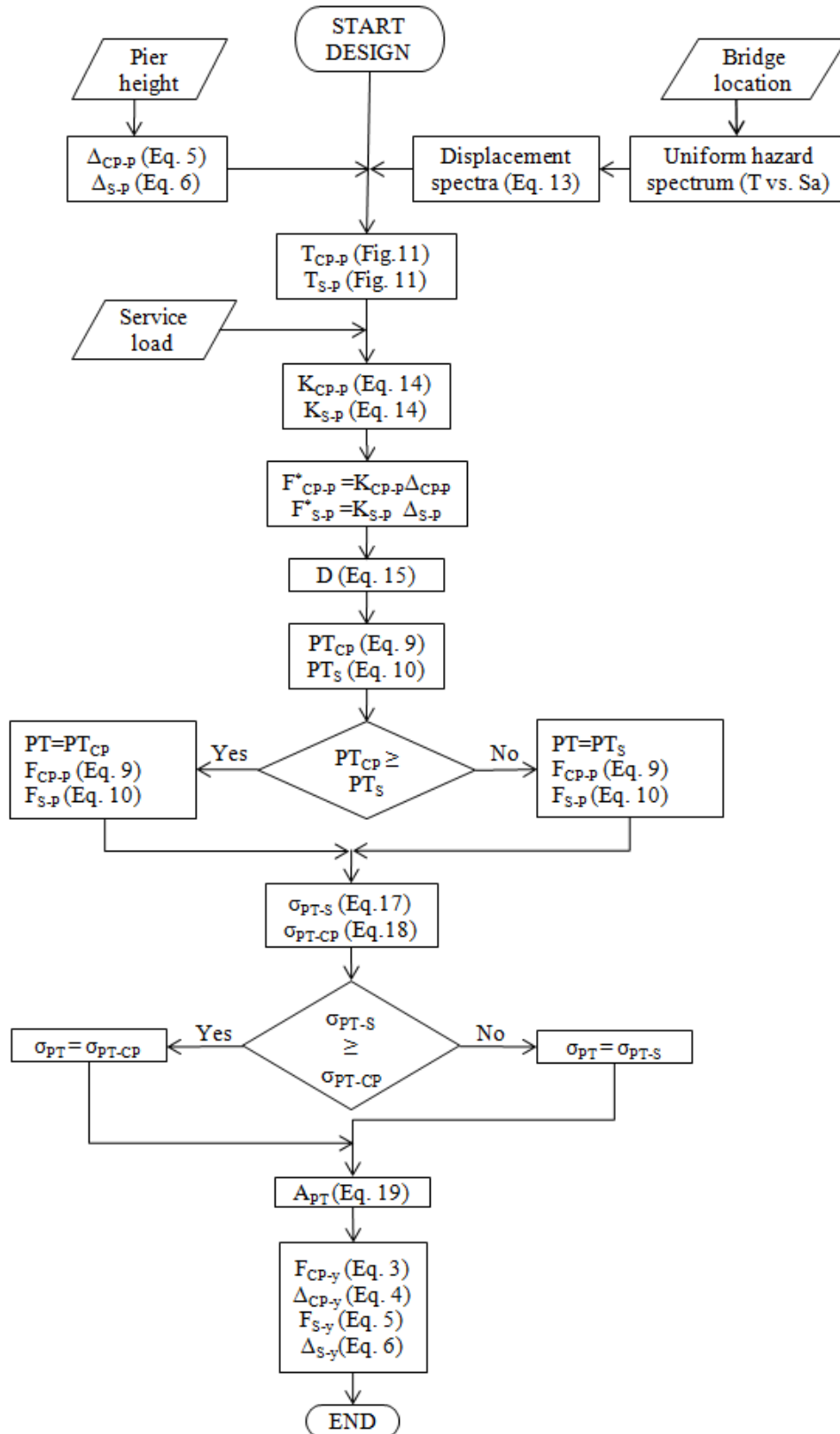


Figure 6.10: Flow chart diagram of the proposed design procedure for SPPT piers

* means that this is a temporary value that will be checked later on

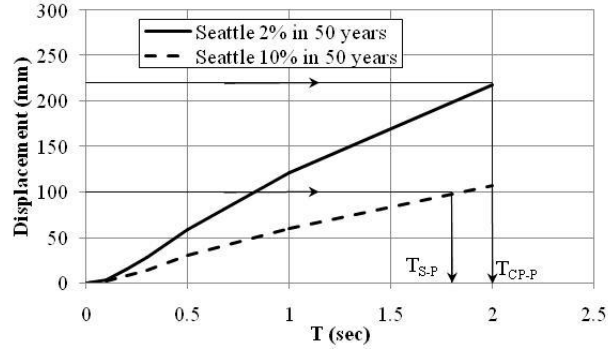


Figure 6.11: A diagram showing how to obtain the target periods of the pier from the uniform hazard displacement spectra of the Seattle, WA area

5) The tributary mass acting on the pier (m) along with T_{CP-P} and T_{S-P} are used to calculate the target secant stiffnesses (Eq. 6.14) of the pier for collapse-prevention and serviceability using the respective periods (step 4).

$$K_{CP-P} = \frac{4\pi^2 m}{T_{CP-P}^2} \quad (\text{Equation 6.14-a})$$

$$K_{S-P} = \frac{4\pi^2 m}{T_{S-P}^2} \quad (\text{Equation 6.14-b})$$

6) The target performance lateral loads (F_{CP-P}^*) and (F_{S-P}^*) are computed by multiplying the secant stiffness (i.e., K_{CP-P} and K_{S-P}) by its corresponding performance lateral displacement.

7) A diameter (D) for the pier should be reasonably assumed or alternatively computed using Eq. 6.15 which is an approximate equation that gives an estimation of the diameter that is most likely to fulfill the target performance levels. The post-tensioning stress on concrete as a percentage of f'_c (PT^*) is then calculated using Eq. 6.9.

$$D \text{ (mm)} = 10.5 F_{CP-P}^{0.33} H^{0.42} / T_{CP-P} \quad (\text{Equation 6.15})$$

8) PT_{CP} and PT_S which represent the post-tensioning stress on the concrete required to assure the pier to reach the performance lateral displacement, are computed using Eqs. 9 and 10, respectively.

9) If $PT_{CP} \geq PT_S$ then the final PT equals to PT_{CP} . This means that the pier should reach F_{CP-P} at lateral displacement of Δ_{CP-P} . While the pier will reach F_{S-P} at a lateral displacement which is smaller than Δ_{S-P} . On the other hand, If $PT_S \geq PT_{CP}$ then the final PT equals to PT_S . This means that the pier should reach F_{CP-P} at lateral displacement smaller than Δ_{CP-P} . While the pier will reach F_{S-P} at a lateral displacement of Δ_{S-P} .

10) The target initial stress in the post-tensioning tendons (Eq. 6.16) is taken as the minimum of the stress values computed using Eqs. 6.17 and 6.18, where; σ_{PT-S} is the initial post-tensioning stress in the tendons that will make the tendons reach 90% of their yield stress when the lateral displacement of the pier reaches Δ_{S-P} ; σ_{PT-CP} is the initial post-tensioning stress in the tendons that will make the tendons reach 100% of their yield stress when the lateral displacement of the pier reaches Δ_{CP-P} ; σ_y is the yield stress of the tendons' material; Δ_0 is calculated from Eq. 6.14.

$$\sigma_{PT} = \text{minimum of } \begin{cases} \sigma_{PT-S} \\ \sigma_{PT-CP} \end{cases} \quad (\text{Equation 6.16})$$

$$\sigma_{PT-S} = 0.9\sigma_y / \left[1 + \frac{1.2 \times 10^4 D^{0.78}}{PT^{1.4} H^2} \times (\Delta_{S-P} - \Delta_0) \right] \quad (\text{Equation 6.17})$$

$$\sigma_{PT-CP} = \sigma_y / \left[1 + \frac{1.2 \times 10^4 D^{0.78}}{PT^{1.4} H^2} \times (\Delta_{CP-P} - \Delta_0) \right] \quad (\text{Equation 6.18})$$

11) The cross sectional area of the tendon (A_{PT}) is calculated using Eq. 6.19, where;

$$A_{PT} = \frac{\pi D^2 \times PT \times f'_c}{4 \sigma_{PT}} \quad (\text{Equation 6.19})$$

12) If required, F_{CP-y} , F_{S-y} , Δ_{CP-y} , and Δ_{S-y} are computed using Eqs. 3, 4, 5, and 6, respectively.

6.14 Findings and Conclusions

This manuscript presents a design procedure for segmental precast post-tensioned concrete filled fiber reinforced polymer tubes (CFFT). The piers consisted of a single precast segment sandwiched between the foundation and the superstructure with an unbonded post-tensioning tendon passing through ducts located in the centroid of the segment. A series of 84 piers having different design parameters were analyzed using a finite element model. Criteria for two performance levels for the SPPT pier system were proposed. A set of empirical equations, capable of predicting the bilinearized backbone curve of the piers, had been developed using the results of the FE models of 84 piers. Those empirical equations had been arranged to form a design procedure for the SPPT pier system to fulfill the two performance levels. The analyses conducted in this manuscript revealed that:

- The developed empirical equations were able to predict the bilinearized backbone curve of the SPPT piers with good accuracy.
- The yield and performance lateral loads were found to be inversely proportional to the pier's height and directly proportional to the piers diameters, stress induced on the concrete from the post-tensioning load and the external bridge gravity load.
- Within the scope of the investigated parameters, the performance of the piers was governed by the preset lateral drift angles of 4.5% and 2.0% for collapse-prevention and serviceability performance levels with no yielding in the tendons or crushing in the concrete.

- The developed empirical equations to predict the lateral displacement vs. change in post-tensioning stresses were able to capture the behavior of the tendons. The rate of increase in post-tensioning stress was found to be directly proportional to the diameter of the pier and inversely proportional to the pier's height and the post-tensioning stress on the concrete. On the other hand, the displacement at which the increase in post-tensioning stress start was inversely proportional to the pier's diameter and directly proportional to the pier's height, post-tensioning and serviceability axial load stress acting on the pier.

The presented set of design equations represents the first design procedure for SPPT piers having concrete filled fiber tubes segments that can be elaborated in the future. The design methodology was developed based on the data collected from 84 piers with different design parameters including the dimensions and the load combinations that acts on the pier. However, other parameters such as different distribution of post-tensioning tendons, f_c of the concrete and confinement properties should be taken into consideration in future studies. Also, while the FE model was validated against three sets of experimental data (Dawood et al. 2010(a), ElGawady and Dawood 2010, and Dawood 2010), the FE model and equations were not validated against dynamic tests. However, no such data is available in the literature yet.

6.15 References

- ABAQUS Software and Documentation, Version 6.8-2. © Dassault Systèmes, SIMULIA, 2008.
- Beque, J., Patnaik, A. K., and Rizkalla, S., (2003), "Analytical models for concrete confined with FRP tubes" J. Composites for Construction, ASCE, 7(1), 31-38.

- California Office of Emergency Services (OES), vision 2000: Performance Based Seismic Engineering of Buildings, Structural Engineers Association of California, Sacramento, USA, 1995
- Chang, K. C., Loh, C. H., Chiu, H. S., Hwang, J. S., Cheng, C. B., and Wang, J. C. (2002). “Seismic behavior of precast segmental bridge columns and design methodology for applications in Taiwan”, Taiwan Area National Expressway Engineering Bureau, Taipei, Taiwan in Chinese.
- Chou, C.-C., and Chen, Y.-C., (2006). “Cyclic tests of post-tensioned precast CFT segmental bridge columns with unbonded strands” J. Earthquake Engng. Struct. Dyn., 35, 159-175.
- Dawood, H. M., “Seismic Behavior and Design of Segmental Precast Post-tensioned Concrete Piers”, M.S. thesis, Washington State University, Washington, 2010
- Dawood, H., ElGawady, M., and Hewes, J., (2010(a)-in review). “Behavior of segmental precast post-tensioned concrete bridge piers under lateral loads: experimental and modeling”, ASCE, Journal of Bridge Engineering.
- Dawood, H., ElGawady, M., and Hewes, J., (2010(b)-in review). “Behavior of segmental precast post-tensioned concrete bridge piers under lateral loads: parametric study”, ASCE, Journal of Bridge Engineering.
- ElGawady, M., Booker, A., Dawood, H. M. (2010). “Seismic behavior of post-tensioned concrete filled fiber tubes”, ASCE, Journal of Composites for Construction, (to appear in October 2010 issue)
- ElGawady, M., and Dawood, H., (2010-In review). “Finite element analysis of self-centering segmental piers” 10th International Symposium on Fiber Reinforced Polymer Reinforcement for Concrete Structures, Tampa, FL, USA (April 2-4, 2011).

- ElGawady, M. A., Shaalan A., and Dawood, H. M. (2010). “Seismic behavior of precast post-tensioned segmented frames”, 9th U.S. National and 10th Canadian Conference on Earthquake Engineering (July 25-29, 2010).
- ElGawady, M., and Shaalan, A., (2010- in review). “Seismic behavior of self-centering bridge bents”, ASCE, Journal of Bridge Engineering.
- Fam, A. Z., and Rizkalla, S. H., (2001), “Confinement model for axially loaded concrete confined by circular fiber-reinforced polymer tubes” ACI Str. J., 98 (4), 451-461.
- FEMA 356 (2000). "Prestandard and Commentary for the Seismic Rehabilitation of Buildings". Federal Emergency Management Agency. Washington, District of Columbia.
- Hewes, J. T., and Priestley N. (2002). “Seismic design and performance of precast concrete segmental bridge columns.” Report No. SSRP-2001/25, Univ. of California at San Diego.
- Kurama, Y. C. (1997). “Seismic analysis, behavior, and design of unbonded post-tensioned precast concrete walls.” PhD dissertation, Dept. of Civil and Environmental Engineering, Lehigh University, Bethlehem, Pa.
- Kwan, W.-P., and Billington, S. L. (2003). “Unbonded posttensioned concrete bridge piers. I: Monotonic and cyclic analyses.” J. Bridge Eng., 8(2), 92–101.
- Lee, WK and Billington, SL (2010) “Residual Displacement Prediction for Structural Concrete Columns under Earthquake Loading,” ASCE J. Bridge Engineering, 15(3): 240-249.
- Lee, J., and G. L. Fenves, (1998) “Plastic-Damage Model for Cyclic Loading of Concrete Structures,” Journal of Engineering Mechanics, vol. 124, no.8, pp. 892–900.
- Lubliner, J., J. Oliver, S. Oller, and E. Oñate, (1989) “A Plastic-Damage Model for Concrete,” International Journal of Solids and Structures, vol. 25, pp. 299–329.

- Mander, J. B., Priestley, M. J. N., and Park, R. (1988). “Theoretical stress-strain model for confined concrete.” *J. Struct. Eng.*, 114(8), 1804–1826.
- Marriott., D., PaMPanin, S., and Palermo, A., (2009). “Quasi-static and pseudo-dynamic testing of unbonded post-tensioned rocking bridge piers with external replaceable dissipaters” *J. Earthquake Engng. Struct. Dyn.*, 38, 331-345.
- Priestley, M.J.N., Calvi, G. M., and Kowalsky, M. J., “Displacement Based Seismic Design of Structures,” IUSS Press, Pavia, Italy, 2007, 720pp.
- Samaan, M., Mirmiran, A., and Shahawy, M. (1998). “Model of concrete confined by fiber composite.” *J. Struct. Eng.*, 124(9), 1025–1031.
- Teng, J. G., Jiang, T., Lam, L., and Luo, Y.Z., (2009), “Refinement of a design-oriented stress strain model for FRP-Confined concrete” *J. Composites for Construction*, ASCE, 13(4), 269-278.
- Wight, G. D., Kowalsky, M. J., and Ingham, J. M., (2007). “Direct Displacement-Based Seismic Design of Unbonded Post-Tensioned Masonry Walls.” *ACI Structural Journal*, V. 104, No. 5, pp. 560-569.
- Yamashita, R., and Sanders, D. H. (2009). “Seismic Performance of Precast Unbonded Prestressed Concrete Columns.” *ACI Structural Journal*, V. 106, No. 6, pp. 821-830.

APPENDIX

APPENDIX A

MATERIALS TESTING

During the current research different properties of the used materials were tested and will be explained through this part of the appendix.

A.1 Concrete

Several concrete cylinders were cast during pouring the specimens by ElGawady et al. (2020) and ElGawady and Shaalan (2010) (ASTM C172) and cured until the testing day (ASTM C192). Compressive strength (ASTM C39/C39M) was measured for six cylinders, three for concrete which was expected to give $f'_c = 13.8$ Mpa [2000 psi] and three more for $f'_c = 20.7$ Mpa [3000 psi] (Table A.1), (Fig. A.1). To assure the full contact between the cylinder ends and the machine's loading heads, either a steel cap filled with rubber or gypsum caps were used.



Figure A.1 Test setup for computing concrete characteristic strength f'_c

Table A.1 Summary of compression test results

Expected strength	Failure load kN [lbs]	f _c Mpa [psi]	status	f _c average
13.8Mpa [2 ksi]	509 [114,453]	27.9 [4050]	rejected	14.3 Mpa [2068psi]
13.8Mpa [2 Ksi]	246 [55,218]	13.5 [1954]	ok	
13.8Mpa [2 Ksi]	274 [61,672]	15.0 [2182]	ok	
20.7Mpa [3 ksi]	387 [86,953]	21.2 [3077]	ok	20.5 Mpa [2973psi]
20.7Mpa [3 Ksi]	380 [85,395]	20.8 [3022]	ok	
20.7Mpa [3 Ksi]	355 [79,706]	19.4 [2820]	ok	

Five more concrete cylinders were tested to calculate the static modulus of elasticity (ASTM C469) of the concrete (Figs. A.2 & A.3). Because the actual modulus of elasticity was computed, this value replaced the theoretical one suggested by Samaan et al. (1998) in their model as this should be used when no testing results are available.



Figure A.2 Test setup for computing static modulus of elasticity of the concrete cylinders

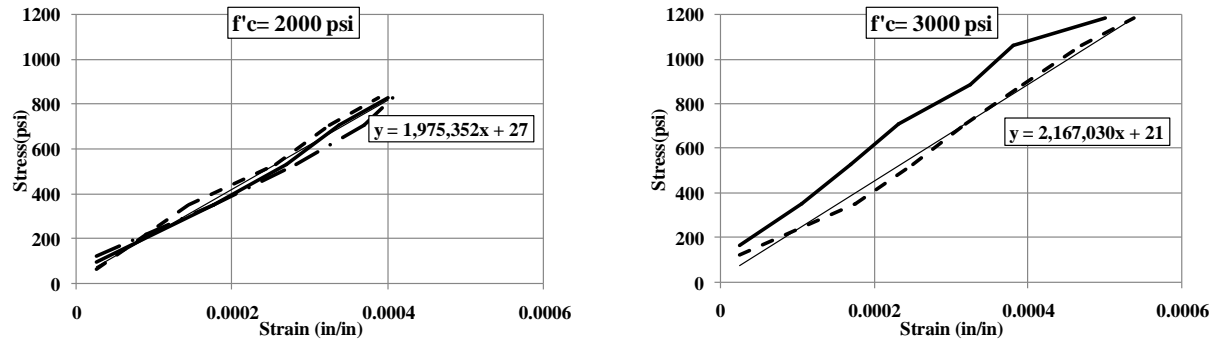


Figure A.3 Stress strain curves from the cylinders tests along with the equations of the trend lines

For information about testing results of the concrete cylinders of the concrete used in the piers studied in chapters (3) and (4) refer to Hewes (2002).

A.2 Post-tensioning bars

The stress-strain curve used in chapter (5) of this manuscript is supplied by a certified test report provided by the DYWIDAG Company which was done by North Star Steel Minnesota on 02/11/2003 (Fig. A.4). The post-tensioning bars in chapters (3 and 4) were used as reported by Hewes (2002).



NORTH STAR STEEL MINNESOTA

P.O. Box 64189
1678 Red Rock Road
Saint Paul, Minnesota 55164

Heat #: S57731
Size: 32mm Int.
Product: Dywidag
Grade: D150
Date Rolled: 2/10/03
P.O.
M.O. #: C0019997

CERTIFIED TEST REPORT

CHEMICAL ANALYSIS (WT %)

C	Mn	P	S	Si	Sn	Cu	Ni	Cr	Mo	Cb	V	Co	Al	Ti	Ca	N
0.50	1.38	0.015	0.024	0.62	0.016	0.26	0.44	0.21	0.02	0.003	0.088	0.0100	0.003	0.0042	13	132

MATERIAL 100% MELTED AND ROLLED IN THE USA. MANUFACTURING PROCESSES FOR THIS STEEL, WHICH MAY INCLUDE SCRAP MELTED IN AN ELECTRIC ARC FURNACE AND HOT ROLLING, HAVE BEEN PERFORMED AT NORTH STAR STEEL MINNESOTA, 1678 RED ROCK ROAD, SAINT PAUL, MINNESOTA, USA. ALL PRODUCT PRODUCED FROM STRAND CAST BILLETS. NO WELD REPAIRMENT PERFORMED. STEEL NOT EXPOSED TO MERCURY OR ANY LIQUID ALLOY WHICH IS LIQUID AT AMBIENT TEMPERATURES DURING PROCESSING OR WHILE IN NORTH STAR STEEL MINNESOTA POSSESSION.

JOMINY END QUENCH HARDENABILITY RESULTS (HRC)

J1	J2	J3	J4	J5	J6	J7	J8	J9	J10	J11	J12
J13	J14	J15	J16	J18	J20	J22	J24	J26	J28	J30	J32

MECHANICAL TEST REPORT

SPECIMEN AREA (in ²)	YIELD (Kpsi)	YIELD (Ksi)	TENSILE (Kpsi)	TENSILE (Ksi)	GAUGE LENGTH (in)	% ELONG	BEND	% R.A.	SPECIFICATION / GRADE
1.261	159.8	126.8	202.9	160.9	12.50	10.40	OK		D150
1.256	168.0	133.8	204.4	162.7	12.50	9.60	OK		D150

Additional Specifications/Comments:

Meets Material requirements of A722-95

A722-95

Conforms to DSI, USA, INC. Spec 2, Revision 5, Issued Aug 14th 1997.

Grain Size: <input type="text"/>	Reduction Ratio: <input type="text"/>	C.E. Per: <input type="text"/>	As Rolled surface Hardness Bhn HRC Test 1: <input type="text"/> Test 2: <input type="text"/>
Coding: CIN	DJ: 5.37 in. Ms: <input type="text"/> Deg F.	C.E: <input type="text"/>	

CHARPY IMPACT TEST

* Test 1	Test 2
Temp (F)	
ft-lb 1	
ft-lb 2	
ft-lb 3	

Micro Clean Average
At: Ab: Bt: Bh: Ct: Ch: Dt: Dh: S-Rating: O-Rating:
Macro Etch:

ASTM Test Method

Accredited to:	ASTM A370	ASTM E9	ASTM E10	ASTM E19	ASTM E23	ASTM E112	ASTM E255	ASTM E298	ASTM E415	ASTM E1619
ISO Guide 25	X	X	X	X				X	X	X
ISO Guide 25 AND FQA									X	X
Subcontractor (ISO Guide 25)		*			*	*	*			

The above results relate only to the items tested.

* Denotes tests performed by subcontractors in accordance with ASTM standards.

Chemical tests performed in accordance with ASTM E415 and E1019.
Mechanical tests performed in accordance with ASTM E8, E10 and A370. All other tests performed in accordance with the requirements of applicable specifications unless otherwise noted above. We hereby certify that the above test results are representative of those contained in the records of the company.

Any modification to this certificate as provided by North Star Steel Minnesota without the expressed written consent of North Star Steel Minnesota negates the validity of this test report. This report shall not be reproduced except in full, without the expressed written consent of North Star Steel Minnesota. North Star Steel Minnesota is not responsible for the inability of this material to meet specific applications.

SIGNED:

DATE: 02/11/2003

APPROVAL:

SWORN AND SUBSCRIBED TO BEFORE ME

THIS _____ DAY _____
(NOTARY PUBLIC)
THIS CERTIFICATE IS NOTARIZED ONLY WHEN REQUESTED.

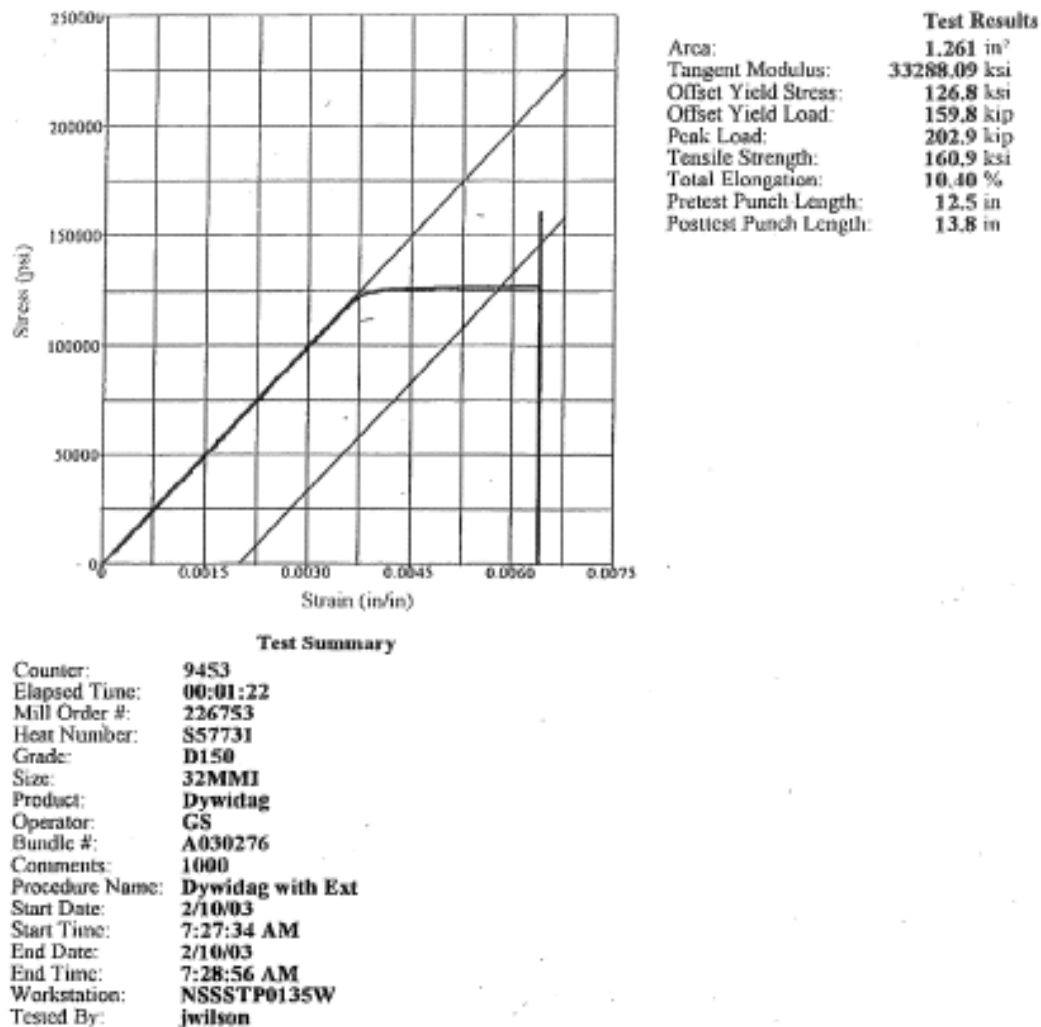


Figure A.4: Copy of the report supplied by the DYWIYDAG company

A.3 Glass Fiber Reinforced Polymer (GFRP)

GFRP was tested in tension by (Rai) (Table A.2) and compression by (Westmoreland Mechanical Testing & Research, Inc.) using (ASTM D6641) (Fig. A.5).

Table A.2 Summary of tension tests of GFRP specimens (Rai)

Gauge length: 2 in Strain rate: 0.1 in/in.min Date of test: 09/29/09						
Sample	Thickness mm [in]	Width mm [in]	Peak stress Mpa [psi]	Cracking stress Mpa [psi]	Cracking strain (%)	Young's modulus Mps [psi]
1	3.23 [0.127]	12.98 [0.511]	65.0 [9427]	55.9 [8108]	0.3946	13627 [1,976,442]
2	3.20 [0.126]	13.00 [0.512]	64.0 [9283]	60.0 [8707]	0.4126	14436 [2,093,749]
3	3.23 [0.127]	12.98 [0.511]	63.5 [9203]	56.9 [8248]	0.3979	14543 [2,109,212]
4	[discarded]	[--]	[--]	[--]	--	[--]
5	3.20 [0.126]	12.93 [0.509]	62.4 [9046]	51.0 [7392]	0.3721	12303 [1,784,448]
6	3.23 [0.127]	13.13 [0.517]	63.7 [9248]	57.0 [8272]	0.3970	14332 [2,078,645]
			Mean (Young's modulus) =			13848 [2,008,499]



Westmoreland Mechanical Testing & Research, Inc.

P.O. Box 388

221 Westmoreland Drive

Youngstown, Pa. 15696-0388 U.S.A.

Telephone: 724-537-3131 Fax: 724-537-3151

Website: www.wmtr.com

WMT&R is a technical leader in the material testing industry.

1 December 2009

Washington State University
100 Dairy Road
Pullman, WA 99164-1120

WMT&R Report No.: 9-41303
Purchase Order No.: K621273
WMT&R Quote No.: QN292761

Attention: Dr. Mohammed ElGawady

Subject: Compression Testing of Glass Fiber Reinforced Polymer Tube Sections

Introduction

Five (5) already machined tube sections, identified as glass fiber reinforced polymer material, were provided by Washington State University for compressive strength testing. An additional specimen was provided as a spare in the event of an invalid result. Testing was originally to be performed in accordance with ASTM D3410 but due to the unavailability of an ASTM D3410 fixture, WMT&R was given authorization by Washington State to substitute ASTM D6641 as the test standard of interest. As a result, the overall specimen length was reduced from 6.0" to 5.5" to comply with Section 4.1 of ASTM D6641.

Prior to testing, the cross section area of each specimen was measured using a Keyence VHX 600E Digital Microscope with integrated image analysis software. Each cross section image was calibrated at 10X magnification, a perimeter sketched around the specimen, and the area within determined (Figure 1). The width and thickness of each specimen was also measured at three (3) distinct locations within the middle 0.5" such that an alternate cross section area may be determined using a nominal tube outer diameter and average width/thickness values. All specimens were then equipped with a Vishay Micromeritics uniaxial general purpose strain gage, Item No. CEA-06-125UN-350, on the outer diameter face for strain measurement. A bending evaluation as defined by Section 7.6 of ASTM D6641 was not performed due to monetary concerns.

Testing was conducted utilizing a fixture capable of inducing a compressive force through simultaneous end and shear loading as shown in Figure 2. The test fixture bolts used to control shear loading were torqued to a minimum of 25in.*lbs applied in increments using a diagonally crossing pattern. Following specimen installation, the fixture was placed between two well aligned platens then a compressive load applied at a crosshead controlled rate of 0.05in./min. until rupture.

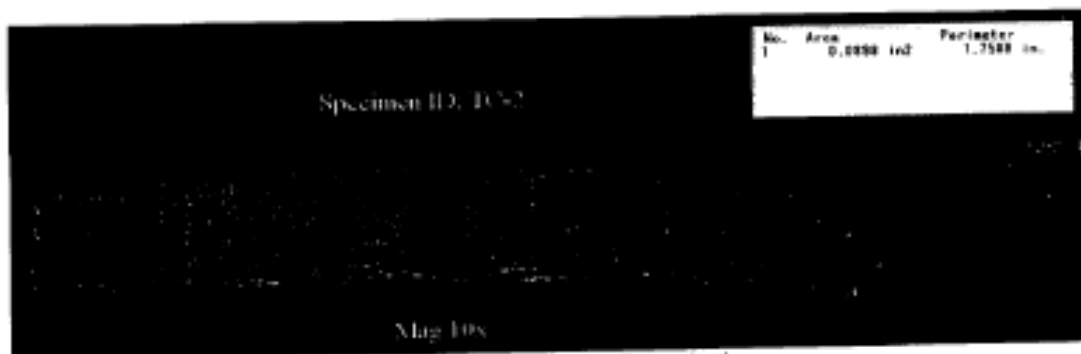


Figure 1: Cross Section Area Determination

"NOTE: THE RECORDING OF FALSE, FICTITIOUS, OR FRAUDULENT STATEMENTS OR ENTRIES ON THIS DOCUMENT MAY BE PUNISHABLE AS A FELONY UNDER FEDERAL STATUTE."

THIS CERTIFICATE OR REPORT SHALL NOT BE REPRODUCED EXCEPT IN FULL, WITHOUT THE WRITTEN APPROVAL OF WMT&R, INC.

Testing Specialists for Aerospace, Automotive, and Material Testing Fields

Locations in Youngstown, PA U.S.A. ~ Tel. (724) 537-3131 and

Banbury, Oxon U.K. ~ Tel. +44 (0) 1295 261211

1 December 2009
Purchase Order No.: K621273

WMT&R Report No.: 9-41303

Continued:



Figure 2: ASTM D6641 Test Fixture

An automated test system utilizing an Instron servo-controlled, hydraulically actuated test frame in conjunction with software designed by Westmoreland Mechanical Testing and Research, Inc., provided the means for load application. Vishay-MicroMeasurements Strain Smart Software Version 3.10 with a model 5100 scanner provided the means for acquisition of load and strain at a sampling rate of 50 points per second.

Testing results, including relevant comments, may be found on the following pages and accompanying compact disc. The graphical data was plotted to the maximum strain value acquired. Strain to rupture was not obtained for Specimen ID Nos. TC-3 and TC-5 as a result of deformation of the test area which detached the gage and consequently terminated the signal. All tested and untested material is also enclosed.

All machining, testing and inspections were performed in accordance with the WMT&R Quality Assurance Manual Rev. 11, dated 12/3/2008.

If you have any questions concerning this report, please feel free to contact me. If I am unavailable, you may also speak with Mr. Matt Wojton, Tensile Laboratory Supervisor.

At your service,

Ethan Pytash
Mechanical Engineer

bt

K:\Epytash\Washington State University\9-41303\9-41303.doc

NOTE: THE RECORDING OF FALSE, FICTITIOUS, OR FRAUDULENT STATEMENTS OR ENTRIES ON THIS DOCUMENT MAY BE PUNISHABLE AS A FELONY UNDER FEDERAL STATUTE.
THIS CERTIFICATE OR REPORT SHALL NOT BE REPRODUCED EXCEPT IN FULL, WITHOUT THE WRITTEN APPROVAL OF WMT&R, INC.



Materials Testing Laboratory
Tuesday, December 01, 2009

Washington State University
100 Dairy Road
Pullman, WA 99164-1120
Attention: Dr. Mohammed ElGawad

Westmoreland Mechanical Testing and Research, Inc.

ASTM D6641 Testing Results



WMT&R Report Number: 9-41303
WMT&R Quote Number: QN292761
Washington State Purchase Order Number: K621273

Test Type: Compressive Properties per ASTM D6641-09
Test Environment: 72°F / Ambient Air
Speed of Testing: 0.050 in./min.
Material: Glass Fiber Reinforced Polymer Tube Sections

Specimen ID	Test Log Number	Ult. Comp. Strength (ksi)	Ult. Comp. Load (lbf)	0.2% Off. Yield Strength (ksi)	0.2% Off. Yield Load (ksi)	Modulus (Msi)	Width (in.)	Thickness (in.)	Machine Number	Disposition
TC-1	L28887	-27.122	-2465.4	-23.032	-2093.6	2.46	0.7599	0.1267	H14	R
TC-2	L28888	-28.162	-2528.9	-24.565	-2205.9	2.46	0.7630	0.1252	H14	R
TC-3	L28889	-29.097	-2572.2	-24.806	-2192.9	2.55	0.7615	0.1248	H14	R
TC-4	L28890	-28.044	-2465.1	-23.323	-2050.1	2.45	0.7604	0.1209	H14	R
TC-5	L28891	-26.950	-2476.7	-21.120	-1940.9	2.11	0.7607	0.1205	H14	R
Average		-27.875	-2501.7	-23.369	-2096.7	2.41	0.7611	0.1236		
Standard Deviation		0.8697	47.4140	1.4722	109.1259	0.1696	0.0012	0.0027		
Coefficient of Variation		-3.1200	-1.8953	-6.2999	-5.2047	7.0412	0.1592	2.2112		

AU/R: A=Acceptable, U=Unacceptable, R=Report

Notes:

- All specimens were equipped with a Vishay MicroMeasurements uniaxial general purpose strain gage, Item No. CEA-06-125UN-350, on the outer diameter side.
- A 25in*lb torque was applied to all fixture bolts in increments using a diagonally crossing pattern.
- Load-Strain Data was recorded at 50 data points per second using Vishay-MicroMeasurements Strain Smart Software Version 3.10 in conjunction with a model 5100 scanner.
- All modulus calculations were performed using a range of 1000 to 3000 microstrain according to ASTM D6641.

Ethan P. Pysak
Ethan Pysak
Mechanical Engineer

Figure A.5: Copy of the compression testing report of the FRP

A.4 Fiber Sheets Used To Retrofit JH12 & JH22 (CHAPTER 3)

Table A.3 shows the FRP material's properties used to retrofit piers JH12 and JH22 (chapter 3).

Table A.3 Typical dry fiber properties used in chapter (3)

Tensile strength	3.24 GPa [470,000 psi]
Tensile modulus	72.4 GPa [10.5×10^6 psi]
Ultimate elongation	4.5%
Density	2.55 g/cm ³ [0.092 lbs/in ³]
Weight per sq. yd.	915 g/m ² [27 oz.]
Fiber thickness	0.36 mm [0.014 in]

A.5 References:

- ASTM C172 (Standard practice for sampling freshly mixed concrete).
- ASTM C 39/C 39M (Standard test method for compressive strength of cylindrical concrete specimens).
- ASTM C469 (Standard test method for static modulus of elasticity and poisson's ratio of concrete in compression).
- ASTM C192 (Making and curing concrete test specimens in the laboratory).
- ASTM C617 (Capping cylindrical concrete specimens).
- ASTM C469 (Static modulus of elasticity and poisson's ratio of concrete in compression).
- ElGawady, M., Booker, A., Dawood, H. M. (2010- In press). "Seismic behavior of post-tensioned concrete filled fiber tubes", ASCE, Journal of Composites for Construction.
- ElGawady, M., and Shaalan, A., (2010- In review). "Seismic behavior of self-centering bridge bents", ASCE, Journal of Bridge Engineering.
- Hewes, J.T. "Seismic Design and Performance of Precast Concrete Segmental Bridge Columns." Ph.D. Dissertation, University of California, San Diego, La Jolla, California. 2002.